

# **Halogens in Ocean Island Basalts**

**A report submitted in partial fulfilment of the  
requirements for the degree of MEarthSci Hons.  
(Geology) at the University of Manchester**

**May 2010**

**58693681**

**Lisa Abbott**

**The University of Manchester**

**School of Earth, Atmospheric and Environmental Sciences**

**Oxford Road**

**Manchester**

**M13 9PL**



View of Tristan da Cunha, taken from HMS Endurance's helicopter, 12<sup>th</sup> April 2007 (Image taken from The Tristan da Cunha Website 2009).

## Abstract

The halogen composition of thirteen basalts from ocean island settings, including nine samples from Tristan da Cunha, have been analysed using an extension of the Ar-Ar technique. The ocean island basalts (OIBs) have a subducted halogen signature, showing a strong overlap with I/Cl and Br/Cl in marine pore fluids. The OIBs show a mixing between mid-ocean ridge basalt (MORB) / bulk Earth (BE) and sediment, or marine pore fluid end-members. I/Cl values for the OIBs extend up to  $4.1 \times 10^{-3}$ ; Br/Cl values range up to  $3.4 \times 10^{-3}$ . The highest values are observed in the Inaccessible Island samples, suggesting that the mantle source has evolved over time. Petrological analysis suggests a similar composition for the Tristan and Inaccessible Island basalts; however, Tristan eruptions appear to have been more effusive and less gaseous, due to the absence of vesicles. Cl/K values observed show a mixing between MORB and OIB.

The low  $^3\text{He}/^4\text{He}$  values suggest that U-rich sediment is being recycled into the mantle source. The  $^{40}\text{Ar}/^{36}\text{Ar}$  values are air-like in composition, suggesting that dissolved air is being recycled within the sediment pore fluid.

Estimates of halogen abundances in the Tristan mantle source are 90 ppm Cl, 0.46 ppm Br and 0.25 ppm I, giving Br/Cl  $2.3 \times 10^{-3}$  and I/Cl  $776 \times 10^{-5}$ . A maximum of 400 ppm sediment in the Tristan mantle source is needed to obtain the halogen ratios observed.

*Keywords:* ocean island basalts; halogens; noble gases; Tristan; mantle hotspots

## Contents

Abstract.....	3
List of Figures .....	7
List of Tables.....	9
1 Introduction.....	10
1.1.1 Mantle Geochemistry .....	10
1.1.2 Halogens .....	11
1.2 Aims.....	11
1.3 Outline of Dissertation.....	12
2 Background and Previous Work .....	13
2.1 Halogens.....	13
2.1.1 Halogen Concentrations in OIB, MORB and Diamonds .....	15
2.2 Noble Gases .....	17
2.3 Mantle Hot Spots .....	18
2.4 Tristan da Cunha .....	19
2.4.1 Geological Setting .....	21
2.4.2 1962 Expedition.....	23
3 Experimental Methods.....	24
3.1 Sample Description.....	24
3.1.1 Optical Microscopy .....	24
3.2 Halogen and Noble Gas Analyses .....	26

3.2.1	Neutron Irradiation.....	26
3.2.2	Noble Gas Extraction .....	27
3.2.3	Noble Gas Isotopic Analysis.....	30
3.2.4	Air Calibration.....	32
3.2.5	Blanks .....	33
3.2.6	Data Reduction.....	33
3.2.7	Conversion of the Noble Gases to the Halogens, K and Ca.....	35
4	Results and Discussion .....	36
4.1	Petrography .....	36
4.1.1	BM 1962 128 / 60 (Tristan).....	36
4.1.2	BM 1962 128 / 112 (Tristan).....	38
4.1.3	BM 1962 128 / 114 (Tristan).....	39
4.1.4	BM 1962 128 / 116 (Tristan).....	40
4.1.5	BM 1962 128 / 341 (Tristan).....	41
4.1.6	BM 1962 128 / 446 (Inaccessible).....	42
4.1.7	BM 1962 128 / 473 (Inaccessible).....	43
4.1.8	BM 1962 128 / 480 (Inaccessible).....	45
4.1.9	BM 1962 128 / 482 (Tristan).....	46
4.1.10	BM 1962 128 / 484 (Tristan).....	47
4.2	The Halogens and K.....	48
4.2.1	Release Patterns.....	48

4.2.2	Cl, Br, I and K Relationships .....	52
4.2.3	Halogen and K Ratios .....	59
4.2.4	Halogen Ratios.....	63
4.3	Mantle Source Halogen Concentrations .....	68
4.4	Noble Gases .....	70
4.4.1	Argon.....	70
4.4.2	Helium .....	71
4.5	Réunion and Fogo .....	73
4.6	Implications for Mantle Halogen Geochemistry.....	74
4.7	Implications for the Source of the Tristan Mantle Plume.....	74
5	Conclusions.....	76
5.1	Ideas for Further Work .....	77
	Acknowledgements.....	79
	References.....	80
	Appendices .....	85

## List of Figures

Figure 2.1 Showing the ranges of MORB and pore fluid, with the values for chondritic (CI), bulk earth (BE) and model bulk earth (model BE).....	17
Figure 2.2 The location of Tristan da Cunha in the South Atlantic. ....	20
Figure 2.3 Locations of the Tristan da Cunha group islands.....	23
Figure 3.1 Tristan sample localities.....	24
Figure 4.1 Showing resorbed olivine (ol), zoned clinopyroxene (cpx) and multiply twinned leucite (leuc) under crossed-polars.....	36
Figure 4.2 Showing magma inclusions and twinning within clinopyroxene, and mineral preferred orientation within the groundmass. ....	38
Figure 4.3 Showing weak preferred orientation and porphyritic texture. ....	39
Figure 4.4 Showing preferred orientation.....	40
Figure 4.5 Showing resorbed clinopyroxene phenocryst and preferred orientation within the matrix. ....	41
Figure 4.6 Showing vesicular texture. ....	42
Figure 4.7 Showing vesicular texture and alternation of olivine rim to serpentine. ....	43
Figure 4.8 Showing vesicular texture and preferred orientation. ....	45
Figure 4.9 Showing twinned and resorbed clinopyroxene phenocryst. ....	46
Figure 4.10 Showing magma inclusions within an olivine phenocryst.....	47

Figure 4.11 Percentage release of Cr, Br, I and K during stepped heating of sample 473 (Inaccessible) .....	49
Figure 4.12 Showing the variation in Br/Cl and I/Cl with temperature.....	51
Figure 4.13 Showing the variation in K/Cl with temperature (in °C). .....	52
Figure 4.14 Br vs Cl for the Tristan and Inaccessible samples .....	54
Figure 4.15 I vs Cl for the Tristan and Inaccessible samples .....	56
Figure 4.16 K vs Cl for the Tristan and Inaccessible samples steps .....	58
Figure 4.17 Br/K vs Cl/K for the Tristan and Inaccessible samples.....	60
Figure 4.18 Showing the derivation of MORB and OIB Br/K estimates.....	61
Figure 4.19 I/K vs Cl/K for the Tristan and Inaccessible samples .....	62
Figure 4.20 I/Cl vs Br/Cl for the Tristan and Inaccessible samples .....	63
Figure 4.21 I/Cl vs Br/Cl showing MORB field and diamond data added. ....	65
Figure 4.22 I/Cl vs Br/Cl showing chondritic (CI), bulk Earth (BE) and model BE values.....	66
Figure 4.23 I/Cl vs Br/Cl showing marine pore fluid field and seawater .....	68
Figure 4.24 Showing the range of Ar values .....	71

## List of Tables

Table 2.1 Ar and He ratios of the Earth's reservoirs .....	18
Table 3.1 Sample location, locality and brief description. ....	25
Table 3.2 The reactions of the irradiated parent elements, producing the nucleogenic noble gas isotopes.....	29
Table 4.1 Tristan, Inaccessible, Fogo and Réunion halogen and K data. ....	53
Table 4.2 He and Ar data from previous study.....	72

# 1 Introduction

The Earth's mantle is both chemically and isotopically heterogeneous (Carlson 1995). The reason for this heterogeneity is disputed; possibilities include primordial variations in hidden or isolated mantle reservoirs or the presence of subducted oceanic crust and pelagic sediments (Davies 1990; Wilson 1993).

## 1.1.1 Mantle Geochemistry

Less chemical and isotopic variation is observed in mid-ocean ridge basalts (MORBs), which are more chemically uniform than ocean island basalts (OIBs) (Davies 1990). MORBs sample a mantle reservoir, which is relatively more depleted in incompatible elements due to the extraction of the Earth's crust (Carlson 1995). OIBs are relatively enriched in incompatible elements compared to MORB, as they are sourced from regions of the mantle which are thought to have remained relatively undepleted in incompatible elements (Davies 1990).

The variation in composition of OIBs is thought to be partially due to the recycling of ancient subducted crust and lithospheric mantle, together with sediments and marine pore fluids (Farnetani *et al.* 2002; Gibson *et al.* 2005; Sumino *et al.* 2010). OIBs are erupted at mantle hotspots, and are considered to be mantle plumes rising from the core-mantle boundary (Campbell 2007). As such, OIBs are extremely important as they sample the undepleted mantle reservoir and can therefore improve our understanding of mantle dynamics, particularly subduction, and provide information on the undepleted mantle source (Wilson 1993).

### **1.1.2 Halogens**

Chlorine (Cl), Bromine (Br) and Iodine (I) can be used as tracers of igneous and mantle processes as the Earth's reservoirs have distinct halogen signatures (Pyle & Mather 2009). As I is concentrated within pelagic sediments, it is an ideal geochemical tracer of sediment and marine pore fluid subduction; Cl is concentrated in seawater and Br is approximately equally split between the hydrosphere and the crust (Kendrick 2000; Sumino *et al.* 2010). Previous work has concentrated on the role of Cl and Br as chemical tracers, with relatively little work on I, perhaps due to the relatively low abundances of the halogens, with I being the least abundant of the heavy halogens (Aiuppa *et al.* 2008). By analysing the halogen signature present within OIBs, we may be able to identify the components present within OIB, and obtain information on the mantle source and gain evidence for deep recycling into the mantle.

For the purposes of this study only the heavy halogens, Cl, Br and I were analysed. F exhibits different geochemical behaviour, as it is a more compatible element able to substitute for OH<sup>-</sup> within hydrous minerals, due to its smaller ionic radius. As such, it partitions more readily into the solid phase and therefore gives us little information about the source of the magma, in contrast with Cl, Br and I.

## **1.2 Aims**

- To establish the halogen composition ratios (I/Cl and Br/Cl) and concentrations of plume source basalts (Tristan de Cunha), as a proxy for the undegassed mantle.

- To compare these ratios with MORB source mantle and subcontinental lithospheric mantle (SCLM).
- To derive/confirm the Bulk Earth (BE) halogen ratios and compare these with chondrite ratios and model values from condensation temperatures.
- To look for evidence of a recycled crustal halogen component.
- To establish the petrography, crystallisation history and texture of the basalts.

### **1.3 Outline of Dissertation**

Chapter 2 discusses the geochemical behaviour of the halogens and the previous work on mantle halogen geochemistry and their relationship to noble gases. It presents some of the current concentration and ratio data on both the halogens and Ar and He. The formation of OIBs and mantle hotspots is discussed briefly, and the geological setting of the Tristan da Cunha group of islands, which form the basis of the study, is presented.

Chapter 3 details the experimental methods and techniques used for the geochemical and petrographic analyses. The results of both these analyses are presented and discussed in Chapter 4. Chapter 5 highlights the conclusions of this study and provides suggestions for further work.

## 2 Background and Previous Work

### 2.1 Halogens

The halogens, fluorine (F), chlorine (Cl), bromine (Br), iodine (I) and astatine (At) belong to Group VII (Group 17 IUPAC) of the periodic table. They are non-metal elements and are highly volatile, with reactivity decreasing moving down the group. Due to their volatility, they are concentrated in the outer reservoirs of the Earth, mainly in the crust and hydrosphere (Kendrick 2000). Chlorine is concentrated in seawater (18,000 ppm), whereas the most significant reservoir of iodine is organic matter within sedimentary material (Déruelle *et al.* 1992; Kendrick 2000). Bromine is approximately equally split between the crust and the hydrosphere (Kendrick 2000).

Due to their large ionic radii, Cl, Br and I are incompatible elements in most anhydrous silicate minerals and as such, are concentrated in the liquid phase during partial melting (Pyle & Mather 2009). This liquid phase will be preserved as melt inclusions in host silicate phases or in basalt glass. F has a smaller ionic radius, the smallest of any anion, and accordingly exhibits different geochemical behaviour (Aiuppa *et al.* 2008). Unlike the heavy halogens, F is a compatible element which can substitute for OH<sup>-</sup> and oxygen within silicate minerals, as it has a similar ionic radius to oxygen (Aiuppa *et al.* 2008). Astatine forms as part of the <sup>238</sup>U and <sup>235</sup>U decay series; all of its isotopes have short half-lives, making it the least abundant naturally occurring element (Aiuppa *et al.* 2008; Pyle & Mather 2009). The enrichment of halogens in the surface reservoirs has arisen from degassing of the mantle during magmatic processes (Déruelle *et al.* 1992; Kendrick 2000).

The halogens are considered to be important tracers of mantle processes and fluid sources (Johnson *et al.* 2000; Pyle & Mather 2009). The heavy halogen (Cl, Br and I) concentrations and ratios (Br/Cl and I/Cl) within melt inclusions can be used to establish the source reservoir and components of the magma and to trace recycling of fluid and sediment components in subducted slabs in subduction zones (Pyle & Mather 2009). F and Cl can also be used to trace magma fractionation and evolution (Pyle & Mather 2009).

Significant fractionation of the heavy halogens is unlikely in the deeper regions of the Earth, however at shallower levels fractionation may occur in the presence of halogen-bearing mineral phases or during separation of immiscible fluids and melts (Johnson *et al.* 2000; Burgess *et al.* 2009). Cl-bearing minerals include apatite, amphibole and mica and other hydrous minerals, with apatite being the most probable at mantle depths (Johnson *et al.* 2000). Fluid-melt immiscibility, and melt-hydrous fluid partitioning are also thought to lead to fractionation of Cl, Br and I (Burgess *et al.* 2009). Cl will partition into the melt under reducing pressures caused by magma ascent, but under lower temperatures experienced during magma cooling Cl partitions in favour of the fluid phase (Aiuppa *et al.* 2008). Major halogen fractionation can also occur during freezing or evaporation of hydrous fluids (brines) although this is unlikely to be an important process in the Earth's mantle (Martin *et al.* 1993).

Further fractionation has been shown experimentally to occur at mantle temperature and pressure by the addition of Cl into carbonate-silicate melts (or by the addition of silicate into chloride-carbonate melts) (Safonov *et al.*

2007). This mixing leads to separation of the melt into an immiscible chloride-carbonate brine and carbonate-silicate melt (Safonov *et al.* 2007). Experimental studies have revealed that the melt/fluid and mineral/melt partition coefficients of the halogens are affected by the presence of other species, such as S, and by the overall composition of the melt (Aiuppa *et al.* 2008).

Addition and removal of the halogens may also occur via fluid-rock interaction, or interaction between the magma and meteoric or marine fluids, particularly with respect to Cl (Harris *et al.* 2000). Low  $\delta^{18}\text{O}$  values observed in some Tristan lavas suggest that the magmas were contaminated with volcanic edifice material that had interacted with hydrous fluids at high temperatures (Harris *et al.* 2000).

### **2.1.1 Halogen Concentrations in OIB, MORB and Diamonds**

Although there is increasing information on the halogen content of MORB, data on OIB are scarce, particularly with respect to I as none have so far been reported in the literature. Analysis by Schilling *et al.* (1978) estimated the Cl and Br concentrations of OIB to be 70-257 ppm and 0.27-0.69 ppm respectively, giving a Br/Cl ratio of  $1.2 \times 10^{-3}$  (mol/mol). Calculations by Jambon *et al.* (1995) are in good agreement with these values, giving a Br/Cl ratio of approximately  $1.1 \times 10^{-3}$ , although the estimated concentrations are lower at 35 ppm and 88 ppb for Cl and Br respectively.

Estimates for MORB halogens are better constrained. Cl concentrations range from 29-55 ppm; while estimates for Br range from 60-1,300 ppb (Déruelle *et al.* 1992; Jambon *et al.* 1995; Burgess *et al.* 2002). I in MORB

ranges between 8-10 ppb (Déruelle *et al.* 1992; Burgess *et al.* 2002). Analyses on African and Siberian diamonds, believed to sample the sub-continental lithospheric mantle, show Br/Cl values in the range  $(1.4-4.3) \times 10^{-3}$  (Figure 2.1), and I/Cl values extend from  $(9.4-70.0) \times 10^{-6}$  (with some ranging to  $176.4 \times 10^{-6}$ ) (Johnson *et al.* 2000; Burgess *et al.* 2002; Burgess *et al.* 2009). These values are consistent with MORB values (Figure 2.1) of  $(1.03-1.11) \times 10^{-3}$  Br/Cl and  $(15-25) \times 10^{-6}$  I/Cl (Burgess *et al.* 2009). Canadian diamonds however show a far greater range of values (Figure 2.1), with Br/Cl ranging from  $(1.3-63.0) \times 10^{-3}$  and I/Cl from  $(9.8-1703.5) \times 10^{-3}$  (Johnson *et al.* 2000; Burgess *et al.* 2009). It is considered that these higher ratios may result from crystallisation of Cl-rich phases, or the presence of Br- and I-enriched pore fluids within fluid inclusions, or melt-hydrous fluid partitioning and immiscible fluid separation (Johnson *et al.* 2000; Safonov *et al.* 2007; Burgess *et al.* 2009).

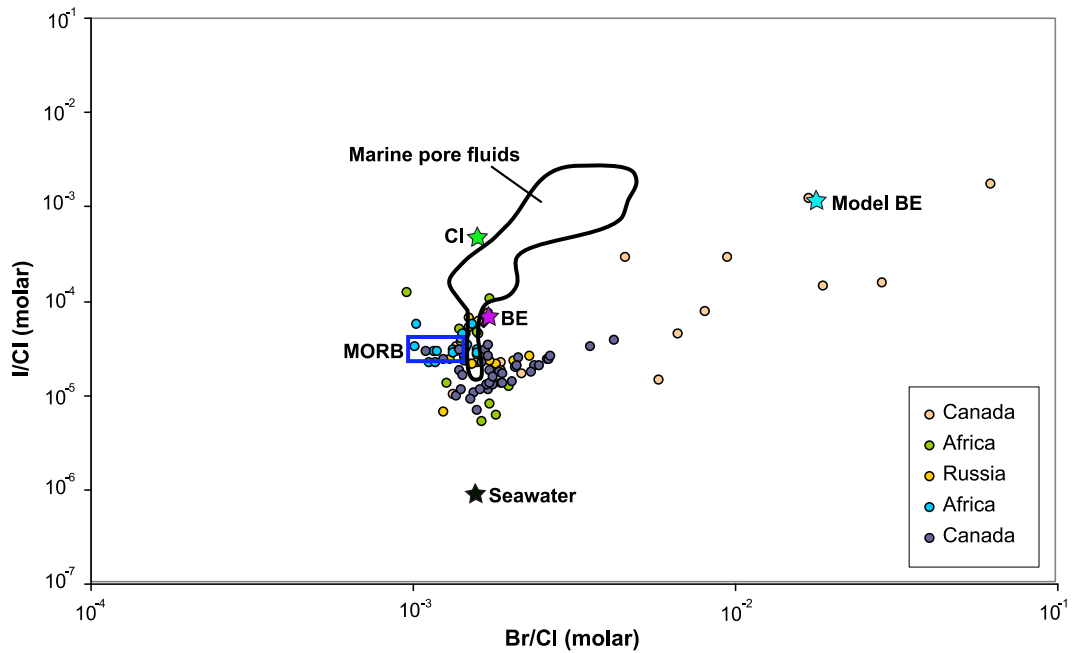


**Figure 2.1** Showing the ranges of MORB and pore fluid, with the values for chondritic (CI), bulk earth (BE) and model bulk earth (model BE). Diamond data are shown by the circles (Marine pore fluid data from (Martin *et al.* 1993; Mahn & Gieskes 2001; Sumino *et al.* 2010); MORB values from (Schilling *et al.* 1980; Jambon *et al.* 1995; Burgess *et al.* 2009); diamond, BE, CI and seawater data from (Johnson *et al.* 2000; Burgess *et al.* 2002; Burgess *et al.* 2009); model BE data derived from (Allègre *et al.* 2001)).

## 2.2 Noble Gases

Due to their high volatility, the noble gases are concentrated in the Earth's outer reservoirs (Kendrick 2000). Ar is the most abundant noble gas isotope on Earth (Kendrick 2000).  $^{40}\text{Ar}$  is formed by the decay of  $^{40}\text{K}$ ; essentially all  $^{40}\text{Ar}$  is from this decay, whereas  $^{36}\text{Ar}$  is primordial (Ballentine *et al.* 2002). As K is a highly incompatible element, this coupled with the degassing of the upper mantle has led to a high  $^{40}\text{Ar}/^{36}\text{Ar}$  ratio of  $> 40,000$  in the upper mantle reservoir (Table 2.1) (Graham 2002).

**Table 2.1 Ar and He ratios of the Earth's reservoirs (data from Kendrick 2000; Graham 2002; Pepin & Porcelli 2002).**

Reservoir	$^{40}\text{Ar}/^{36}\text{Ar}$	$^3\text{He}/^4\text{He}$
Atmosphere	295.5	$1.4 \times 10^{-6}$ (= $R_A$ )
Crust	> 295.5–37,500	0.01–0.001 $R_A$
Upper Mantle	> 40,000	8 $R_A$
Lower Mantle	3,000–12,000	< 38 $R_A$

$^4\text{He}$  is formed from during the decay of  $^{238}\text{U}$ ,  $^{235}\text{U}$  and  $^{232}\text{Th}$  (Porcelli *et al.* 2002). He is not gravitationally bound to the Earth, and the residence time of He in the Earth's atmosphere is approximately 1 Ma, thus He has a very low abundance in the atmosphere and  $^3\text{He}/^4\text{He}$   $R_A = 1.4 \times 10^{-6}$  (Pepin & Porcelli 2002). The  $^3\text{He}/^4\text{He}$  value for MORB is approximately 8  $R_A$ , indicating the presence of primordial  $^3\text{He}$  (Pepin & Porcelli 2002). OIB values are more varied, ranging from below MORB to a maximum of 38  $R_A$  (Pepin & Porcelli 2002). It is suggested that the higher  $R_A$  values of OIB may relate to either mantle which has remained undegassed during Earth's evolution, or it may represent He leaking from the core (Pepin & Porcelli 2002).

### 2.3 Mantle Hot Spots

Mantle hotspots form at intra-plate settings, due to the upwelling of anomalously hot and buoyant mantle material from the core-mantle thermal boundary (Campbell 2007; Wolfe *et al.* 2009). As such, they can provide us with geochemical insights into the undegassed mantle (Davies 1990). As hot

mantle material rises upwards in a mantle plume, it eventually punctures the overlying crust, resulting in the eruption of basalts (Gibson *et al.* 2005). Mantle plumes consist of a head up to 1,000 km wide, with a narrower tail beneath (Campbell 2007). The head of mantle plumes is thought to have been the cause of flood basalt eruptions in the geological past, with the mantle plume tail causing hotspot volcanicity as seen worldwide today (Richards *et al.* 1989; Gibson *et al.* 2005; Campbell 2007). Present day hotspots are often associated with large igneous provinces; the Tristan mantle plume, responsible for the creation of the Tristan da Cunha group of volcanic islands, is thought to have contributed to the Paraná-Etendeka continental flood basalt, which formed 138-127 Ma ago (Ernesto *et al.* 2002; Gibson *et al.* 2005).

## **2.4 Tristan da Cunha**

The Tristan da Cunha group comprises the three volcanic islands of Tristan da Cunha (known locally as Tristan), Nightingale and Inaccessible (McDougall & Ollier 1982; Le Roex *et al.* 1990). The islands are located in the South Atlantic, approximately 400 km east of the Mid-Atlantic Ridge (Figure 2.2) (McDougall & Ollier 1982; Le Roex *et al.* 1990).

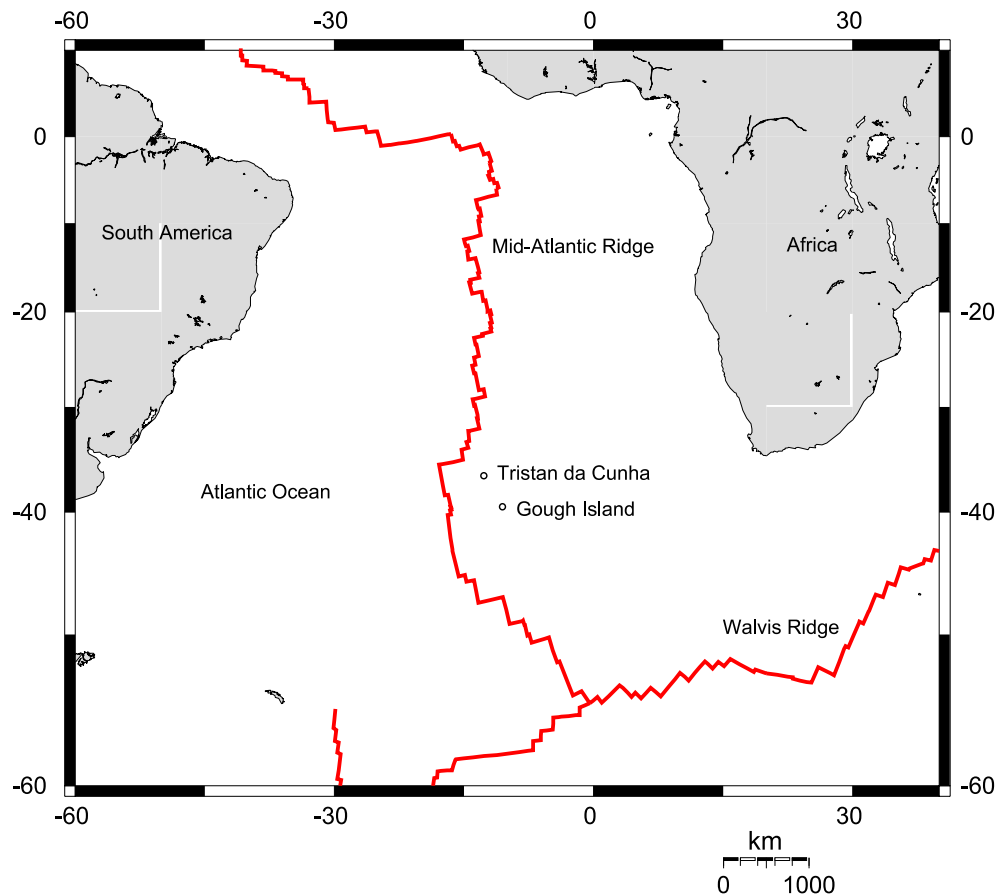


**Figure 2.2** The location of Tristan da Cunha in the South Atlantic (base map generated using GMT ([www.aquarius.geomar.de](http://www.aquarius.geomar.de))).

Six of the samples analysed herein were collected from Tristan and four are from Inaccessible Island. The Tristan volcano is over 5.5 km in height; the island itself rises to over 2.0 km above sea-level and is approximately 12 km in diameter (Baker *et al.* 1964; McDougall & Ollier 1982; Le Roex *et al.* 1990). The Tristan volcano is probably relatively young, with no lavas exceeding 1.0 Ma in age, and most being erupted between 0.2-0.1 Ma (Baker *et al.* 1964; McDougall & Ollier 1982; Le Roex *et al.* 1990). The most recent eruption on Tristan occurred on the 9<sup>th</sup> of October 1961, and continued until March 1962, and led to the evacuation of the entire island (Baker *et al.* 1964).

The rocks on Tristan are highly alkaline and range from ankaramitic basanite to phonolitic in composition (Le Roex *et al.* 1990). Geochemically, the rocks have an enriched radiogenic isotopic signature when compared with other oceanic islands, with a relatively high  $^{208}\text{Pb}$  and  $^{207}\text{Pb}$ , a signature known as the DUPAL anomaly whose origin is intensely debated, which is found in the southern Indian and Atlantic oceans (Harris *et al.* 2000; Gibson *et al.* 2005).

#### **2.4.1 Geological Setting**

The Tristan da Cunha group (Figure 2.3) is thought to have formed from the Tristan mantle plume tail (Gibson *et al.* 2005). The plume head is believed to have impacted Gondwanaland prior to 138 Ma, resulting in the formation of the Paraná-Etendeka continental flood basalt province (138-127 Ma), prior to the breakup of Gondwanaland and the opening of the South Atlantic Ocean (Gibson *et al.* 2005). The Tristan da Cunha islands, together with Gough Island, are thought to have formed due to volcanism related to the mantle plume tail in the last < 33 Ma; both Nightingale and Inaccessible are in an erosional phase, with Nightingale being the oldest of the three islands and Tristan the youngest; K-Ar dating indicates maximum ages of 18 Ma for Nightingale, 6 Ma for Inaccessible and < 1 Ma for Tristan (Gass 1967; Cliff *et al.* 1991; Gibson *et al.* 2005). The present day plume axis is thought to be beneath Gough Island, which lies to the south of Tristan (Gibson *et al.* 2005).

Tristan is the only active volcano in the group (Gass 1967). The main shield building phase of the volcano was short-lived occurring 0.2-0.1 Ma ago; in the past 15,000 years eruptions have only occurred from parasitic vents on the flanks of the main volcano, which total over thirty in number (Gass 1967;

McDougall & Ollier 1982; Le Roex *et al.* 1990). The island consists of interbedded layers of basaltic lava and associated pyroclastic material, ejected mainly from the central conduit (Baker *et al.* 1964). Within this sequence are buried parasitic centres formed by explosive activity (Baker *et al.* 1964). The pyroclastics appear to have formed by hydrovolcanic activity, either due to the magma interacting with a shallow water table, or a crater lake similar to the one in the central cone today (Chevallier & Verwoerd 1987). The majority of the secondary centres formed scoria cones, with strombolian eruptions ejecting pyroclastic material, or more rarely, lava flows (Baker *et al.* 1964; Chevallier & Verwoerd 1987). Only two secondary eruptive centres are effusive; Stony Hill, which was the most recently active centre (200-300 years ago) prior to the 1961 eruption, and the 1961 eruptive centre itself (Baker *et al.* 1964). These effusive centres are characterised by thick flows of lava, with little pyroclastic material (Baker *et al.* 1964).

The oldest rocks of the primary volcano are exposed at the Main Cliffs, with the rocks at the Peak representing the most recent activity associated with the central conduit (Baker *et al.* 1964). Four coastal strips have formed by eruption of lavas from secondary centres, the largest of these strips being the Settlement, where the 1961 eruption occurred (Baker *et al.* 1964).

Centred on the summit is a radial dyke swarm comprising over 90% of the dykes with the remainder being normal to this pattern (Baker *et al.* 1964). Very little erosion has taken place, with the main areas of denudation being the sea cliffs and the upper slopes of the Peak (Baker *et al.* 1964). There is no major folding or faulting on the island, with only small scale slumps observed within some of the tuffaceous layers (Baker *et al.* 1964).

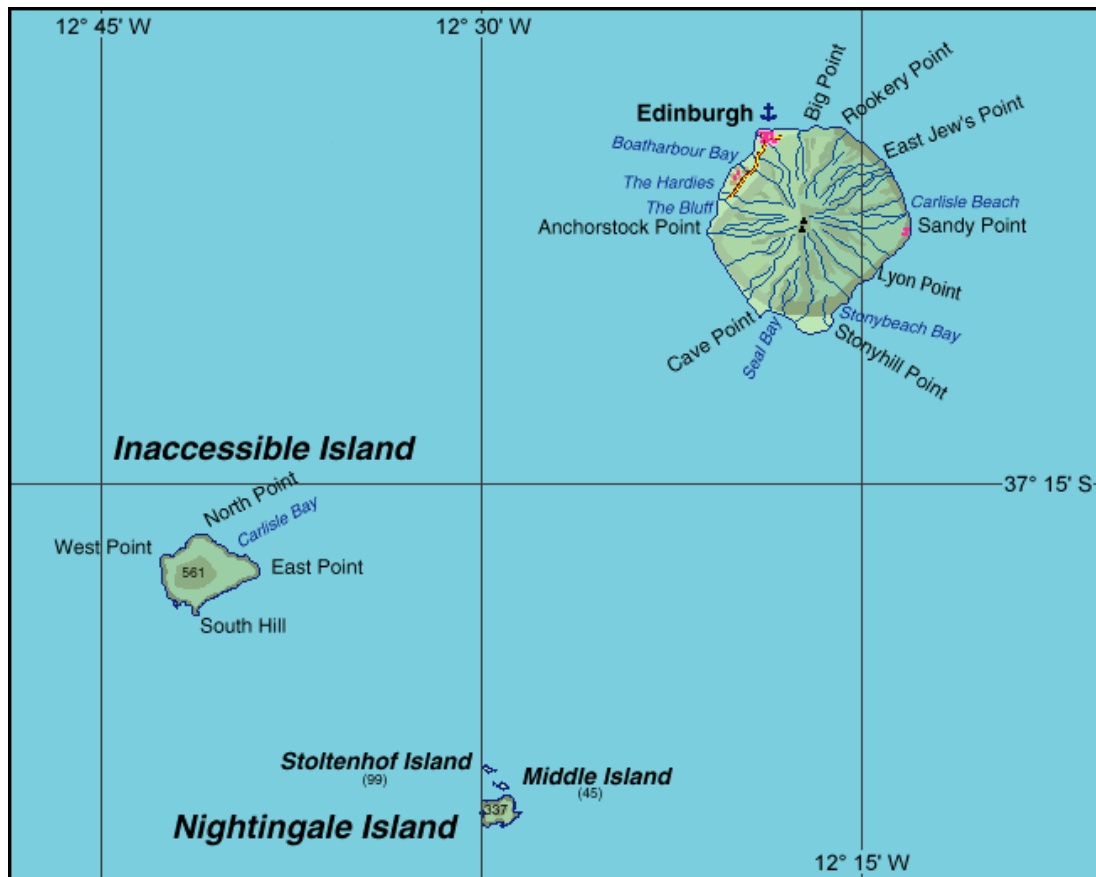


Figure 2.3 Locations of the Tristan da Cunha group islands (Tristan shown top right) (The Tristan da Cunha Website 2009).

#### 2.4.2 1962 Expedition

The six Tristan and three Inaccessible samples analysed are part of a collection (of 686 samples) housed at the Natural History Museum, London (B.M. 1962, 128) and were collected during the Royal Society Expedition to Tristan da Cunha in early 1962 (Baker *et al.* 1964). The aim of the expedition was to study the new parasitic volcano and its effect on the vegetation and fauna (Baker *et al.* 1964). The expedition consisted of twelve members, who spent six weeks surveying Tristan and one week on Inaccessible and Nightingale Islands (Baker *et al.* 1964). A geological survey of Tristan was undertaken and a geological map of the island produced, detailing the lithology and volcanic centres (Baker *et al.* 1964).

### 3 Experimental Methods

#### 3.1 Sample Description

Thirteen basalts were analysed, from three different ocean island groups. Nine samples are from various localities in the Tristan da Cunha group (Figure 3.1). A further two samples are from unknown localities on Réunion Island, and two samples are from the island of Fogo in the Cape Verde Islands. The sample locations, lithology and mineralogy are listed in Table 3.1.

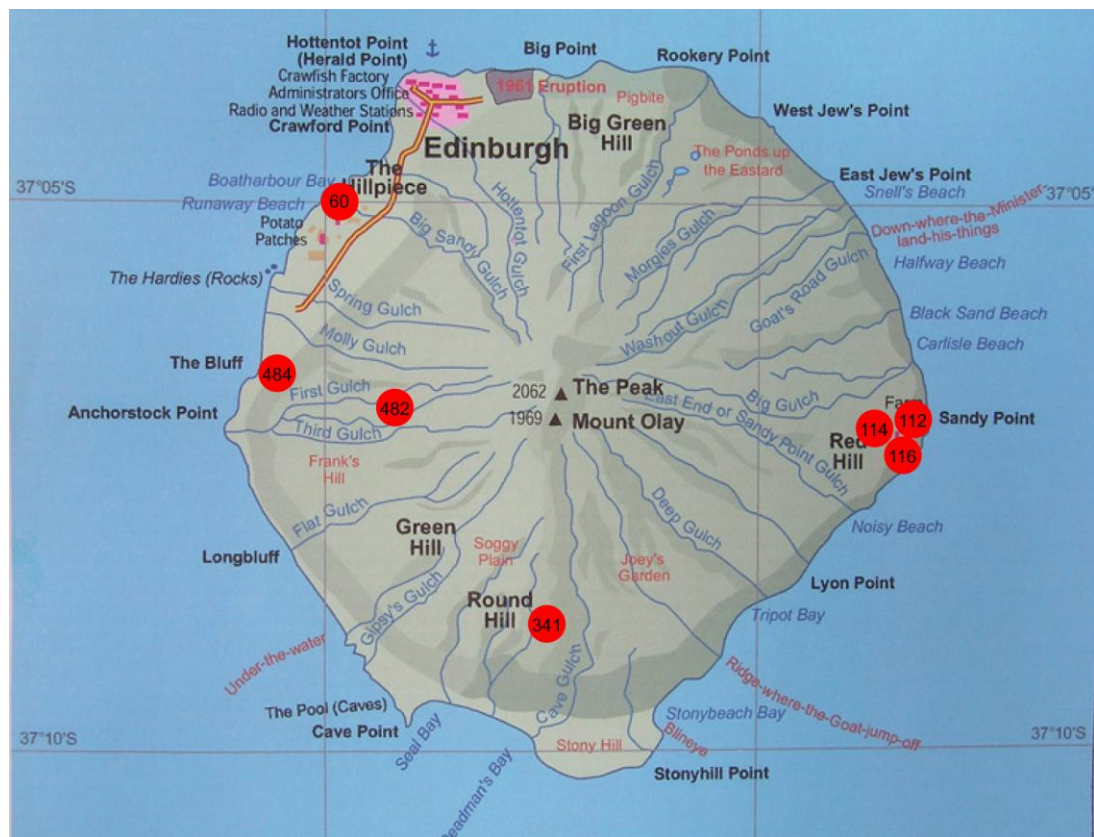


Figure 3.1 Tristan sample localities (After The Tristan da Cunha Website 2009).

##### 3.1.1 Optical Microscopy

Thin sections of the Tristan da Cunha and three of the Inaccessible samples were examined using a Nikon Optiphot2-Pol binocular transmitted light

microscope. Photomicrographs were taken using a Progres c10 *plus* camera attachment and Progres CapturePro 2.5 software.

**Table 3.1 Sample location, locality and brief description (ol = olivine, cpx = clinopyroxene, plag = plagioclase, leuc = leucite).**

<b>Sample Number</b>	<b>Locality</b>	<b>Lithology</b>	<b>Mineralogy</b>
BM 1962 128 / 60	Boulder, Boatharbour Bay, Tristan	Leucite-bearing Ankaramitic Basalt	cpx, ol, leuc + plag
BM 1962 / 112 (& BM 1962 128 / 116)	Sandy Point Flow, Tristan	Leucite-bearing Olivine Basalt	leuc, cpx, ol + plag
BM 1962 128 / 114	Boulder, Sandy Point Flow, Tristan	Ankaramitic Basalt	cpx, plag, ol
BM 1962 128 / 341	Between Round Hill and Cave Gulch, Tristan	Trachybasalt	cpx, leuc, ol + plag
BM 1962 128 / 446	Inaccessible	Vesicular Olivine Basalt	ol, plag, cpx + plag
BM 1962 128 / 473	Inaccessible	Vesicular Olivine Basalt	ol, cpx, plag + glass
BM 1962 128 / 480	Inaccessible	Picritic Basalt	ol, cpx, plag
BM 1962 128 / 482	First Gulch, Tristan	Leucite-bearing Olivine Basalt	ol, cpx, leuc + plag
BM 1962 128 / 484	Burntwood, Tristan	Leucite-bearing Vesicular Trachybasalt	cpx, ol, leuc + plag, glass
P20	Fogo	Basalt	N/A
DRE1	Réunion	Basalt	N/A
DRE2	Réunion	Basalt	N/A
FG01	Fogo	Basalt	N/A

## 3.2 Halogen and Noble Gas Analyses

The halogen and noble gas (Ar, Kr and Xe) contents of handpicked olivine grains were measured using an extension of the Ar-Ar technique and noble gas mass spectrometry. Olivine was chosen because it is one of the first phases to crystallise from a silicate melt and therefore melt inclusions within the crystals are the most representative of the deep source of the OIBs.

Prior to isotopic analysis, the samples were irradiated to generate the following neutron-induced isotopes:  $^{39}\text{Ar}_\text{K}$ ,  $^{38}\text{Ar}_\text{Cl}$ ,  $^{37}\text{Ar}_\text{Ca}$ ,  $^{80}\text{Kr}_\text{Br}$  and  $^{128}\text{Xe}_\text{I}$ , with a conversion efficiency of about 1 atom in  $10^4$  of the parent element. For halogens, the current detection limits are  $1 \times 10^{-12}\text{g}$  for I and up to three times better for Cl. The abundances of the nucleogenic isotopes were then measured and used as proxy for the parent isotopes, including Cl, Br and I. This method allows the natural noble gas isotopes (e.g.  $^{36}\text{Ar}$ ,  $^{40}\text{Ar}$ ,  $^{84}\text{Kr}$ ,  $^{129}\text{Xe}$ ) to be measured at the same time as the nucleogenic isotopes.

### 3.2.1 Neutron Irradiation

Prior to irradiation, the olivine crystals were handpicked under a binocular microscope and then washed in acetone and deionised water. The crystals were then dried and weighed, wrapped in aluminium foil and sealed in evacuated quartz tubes, together with a hornblende flux monitor of known age (Hb3gr =  $1.072 \pm 0.02$  Ga). The tubes were then irradiated in the SAFARI-1 reactor, NECSA, Pelindaba, South Africa. The samples were irradiated in two separate batches. In the initial batch, fast and thermal neutron fluxes of  $2 \times 10^{18}$  and  $7.5 \times 10^{18} \text{ n/cm}^2$  were determined using the Hb3gr flux monitors.

For the second batch the fast neutron flux was  $1.3 \times 10^{18}$  n/cm<sup>2</sup> and the thermal neutron flux was  $0.22 \times 10^{18}$  n/cm<sup>2</sup>. Irradiation transforms a small proportion of the halogens, K and Ca into the noble gas isotopes through interaction with neutrons. The abundance of the nucleogenic isotopes produced depends on the initial abundance of the parent isotope, the neutron-cross section and the neutron flux that the samples were exposed to (Table 3.2).

### **3.2.2 Noble Gas Extraction**

After irradiation, the samples were returned to Manchester and removed from the quartz tubes. The samples were then loaded into the *in vacuo* crushing device or the furnace loading system (“Christmas tree”) for extraction of the noble gases.

#### **3.2.2.1 In Vacuo Crush Release**

Four samples were crushed *in vacuo* using custom built modified Nupro<sup>®</sup> valves. Between 32.57 and 46.16 mg of sample was placed in steel crucibles and crushed using a steel pestle attached to the Nupro<sup>®</sup> valve. The noble gases were extracted from the samples using between two and four steps of increasing crushing intensity. Following extraction, the gases were purified for five minutes using an Al-Zr alloy getter at 450°C to remove active gases. The Ar, Kr and Xe gases were then trapped onto a glass finger containing activated charcoal using liquid N<sub>2</sub> (~196°C) over a period of five minutes. The charcoal finger was then heated to 120°C and the noble gases expanded into the mass spectrometer inlet manifold for a final purification

step using an Al-Zr-V getter at 200°C for a further five minutes, before being admitted to the mass spectrometer for analysis.

#### *3.2.2.2 Stepped Heating*

Crushed residues and uncrushed samples were step heated in an UHV Ta-resistance furnace for 30 minutes whilst undergoing continuous gettering. The samples were initially loaded into the furnace “Christmas tree” glass loading system and individually dropped into the furnace for extraction of the gases. Five samples were heated in six temperature steps of 200°C, over the range 600-1600°C. A further seven samples were heated in two steps of 1200°C and 1600°C. After extraction, the noble gases were purified and transferred to the mass spectrometer using the same procedure for crushing analysis.

Table 3.2 The reactions of the irradiated parent elements, producing the nucleogenic noble gas isotopes (After Kendrick 2000).

Parent	Isotopic Abundance	Reaction	Neutron Cross Section ( $\Phi_t$ )	Yield (branching)	Noble gas product	Corrections
$^{39}\text{K}$	0.9326	$^{39}\text{K}(n,p)^{39}\text{Ar}$	2.098b	1.0	$^{39}\text{Ar}$	Ca
$^{37}\text{Cl}$	0.2423	$^{37}\text{Cl}(n,\gamma)^{38}\text{Cl}(\beta)^{38}\text{Ar}$	432.9mb	1.0	$^{38}\text{Ar}$	K, ( $^{36}\text{Ar}$ )
$^{40}\text{Ca}$	0.9694	$^{40}\text{Ca}(n,\alpha)^{37}\text{Ar}$	407.5mb	1.0	$^{37}\text{Ar}$	Radioactive decay
$^{79}\text{Br}$	0.5069	$^{79}\text{Br}(n,\gamma)^{80}\text{Br}(\beta)^{80}\text{Kr}$	11.00b	0.917	$^{80}\text{Kr}$	( $^{84}\text{Kr}$ U-corrected)
$^{81}\text{Br}$	0.4931	$^{81}\text{Br}(n,\gamma)^{82}\text{Br}(\beta)^{82}\text{Kr}$	2.690b	1.0	$^{82}\text{Kr}$	( $^{84}\text{Kr}$ U-corrected)
$^{127}\text{I}$	1.0000	$^{127}\text{I}(n,\gamma)^{128}\text{I}(\beta)^{128}\text{Xe}$	6.200b	0.940	$^{128}\text{Xe}$	( $^{129}\text{Xe}$ )

Neutron Cross Section measured in barns (b) and millibarns (mb), where 1 barn =  $10^{-24}$  cm<sup>2</sup>.

### **3.2.3 Noble Gas Isotopic Analysis**

The MS1 single focussing magnetic sector mass spectrometer was used for isotopic analysis. The MS1 has a Bauer-Signer high transmission ion source, a 90-deg radius flight tube and two ion detectors, a Faraday detector and an electron multiplier. Higher abundance Ar isotope measurements are made on the Faraday detector. Less abundant Kr and Xe were measured using the electron multiplier.

The electromagnet field and data acquisition on MS1 are controlled using a FORTRAN-90 SPEC program. By adjusting the magnetic field, the program initially centres on the m/z 40 peak on the Faraday detector. Measurements of the remaining isotopes of Ar (m/z 39, 38, 37, 36) are then made by measuring their peak heights (ion current intensities) relative to this reference peak by "peak hopping". Mass peaks 35 and 41 are also measured, to detect any interference from Cl and hydrocarbons respectively. After measuring the Ar isotopes, the peak centre for  $^{80}\text{Kr}$  is then found and the other Kr isotopes (m/z 82, 84, 86) are measured by finding peaks relative to this reference peak, using the electron multiplier. Finally, the peak centre for  $^{132}\text{Xe}$  was found and measurements of the Xe isotopes (m/z 128, 129, 130, 131, 134, 136) were made relative to this reference peak, again using the electron multiplier.

Baseline readings are also measured for each of the noble gases and these are subtracted from the peak measurements during data reduction. Once all of the isotopes have been measured the scan is complete; seven scans were made of each crushing and step heating analysis taking around 45 minutes

in total. At the end of the analysis, peaks are regressed to inlet time to obtain an internally consistent set of readings.

The data were reduced using the SPEC program, which records the time that the sample was admitted to the mass spectrometer, the time of every isotopic measurement and the peak intensity measurements. Once the final scan finished, the data were reduced by extrapolation back to the inlet time ( $t = 0$ ). This is done for each isotope by plotting a graph of the time of the measurement (on the x-axis) against the value of the measurement (y-axis) and performing a regression. Anomalous points, which can occur when the mass peak has been missed (e.g. by magnetic field drift), were removed manually in order to increase the accuracy of the extrapolation.

Three different regressions were calculated for each isotope; abundance (A), ratio (R) and mean (M). For (A), a regression was performed on the abundance of the isotopes and extrapolated back to the start of the analysis to give the initial abundance of the isotopes. For (R), regression was performed on the ratio of the scarce isotope (e.g.  $^{36}\text{Ar}$ ) to an abundant reference isotope (e.g.  $^{40}\text{Ar}$ ). Using the abundance of the reference isotope at the inlet time, the abundance of the scarce isotope was then calculated. (M) calculates the mean abundance of the isotope over the period that measurements were acquired.

For the purposes of these analyses, providing (A) and (R) were in agreement, the regression with the lowest error was chosen. (M) was only chosen when (A) and (R) both returned meaningless values or high errors (e.g. when peak height did not change during the analysis).

### 3.2.3.1 Errors

Errors on the isotopic measurements are derived by the SPEC program. During each data acquisition cycle twenty readings are taken for each isotope. The isotopic measurement and its error are the mean and standard deviation of the inter-quartile range of these twenty measurements. The inter-quartile range was used in order to exclude any anomalous readings. After the seven data acquisition cycles are completed, each average measurement is then plotted against the time of the measurement and the isotopic value obtained by error-weighted least squares fitting of a line back to the inlet time.

Errors on calculated values, for example ratios and concentrations, were derived by propagating the errors from the original measurement error derived by the SPEC program.

### 3.2.4 Air Calibration

At the beginning of each day, an air calibration was run using a sample of air of known amount, in order to establish the sensitivity and mass discrimination. This gives an absolute concentration of Ar in  $\text{cm}^3/\text{div}$ , where 1 div = 10,000 volts (the absolute sensitivity is  $4 \times 10^{-4}$  amps/torr). An aliquot of air (volume  $1.071 \text{ cm}^3$ ) was extracted using a metering volume from a previously filled reservoir bottle. This air sample was purified using getters, cryogenically transferred into the mass spectrometer, and then analysed in the same way as described previously. The  $^{40}\text{Ar}$ ,  $^{84}\text{Kr}$  and  $^{132}\text{Xe}$  are measured in order to determine sensitivity. Typical sensitivities were approximately  $2 \times 10^{-12} \text{ cm}^3/\text{div}$ ,  $4 \times 10^{-15} \text{ cm}^3/\text{div}$  and  $3 \times 10^{-15} \text{ cm}^3/\text{div}$

respectively. This sensitivity is then used to convert the sample voltage measured on the mass spectrometer into cubic centimetres of gas at STP.

### **3.2.5 Blanks**

After sample loading, but prior to sample analysis, blanks were measured on the crushers and furnace. Crusher blanks were approximately  $3.0 \times 10^{-15}$  moles  $^{40}\text{Ar}$ ,  $2.31 \times 10^{-19}$  moles  $^{84}\text{Kr}$  and  $< 1.0 \times 10^{-20}$  moles  $^{129}\text{Xe}$ . Furnace blanks were approximately  $1.41 \times 10^{-11}$  moles  $^{40}\text{Ar}$ ,  $3.4 \times 10^{-18}$  moles  $^{84}\text{Kr}$  and  $1.1 \times 10^{-18}$  moles  $^{129}\text{Xe}$ . Blank corrections were not applied as these measurements represented only 0.1-10% of the amount of noble gases released from the samples.

### **3.2.6 Data Reduction**

After regression using the SPEC program was complete, the raw data were input into an Excel spreadsheet and then corrected for mass discrimination,  $^{37}\text{Ar}_{\text{Ca}}$  decay, neutron interference reactions and  $^{38}\text{Ar}_{\text{Cl}}$  interference respectively.

#### **3.2.6.1 Mass Discrimination**

The MS1 spectrometer favours the heavier isotope of Ar,  $^{40}\text{Ar}$  (as the heavier ions have slightly more kinetic energy), and therefore reports a higher ratio of  $^{40}\text{Ar}/^{36}\text{Ar}_{\text{air}}$  during air calibration. The atmospheric argon ratio measured was typically in the range of 297-300. The difference in the air calibration ratio and the known air ratio of 295.5 is then used to normalise the sample measurements of  $^{36}\text{Ar}$ ,  $^{38}\text{Ar}$  and  $^{39}\text{Ar}$ , with the  $^{40}\text{Ar}$  measurements remaining unchanged.

### 3.2.6.2 $^{37}\text{Ar}_{\text{Ca}}$ Correction

As the first samples analysed were irradiated more than a year before analysis, no corrections were made for  $^{37}\text{Ar}$  decay, as this isotope had already decayed (half-life is 35.1 days). A correction due to the decay of  $^{37}\text{Ar}$  was made on the second batch of samples which were analysed approximately two months after irradiation. The conversion of  $^{40}\text{Ca}$  to  $^{37}\text{Ar}$  was monitored using the hornblende Hb3gr standard for which the Ca content is known.

### 3.2.6.3 Neutron Interference Corrections

During irradiation, additional amounts of some Ar isotopes are produced via interfering reactions. Pure zero-age salts of potassium sulphate ( $\text{K}_2\text{SO}_4$ ) and calcium fluoride ( $\text{CaF}_2$ ) were irradiated with the samples to measure the production rate of Ar from interfering isotope reactions. Isotopic ratios determined from the salts were as follows:  $^{38}\text{Ar}/^{39}\text{Ar}_{\text{salt}} = 0.01241$ ;  $^{40}\text{Ar}/^{39}\text{Ar}_{\text{salt}} = 0.033$ ;  $^{39}\text{Ar}/^{37}\text{Ar}_{\text{salt}} = 0.0007447$ ; and  $^{36}\text{Ar}/^{37}\text{Ar}_{\text{salt}} = 0.0002692$ . The magnitude of the corrections was  $< 1\%$  of the total for each of the Ar isotopes involved.

### 3.2.6.4 Cl Correction

In order to determine the proportion of  $^{38}\text{Ar}$  measured which was produced from  $^{37}\text{Cl}$ , a calculation was made to derive the  $^{38}\text{Ar}^*$  from  $^{38}\text{Ar}_{\text{total}}$ . As the mantle has the same  $^{38}\text{Ar}/^{36}\text{Ar}$  ratio as air (0.188), the measured  $^{36}\text{Ar}$  is used together with this ratio to determine the  $^{38}\text{Ar}^*$  present in the sample. The magnitude of the corrections was typically  $< 10\%$  of the total released.

A further correction is made on  $^{36}\text{Ar}$ , which is produced from the decay of  $^{36}\text{Cl}$ .  $^{36}\text{Cl}$  is produced via neutron capture and gamma decay of  $^{35}\text{Cl}$  during irradiation. Although  $^{36}\text{Cl}$  decays slowly due to its long half-life of  $301,000 \pm 4,000$  years, if there are large amounts of Cl present in a sample, and a long delay ( $> 1$  year) between irradiation and analysis, a significant amount of  $^{36}\text{Ar}$  can still be produced between irradiation and analysis as  $^{35}\text{Cl}$  is the most abundant isotope of Cl. This correction was small, with all values being corrected by  $< 0.01\%$  of their original value.

### ***3.2.7 Conversion of the Noble Gases to the Halogens, K and Ca***

In order to convert the noble gas abundances into their parent isotope concentrations, a conversion factor is determined using a standard of known composition. Br and I abundances were determined based on conversions from the 2320quartz monitor, which has known Br and I content. The hornblende Hb3gr standard was used to obtain a conversion factor to enable the calculation of the remaining parent isotope concentrations.

## 4 Results and Discussion

### 4.1 Petrography

Thin sections were analysed for the six Tristan basalts and the three Inaccessible Island basalts, with a total of ten sections available (including one from a related Tristan sample, BM 1962 128 / 116) (Figure 3.1). Brief descriptions follow, with further details in Appendix A. A full list of all the photomicrographs can also be found in Appendix B. All of the samples analysed optically are porphyritic, indicative of at least two phases of crystallisation; prior to eruption and during cooling post eruption.

#### 4.1.1 *BM 1962 128 / 60 (Tristan)*

Rock Type: Leucite-bearing Ankaramitic Basalt

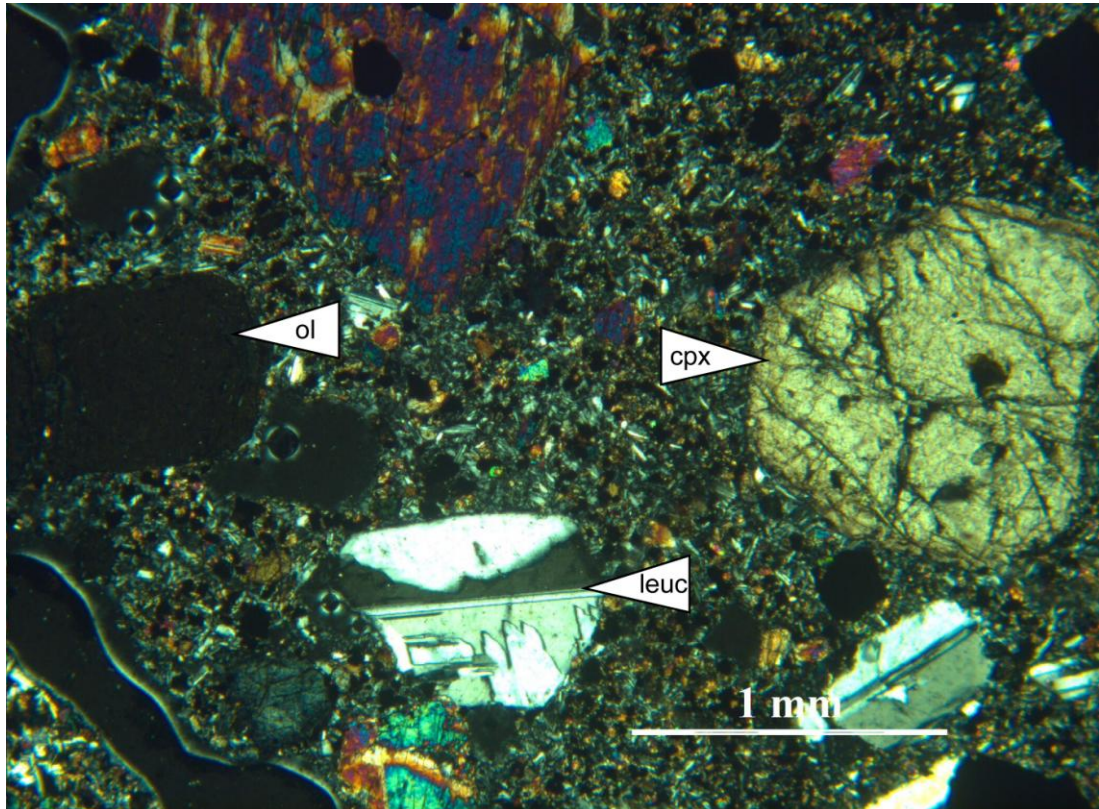


Figure 4.1 Showing resorbed olivine (ol), zoned clinopyroxene (cpx) and multiply twinned leucite (leuc) under crossed-polars.

Phenocrysts of clinopyroxene, olivine and leucite are present, in a vesicular groundmass of opaque minerals, fragmentary crystals and glass (Figure 4.1). The sample has an inequigranular porphyritic texture, with no preferred orientation or vesicles observed. All the phenocrysts are subhedral to anhedral, fragmentary and range in size from 1-6 mm. Plagioclase is also present both as subhedral inclusions within clinopyroxene crystals and as laths within the groundmass. Fluid inclusions appear rare, but are present in some olivine phenocrysts.

The fragmentary nature of this sample, together with its locality (sampled from a boulder on the beach in Boatharbour Bay) suggests that this sample may be an ejected bomb from a pyroclastic eruption.

#### 4.1.2 BM 1962 128 / 112 (Tristan)

Rock Type: Leucite-bearing Olivine Basalt

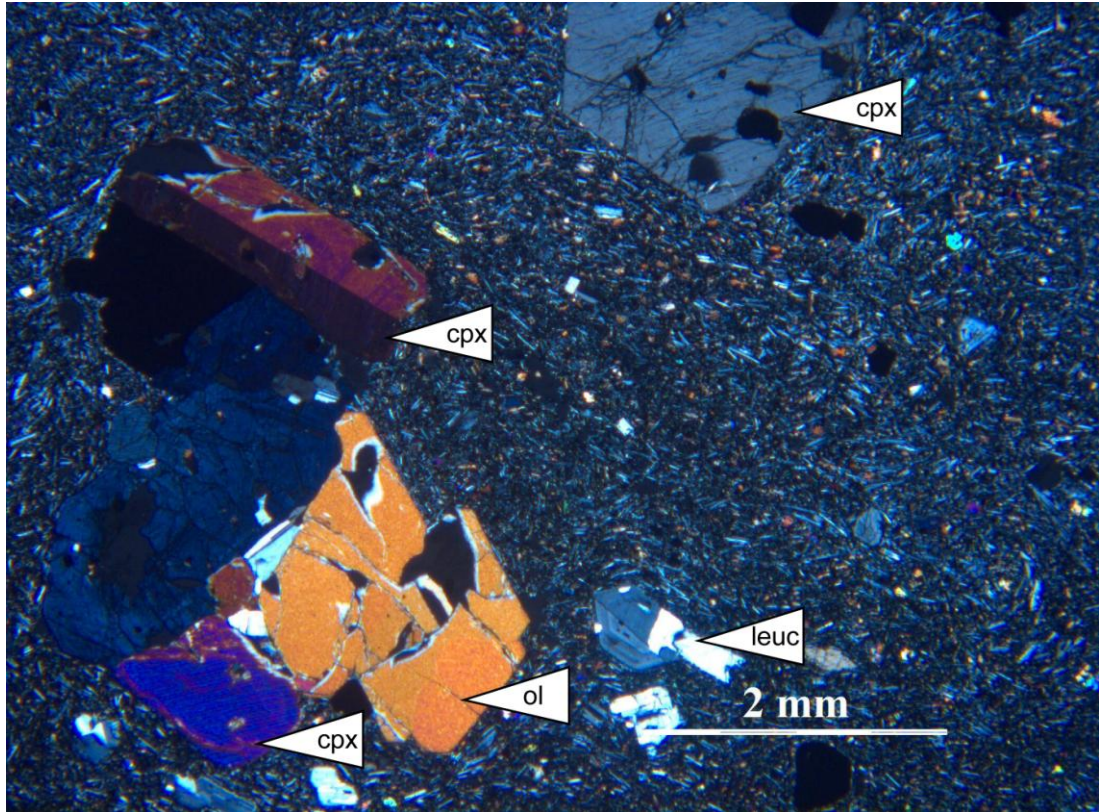


**Figure 4.2** Showing magma inclusions and twinning within clinopyroxene, and mineral preferred orientation within the groundmass.

This sample has a strong preferred orientation, highlighted by plagioclase laths within the matrix (Figure 4.2). The matrix also contains opaques and smaller clinopyroxene crystals. The texture is inequigranular porphyritic with phenocrysts ranging in size from 1-4 mm and comprising of leucite, clinopyroxene and olivine, in order of decreasing abundance. Plagioclase laths within the matrix are aligned around the phenocrysts, indicating that the preferred orientation is as a result of flow processes. Melt inclusions are present within the olivine crystals.

It is possible that this sample may have been collected from a dyke, as sample 116 represents the chilled margin of this sample, and flow alignment is observed.

#### 4.1.3 *BM 1962 128 / 114 (Tristan)*

Rock Type: Ankaramitic Basalt

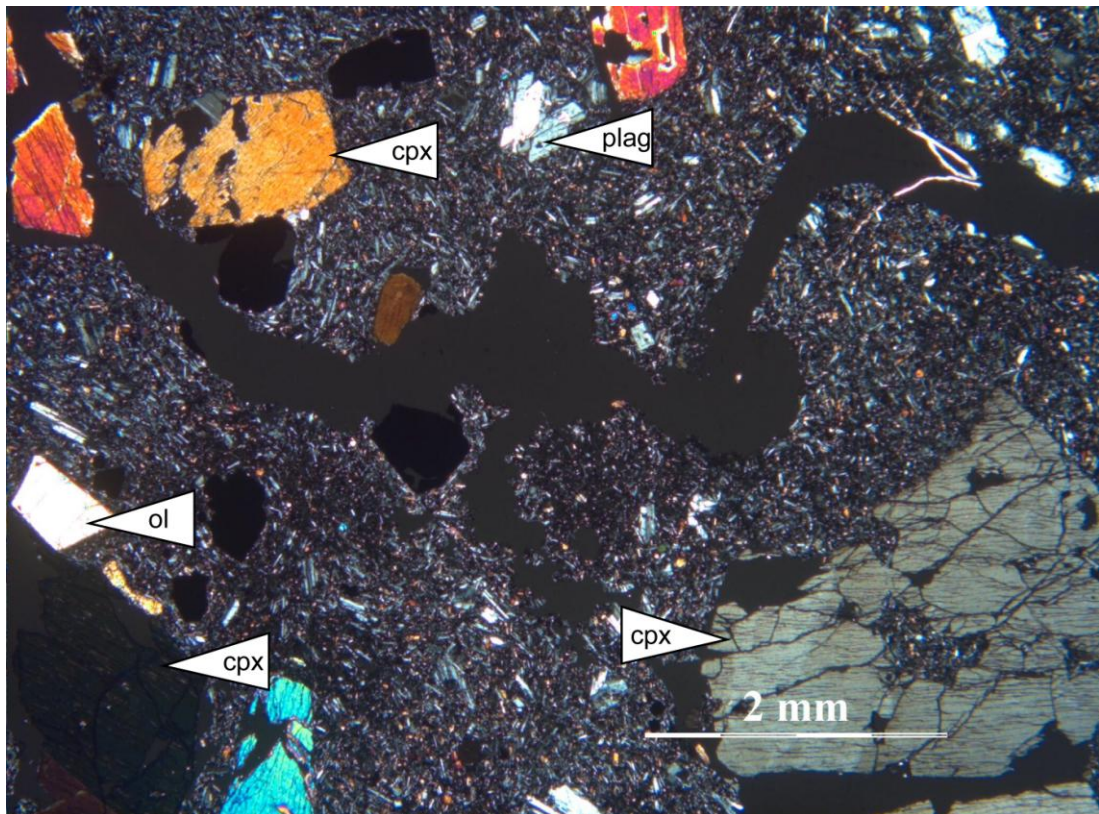


**Figure 4.3** Showing weak preferred orientation and porphyritic texture. Note damage to thin section.

Phenocrysts of clinopyroxene, opaques and plagioclase are present, together with rare olivine crystals. The groundmass is fine-grained, comprising approximately 85% of the sample and contains plagioclase and opaques. The texture is porphyritic inequigranular, with phenocrysts ranging in size from 1-3 mm. The groundmass exhibits a weak preferred orientation (Figure 4.3).

Many of the phenocrysts are resorbed and fractured. The sample was collected from a boulder and thus the fracturing may indicate that the boulder was ejected as a bomb during eruption.

#### **4.1.4 BM 1962 128 / 116 (Tristan)**

Rock Type: Leucite-bearing Olivine Basalt

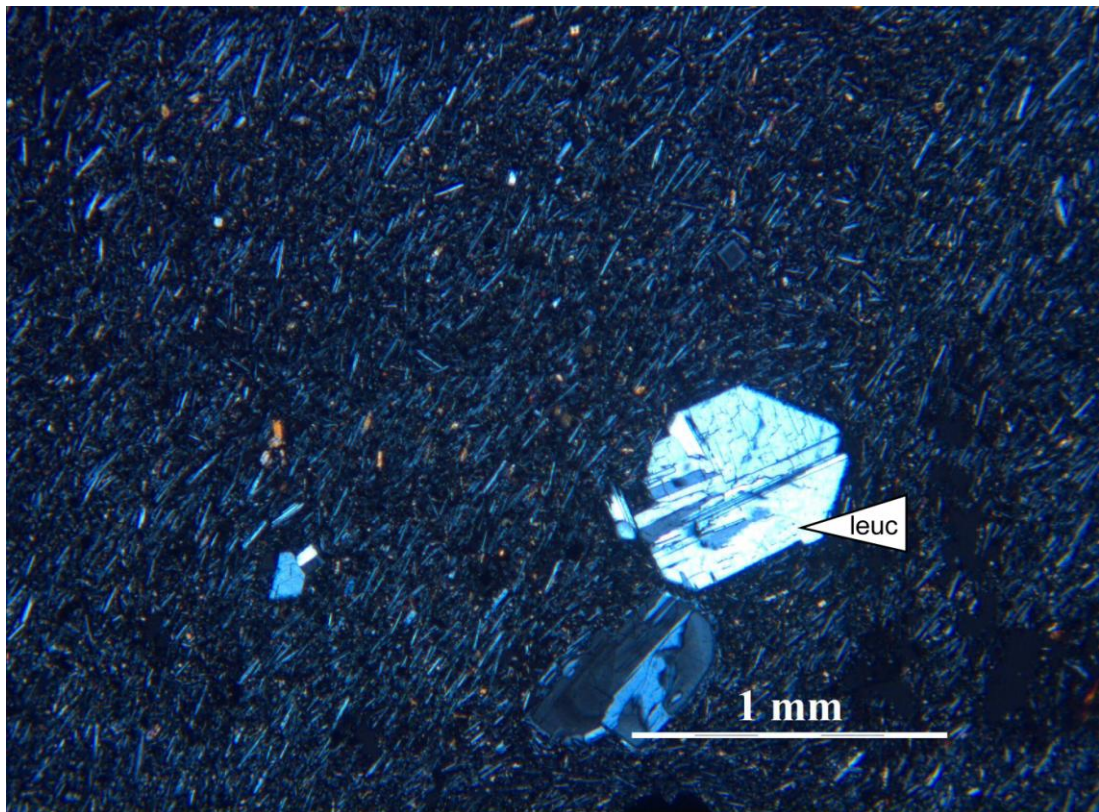


**Figure 4.4 Showing preferred orientation.**

Although this specimen was not analysed isotopically, it is geologically related to sample 112, being a sample from the chilled margin of the same dyke that 112 was collected from. It is mineralogically similar, with phenocrysts of olivine, leucite, plagioclase and clinopyroxene present, and also exhibits a strong preferred orientation (Figure 4.4). The phenocrysts range from 0.5-2 mm and are far less abundant than in the related sample,

112. The groundmass represents about 95% of the total sample, with plagioclase laths in the matrix highlighting the preferred orientation.

This sample is related to 112 and is thought to be collected from a chilled margin of a dyke.

#### **4.1.5 BM 1962 128 / 341 (Tristan)**

Rock Type: Trachybasalt

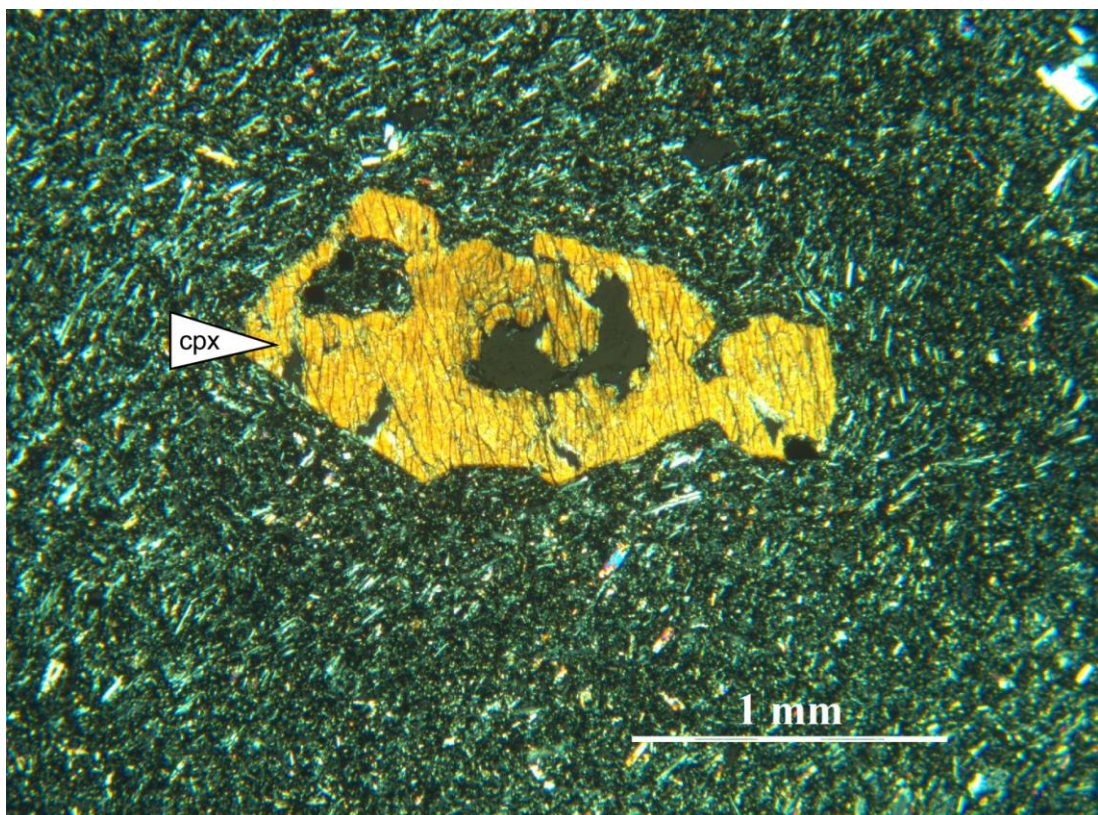


**Figure 4.5 Showing resorbed clinopyroxene phenocryst and preferred orientation within the matrix.**

Phenocrysts of clinopyroxene, leucite and olivine are present within a very fine-grained groundmass, which exhibits preferred orientation (Figure 4.5). The texture is inequigranular porphyritic, with phenocrysts ranging in size from 1-2 mm. Many of the phenocrysts are resorbed and subhedral, but some are euhedral. Quenched lava clots are present within the matrix, which

comprise mainly of plagioclase laths which “flow” around the larger crystals, in addition to opaques and glass. Fluid inclusions are rare, but present in both the clinopyroxene and the olivine phenocrysts.

Due to its proximity to the Round Hill scoria cone, and the presence of flow textures, it is possible that this sample is from the lava field associated with the scoria cone.

#### **4.1.6 BM 1962 128 / 446 (Inaccessible)**

Rock Type: Vesicular Olivine Basalt

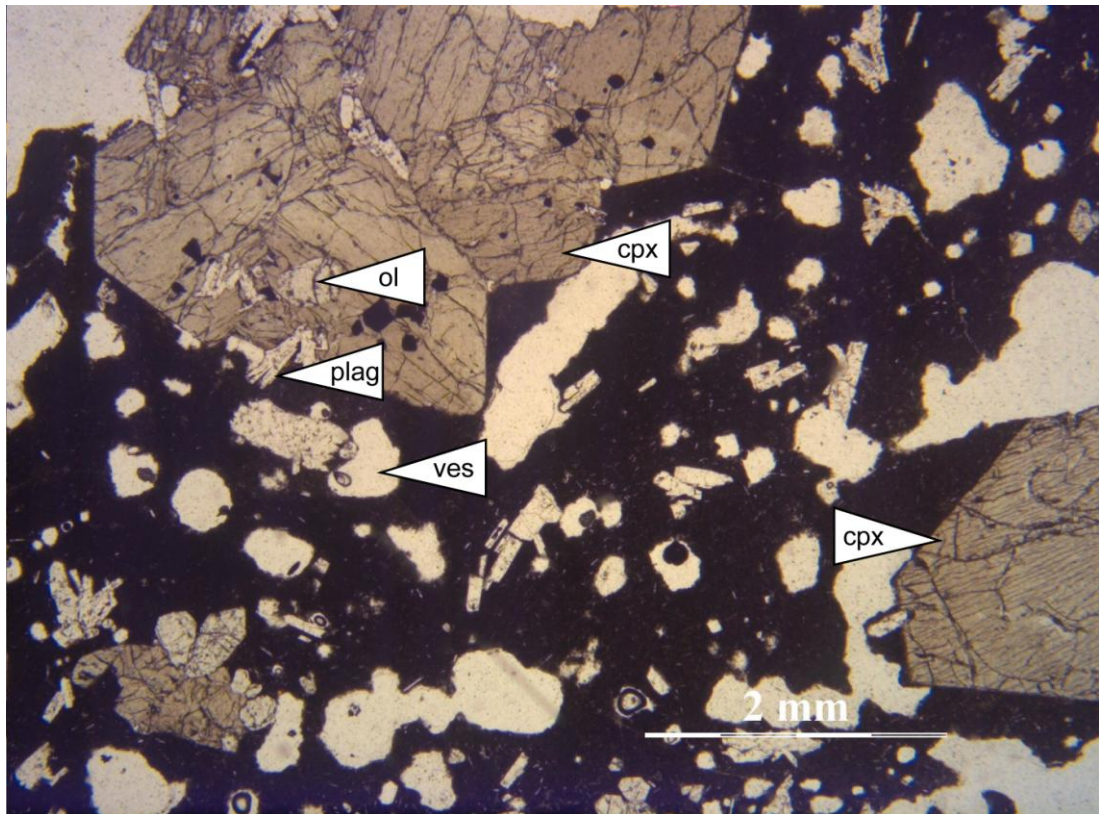


**Figure 4.6 Showing vesicular texture.**

Phenocrysts of olivine, plagioclase and clinopyroxene make up 50% of the sample, with the remainder being vesicles and a matrix of glass and plagioclase (Figure 4.6). Many of the vesicles have coalesced with their neighbours, and are elongated, ranging from 0.2-3 mm in size. The texture is

vesicular porphyritic, with phenocrysts ranging in size from 1-8 mm, the larger being clinopyroxene and the smaller are plagioclase laths.

Texturally, this sample is very different to the others discussed previously, with the abundance of vesicles suggesting that the eruption style was more explosive. Early eruptions on Tristan were more gaseous strombolian type eruptions, compared to the later eruptions from secondary centres which tended to be effusive in nature. This suggests that Inaccessible Island volcanism may have been similar to the early Tristan volcanism.

#### **4.1.7 BM 1962 128 / 473 (Inaccessible)**

Rock Type: Vesicular Olivine Basalt

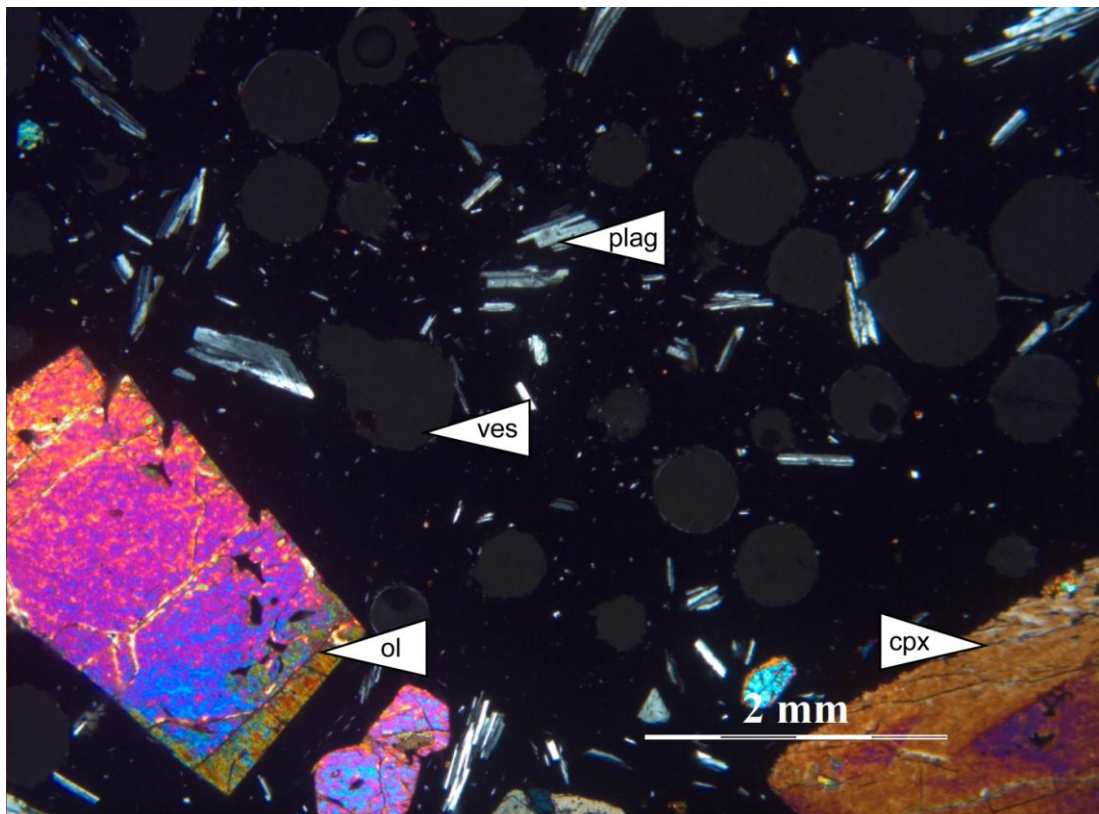


**Figure 4.7 Showing vesicular texture and alternation of olivine rim to serpentine.**

The groundmass is glassy and dominates, being ~60% of the sample. Phenocrysts of olivine, clinopyroxene and plagioclase are present, and are

euohedral or subhedral. Some of the olivines are resorbed, or show slight alteration to serpentine (Figure 4.7). Many of the crystals exhibit zoning and are fractured, indicating an explosive eruption. This is consistent with the presence of vesicles, which are usually individual, rarely coalesced, and approximately 1 mm in diameter. A high density of magma inclusions is observed within the olivine phenocrysts, 1-9 mm crystal size; there also appears to be rarer fluid inclusions present. Exsolution is present within the clinopyroxene crystals, which are 1-5 mm long. Plagioclase laths are 2 mm and show random orientation.

The texture is vesicular porphyritic. Again, the fracturing and vesicles indicate a more gaseous eruption style than observed in the Tristan samples.

#### 4.1.8 BM 1962 128 / 480 (Inaccessible)

Rock Type: Picritic Basalt

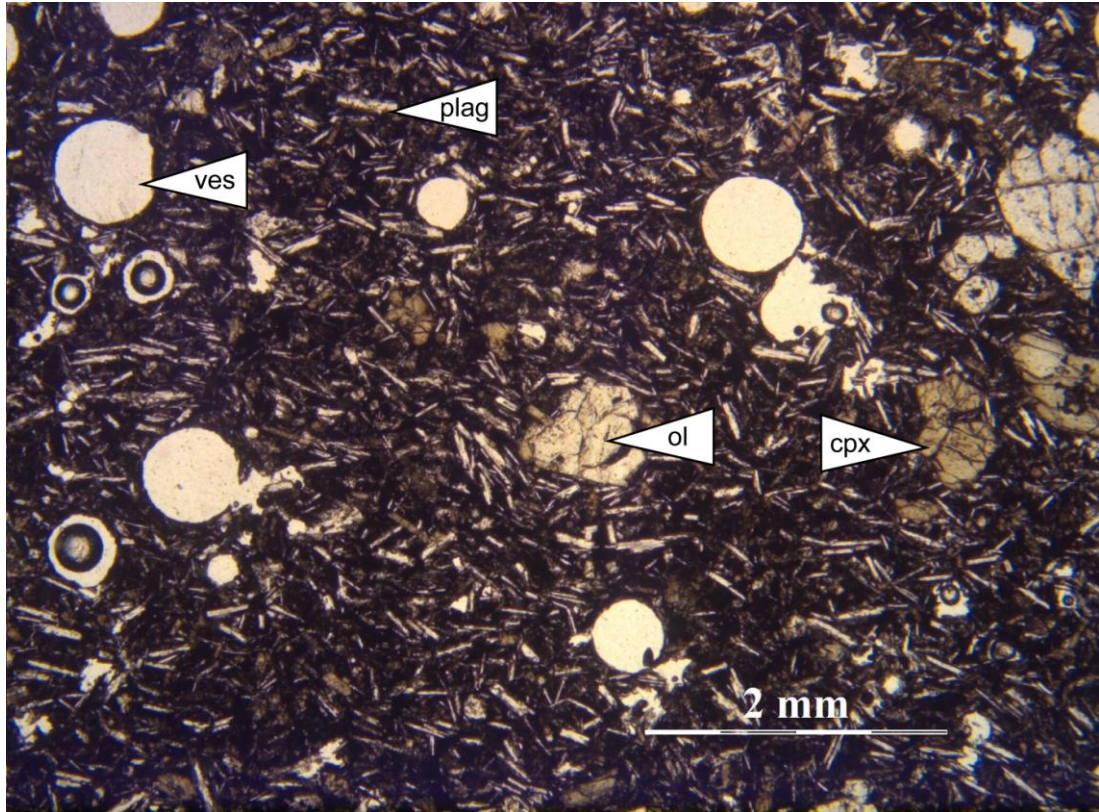


**Figure 4.8 Showing vesicular texture and preferred orientation.**

The sample comprises of phenocrysts of olivine, clinopyroxene and plagioclase in a very fine-grained groundmass. The abundant plagioclase laths show a preferred orientation; some show alteration to clay minerals around their crystal edges (Figure 4.8). The phenocrysts vary in size from 2-4 mm, are euhedral to subhedral, with some fractured crystals. Magma inclusions are present within the olivine crystals.

Vesicles are present, 1 mm in diameter, and are mainly round with rare ones coalescing. The texture is vesicular porphyritic inequigranular, with some evidence of flow banding. The fracturing of crystals, together with the

presence of vesicles suggest that this sample was erupted in a similar style to early Tristan volcanism.

#### 4.1.9 *BM 1962 128 / 482 (Tristan)*

Rock Type: Leucite-bearing Olivine Basalt

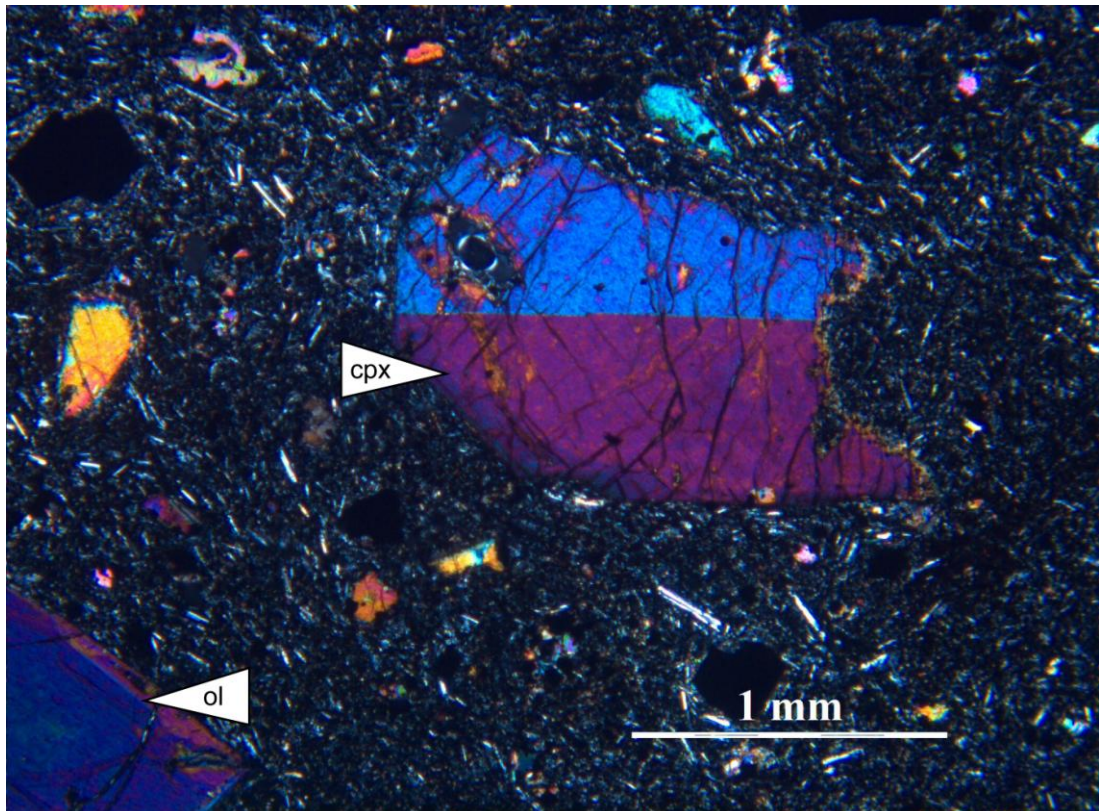


**Figure 4.9 Showing twinned and resorbed clinopyroxene phenocryst.**

Phenocrysts of olivine, clinopyroxene and leucite are present, ranging in size from 1-5 mm. Some crystals are resorbed or fractured (Figure 4.9). The olivine phenocrysts are strongly coloured, suggesting that they are forsterite. Zoning is also present within the olivine crystals, with the stronger colour within the core, reflecting an evolving parental magma composition towards fayalite. The groundmass contains randomly orientated plagioclase laths.

Although selected for analysis, this sample was not analysed geochemically due to technical problems.

#### 4.1.10 BM 1962 128 / 484 (Tristan)

Rock Type: Leucite-bearing Vesicular Trachybasalt

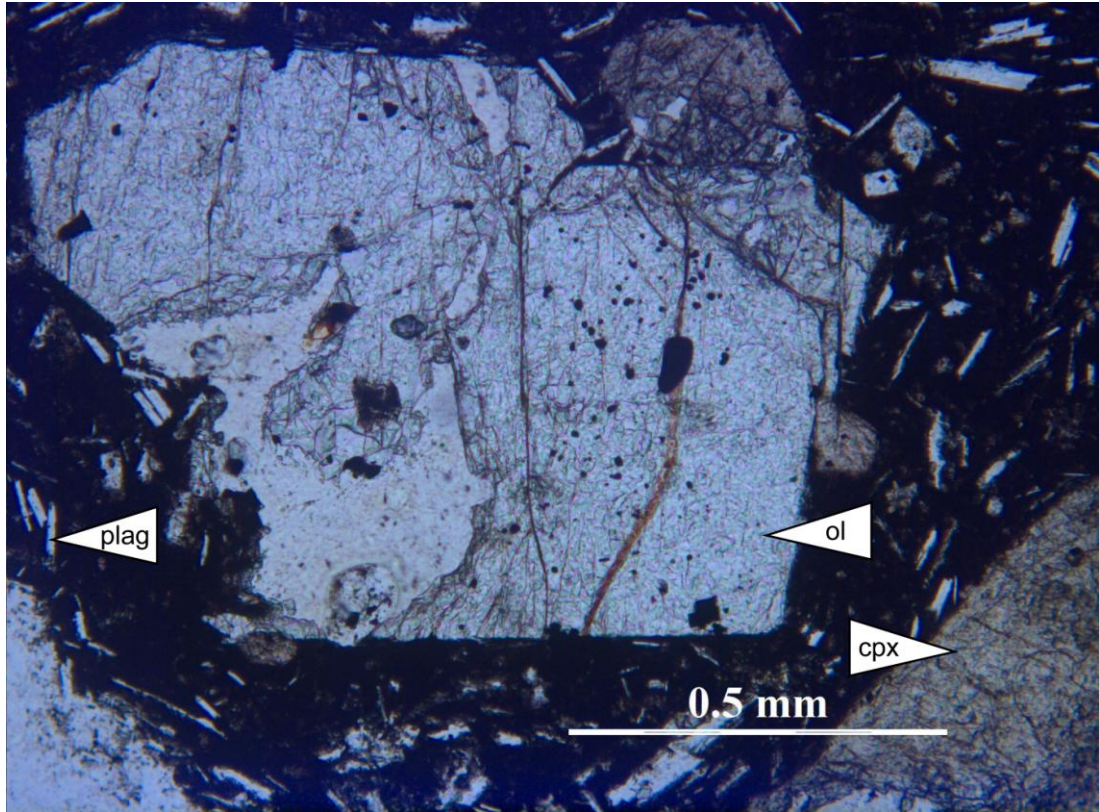


**Figure 4.10 Showing magma inclusions within an olivine phenocryst.**

The groundmass comprises of plagioclase and glass, and shows a weak preferred orientation. Vesicles are present, with a diameter of ~2 mm. Many of the vesicles have coalesced with a neighbouring vesicle. The texture is porphyritic, with phenocrysts of clinopyroxene, olivine and leucite present. These range in size from 1-3 mm, with rare resorption and both fluid and magma inclusions present, both along fractures and within the crystal itself (Figure 4.10).

The presence of vesicles suggests that this sample is from an early stage of volcanic activity on the island.

## **4.2 The Halogens and K**

### **4.2.1 Release Patterns**

Four samples were subjected to both crushing and stepped heating of the crushed powders. Noble gases were extracted from these samples using 600-1600°C heating steps. Total halogen releases from crushing was approximately an order of magnitude lower than the total releases observed during stepped heating, and in the case of K, the stepped heating releases were up to two orders of magnitude higher.

With the exception of samples 473 (Inaccessible) and 446 (Inaccessible), two major releases were observed during step heating at between 800-1200°C and at 1600°C respectively (Figure 4.11). The lower temperature release accounts for approximately 80-90% of the total Cl, Br and I released from each sample, with the highest temperature step yielding up to 20% of the total released. The major I release in samples 473 (Inaccessible) and 446 (Inaccessible) was in a single release at 1000°C. Most of the total K (85-94%) was released in the lower temperature steps, up to and including the 1200°C step, and in some samples, most of the K was released during the 1000°C step.

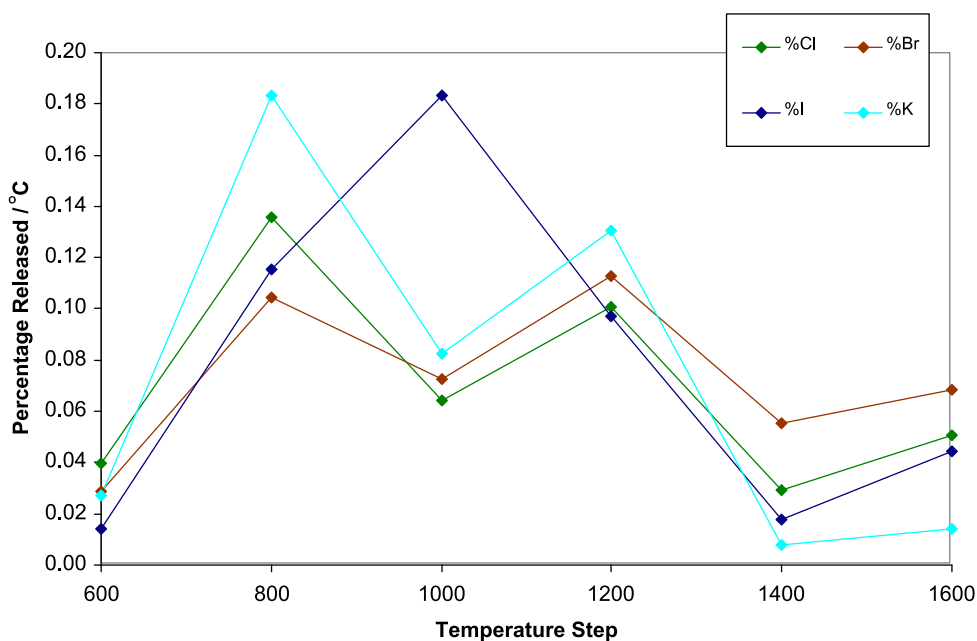


**Figure 4.11 Percentage release of Cr, Br, I and K during stepped heating of sample 473 (Inaccessible) (other samples show similar release patterns, see Appendix C).**

In view of these release patterns, the remaining samples were heated in two temperature steps of 1200°C and 1600°C.

The halogens Br, Cl and I, and K are incompatible elements, which will partition into the melt phase during crystallisation or partial melting. As such, they are not readily accommodated within the crystal lattice of olivine and their concentrations will be low in this mineral. As the melting temperature for olivine is relatively high, ranging from approximately 1200-1900°C, and most of the release occurred prior to the 1200°C step, this confirms that we are not observing a release of Cl, Br, I and K from within the crystal structure.

Alternative sources include melt/fluid inclusions and secondary alteration phases of olivine. Petrographical analysis showed very little alteration of olivine, with the exception of a single sample 473 (Inaccessible). This sample shows similar Br/Cl ratios to other samples (approximately  $3 \times 10^{-3}$ ), but has higher K content. However this sample was also observed to have a high

population density of melt inclusions suggesting an alternative site for halogens. Melt inclusions were observed in most of the olivine crystals present in the samples, and it is therefore expected that the majority of the released Cl, Br, I and K comes from parental magma inclusions trapped within the host olivine crystals. In support of a melt inclusion host for halogens, Koleszar *et al.* (2009) determined up to 185 and 2,000 ppm Cl and K respectively in melt inclusions from Fernandina and Santiago Islands in the Galápagos Archipelago. Variations in concentration of halogens and K between samples may be partly attributed to inter-sample variations in the number of inclusions.

The petrography revealed the possibility of several inclusion assemblages, including primary inclusions trapped during crystal growth and secondary inclusions, which appear to have become trapped during the healing of crystal fractures after the crystal formed. This may account for the two separate temperature releases, however it may also be due to different types of fluid inclusions as some appear optically to be fluid inclusions, whereas some inclusions appear to be primarily formed from the parental magma.

The variation in Br/Cl and I/Cl values with temperature is more complex. For the four samples that were initially analysed, three (112 (Tristan), 114 (Tristan) and 480 (Inaccessible)) show the Br/Cl ratio peaking at 1000°C, with the I/Cl ratio peaking slightly later, at 1000-1200°C (Figure 4.12). Samples 446 (Inaccessible) and 473 (Inaccessible) both show two peaks for Br/Cl, ranging from  $(2 - 9) \times 10^{-3}$ .

As the ratios do not remain constant, this suggests that halogens are being released from two or more types of compositionally distinct inclusions. The lower temperature release may be related to the healed fracture (secondary) inclusions, whereas the high temperature release could be from primary inclusions. Alternatively, the releases could be from different types of inclusions, for instance fluid and magmatic inclusions.

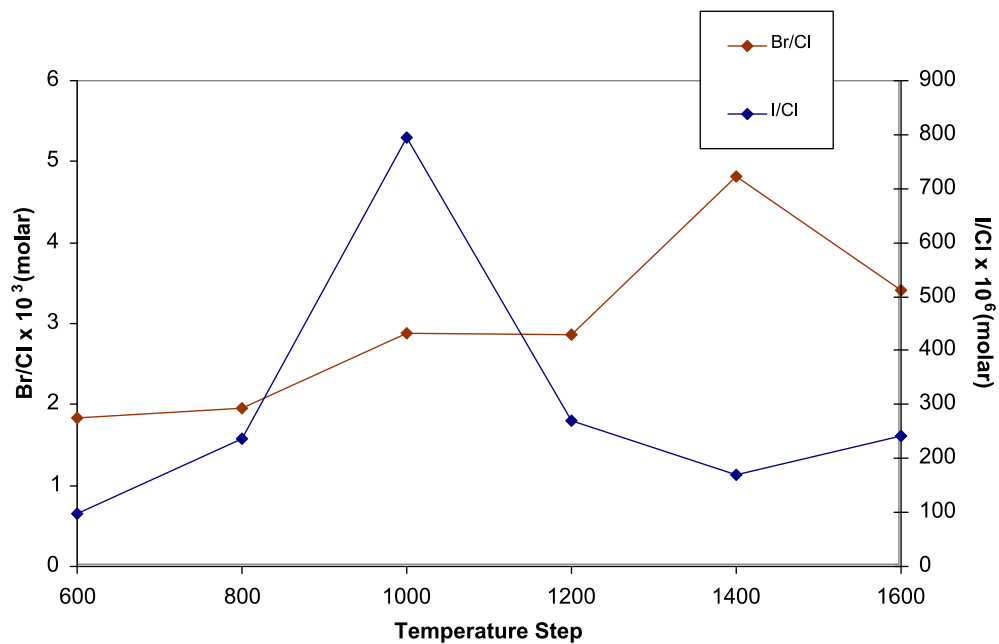


**Figure 4.12** Showing the variation in Br/CI and I/CI with temperature (in °C) (sample 473 (Inaccessible); see Appendix C for other samples).

The variation in K/CI with temperature is again complex, and differs for each sample analysed (Figure 4.13). Most samples show a relatively flat profile, with little variation over the temperature steps, indicating that the release is either from one generation of inclusions or that the ratio is constant in different inclusion assemblages. However, samples 114 (Tristan) and 480 (Inaccessible) show a peak in K/CI around the 800°C step. This suggests that K/CI value may vary in different inclusion assemblages, as the ratio decreases to a constant value in the later temperature steps.

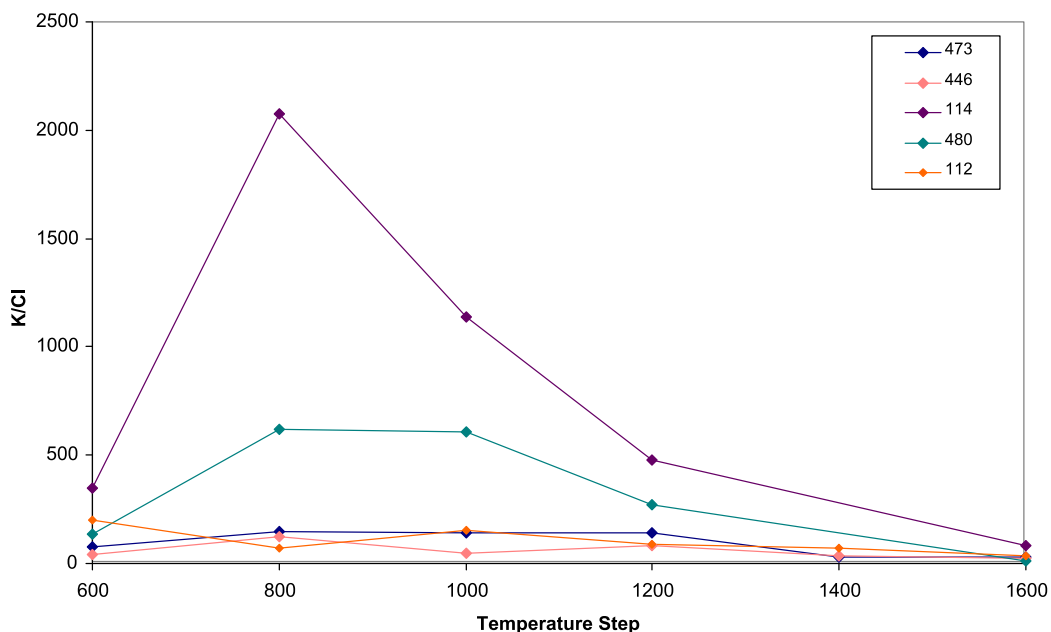


Figure 4.13 Showing the variation in K/Cl with temperature (in °C).

#### 4.2.2 Cl, Br, I and K Relationships

Plots of Br, I and K concentrations against Cl concentrations are shown for the Tristan and Inaccessible samples (Figure 4.14 - Figure 4.16; data shown in Table 4.1). Total release values were obtained by summing all the individual releases measured from both crushing and step heating for each sample.

For the samples which were both crushed and heated, the gas released from heating shows a greater concentration of halogens; crushing releases range from 15-29% of the total Cl released, 18-23% of the total Br, 5-11% of the total I, and 1-7% of the total K.

The total amount of Br released from the individual samples ranges from 2-46 ppb (Figure 4.14). Cl ranges from 0.37-9 ppm. Br/Cl values range from  $(1.7-8.3) \times 10^{-3}$ .

Figure 4.14 shows that individual samples show linear correlations for Br and Cl, suggesting that both the elements are released from the same sites in the olivine and are not significantly fractionated from each other. The higher concentrations seen in samples 473 (Inaccessible) and 484 (Tristan) may be due to the greater density of melt inclusions observed optically in these samples.

**Table 4.1 Tristan, Inaccessible, Fogo and Réunion halogen and K data.**

Sample	Weight (mg)	Method	Temperature / # of steps	Cl (ppm)	Br (ppb)	I (ppb)	K (ppm)	Br/Cl (10 <sup>-3</sup> )	I/Cl (10 <sup>-3</sup> )	
60	64.10	Step Heating	1200°C	0.708 ± 0.186	1.254 ± 0.030	0.114 ± 0.021	30.273 ± 0.073	0.787 ± 0.207	0.045 ± 0.014	
			1600°C	0.856 ± 0.298	1.982 ± 0.041	0.187 ± 0.037	36.513 ± 0.078	1.028 ± 0.358	0.061 ± 0.024	
		<b>Total</b>		<b>1.564 ± 0.351</b>	<b>3.235 ± 0.051</b>	<b>0.300 ± 0.042</b>	<b>66.786 ± 0.107</b>	<b>0.919 ± 0.207</b>	<b>0.054 ± 0.014</b>	
112	32.81	Step Heating	600°C	0.538 ± 0.082	0.882 ± 0.055	0.133 ± 0.049	119.138 ± 0.999	0.729 ± 0.120	0.069 ± 0.028	
			800°C	1.188 ± 0.183	2.035 ± 0.088	0.227 ± 0.061	94.782 ± 0.813	0.761 ± 0.122	0.053 ± 0.017	
			1000°C	0.209 ± 0.040	1.914 ± 0.087	0.122 ± 0.043	35.636 ± 0.354	4.069 ± 0.792	0.163 ± 0.066	
			1200°C	0.455 ± 0.074	2.525 ± 0.149	0.108 ± 0.040	44.820 ± 0.435	2.465 ± 0.424	0.066 ± 0.026	
			1400°C	0.416 ± 0.066	2.142 ± 0.240	0.232 ± 0.094	31.440 ± 0.307	2.290 ± 0.444	0.156 ± 0.068	
			1600°C	0.209 ± 0.034	0.765 ± 0.272	0.160 ± 0.051	8.631 ± 0.122	1.628 ± 0.638	0.215 ± 0.077	
		<b>Total</b>		<b>3.014 ± 0.230</b>	<b>10.263 ± 0.415</b>	<b>0.983 ± 0.145</b>	<b>334.447 ± 1.443</b>	<b>1.51 ± 0.131</b>	<b>0.091 ± 0.015</b>	
114	34.81	Crushing	#1	0.045 ± 0.007	nd	nd	0.558 ± 0.134	nd	nd	
			#20	0.098 ± 0.036	nd	nd	10.162 ± 0.199	nd	nd	
	16.15	Step Heating	600°C	0.457 ± 0.091	1.708 ± 0.068	0.102 ± 0.037	174.580 ± 1.719	1.659 ± 0.338	0.062 ± 0.026	
			800°C	0.168 ± 0.031	1.120 ± 0.069	0.120 ± 0.042	382.659 ± 3.187	2.968 ± 0.575	0.200 ± 0.079	
			1000°C	0.055 ± 0.026	0.756 ± 0.058	nd	69.346 ± 0.842	6.076 ± 2.881	nd	
			1200°C	0.065 ± 0.033	0.589 ± 0.043	0.157 ± 0.046	34.325 ± 0.483	4.004 ± 0.206	0.672 ± 0.390	
			1400°C	nd	0.483 ± 0.069	0.095 ± 0.012	4.808 ± 0.261	nd	nd	
			1600°C	0.057 ± 0.020	0.291 ± 0.049	0.057 ± 0.016	5.208 ± 0.333	2.258 ± 0.867	0.278 ± 0.124	
			<b>Total</b>		<b>0.947 ± 0.143</b>	<b>4.945 ± 0.148</b>	<b>0.530 ± 0.075</b>	<b>681.648 ± 4.012</b>	<b>1.974 ± 0.243</b>	<b>0.133 ± 0.025</b>
	341	47.5	Step Heating	1200°C	nd	1.266 ± 0.041	0.156 ± 0.091	14.803 ± 1.600	nd	nd
1600°C				nd	nd	nd	4.371 ± 0.412	nd	nd	
		<b>Total</b>		<b>nd</b>	<b>1.266 ± 0.041</b>	<b>0.156 ± 0.091</b>	<b>19.174 ± 1.652</b>	<b>nd</b>	<b>nd</b>	
446	38.25	Crushing	#1	0.141 ± 0.024	0.625 ± 0.028	0.250 ± 0.047	1.667 ± 0.081	1.969 ± 0.344	0.496 ± 0.126	
			#3	0.044 ± 0.024	0.177 ± 0.019	0.220 ± 0.045	0.451 ± 0.072	1.805 ± 1.017	0.141 ± 0.833	
			#10	0.083 ± 0.016	0.635 ± 0.063	0.656 ± 0.087	0.840 ± 0.128	3.407 ± 0.745	2.214 ± 0.523	
			#20	0.176 ± 0.032	1.049 ± 0.072	1.057 ± 0.141	1.206 ± 0.080	2.643 ± 0.518	1.676 ± 0.380	
	22.46	Step Heating	600°C	0.487 ± 0.076	4.151 ± 0.138	6.223 ± 0.789	23.111 ± 0.273	3.789 ± 0.608	3.574 ± 0.725	
			800°C	0.110 ± 0.029	2.266 ± 0.153	4.153 ± 0.544	15.328 ± 0.233	9.149 ± 2.468	10.551 ± 3.083	
			1000°C	0.116 ± 0.029	1.210 ± 0.196	7.942 ± 1.031	6.303 ± 0.273	4.621 ± 1.389	19.087 ± 5.431	
			1200°C	0.064 ± 0.018	0.416 ± 0.051	3.727 ± 1.199	5.591 ± 0.178	2.905 ± 0.899	16.357 ± 7.026	
			1400°C	0.104 ± 0.050	1.054 ± 0.055	0.764 ± 0.251	4.167 ± 0.219	4.501 ± 2.166	2.053 ± 1.192	
			1600°C	0.193 ± 0.056	0.800 ± 0.157	0.190 ± 0.062	4.946 ± 0.108	1.846 ± 0.645	0.276 ± 0.1204	
		<b>Total</b>		<b>1.517 ± 0.165</b>	<b>12.382 ± 0.434</b>	<b>25.184 ± 2.049</b>	<b>63.610 ± 0.729</b>	<b>3.433 ± 0.284</b>	<b>4.084 ± 0.432</b>	
473	32.57	Crushing	#1	0.243 ± 0.037	1.486 ± 0.041	0.064 ± 0.019	0.735 ± 0.060	2.720 ± 0.424	0.074 ± 0.024	
			#3	0.236 ± 0.049	1.942 ± 0.102	0.067 ± 0.046	1.366 ± 0.155	3.655 ± 0.785	0.079 ± 0.056	
			#10	0.328 ± 0.050	1.873 ± 0.086	0.110 ± 0.021	2.768 ± 0.113	2.539 ± 0.401	0.094 ± 0.023	
			#20	0.414 ± 0.063	3.067 ± 0.258	0.125 ± 0.016	4.453 ± 0.099	3.290 ± 0.571	0.084 ± 0.017	
	10.66	Step Heating	600°C	1.581 ± 0.247	6.546 ± 0.154	0.554 ± 0.110	130.979 ± 1.520	1.840 ± 0.317	0.098 ± 0.025	
			800°C	1.800 ± 0.275	7.950 ± 0.208	1.531 ± 0.248	294.130 ± 2.705	1.962 ± 0.339	0.238 ± 0.053	
			1000°C	0.854 ± 0.145	5.530 ± 0.049	2.431 ± 0.405	132.301 ± 1.834	2.876 ± 0.494	0.795 ± 0.189	
			1200°C	1.334 ± 0.205	8.569 ± 0.182	1.285 ± 0.182	209.885 ± 2.019	2.855 ± 0.476	0.269 ± 0.056	
			1400°C	0.387 ± 0.104	4.203 ± 0.091	0.236 ± 0.044	12.671 ± 0.946	4.825 ± 1.334	0.171 ± 0.056	
			1600°C	0.675 ± 0.129	5.184 ± 0.052	0.586 ± 0.115	22.313 ± 0.638	3.141 ± 0.662	0.243 ± 0.064	
		<b>Total</b>		<b>7.897 ± 0.587</b>	<b>46.335 ± 0.632</b>	<b>6.988 ± 0.591</b>	<b>810.981 ± 4.992</b>	<b>2.687 ± 0.156</b>	<b>0.206 ± 0.019</b>	
480	46.16	Crushing	#1	nd	nd	nd	0.231 ± 0.074	nd	nd	
			#20	0.081 ± 0.019	0.571 ± 0.057	0.072 ± 0.015	2.043 ± 0.075	3.124 ± 0.779	0.249 ± 0.077	
	44.32	Step Heating	600°C	0.120 ± 0.026	0.797 ± 0.025	0.293 ± 0.155	17.848 ± 0.385	2.941 ± 0.652	0.680 ± 0.390	
			800°C	0.065 ± 0.014	0.466 ± 0.033	0.132 ± 0.025	44.097 ± 0.412	3.190 ± 0.714	0.571 ± 0.163	
			1000°C	0.027 ± 0.016	0.298 ± 0.020	0.073 ± 0.018	18.284 ± 0.217	4.846 ± 2.815	0.749 ± 0.468	
			1200°C	0.020 ± 0.014	0.188 ± 0.017	0.089 ± 0.018	5.790 ± 0.188	4.280 ± 3.039	1.276 ± 0.935	
			1400°C	nd	0.028 ± 0.026	0.002 ± 0.003	0.416 ± 0.132	nd	nd	
			1600°C	0.053 ± 0.034	0.134 ± 0.055	0.001 ± 0.005	0.847 ± 0.231	1.113 ± 0.842	0.003 ± 0.027	
			<b>Total</b>		<b>0.367 ± 0.068</b>	<b>2.482 ± 0.135</b>	<b>0.662 ± 0.175</b>	<b>89.555 ± 0.792</b>	<b>3.007 ± 0.450</b>	<b>0.502 ± 0.141</b>
	484	43.45	Step Heating	1200°C	8.373 ± 0.355	14.443 ± 0.321	0.540 ± 0.132	244.479 ± 0.446	0.766 ± 0.038	0.018 ± 0.004
1600°C				0.681 ± 0.453	1.698 ± 0.060	0.153 ± 0.032	17.639 ± 0.324	1.108 ± 0.738	0.063 ± 0.044	
		<b>Total</b>		<b>9.053 ± 0.575</b>	<b>16.142 ± 0.327</b>	<b>0.693 ± 0.135</b>	<b>262.116 ± 0.551</b>	<b>0.792 ± 0.053</b>	<b>0.021 ± 0.004</b>	
DRE1	74.2	Step Heating	1200°C	0.673 ± 0.204	1.523 ± 0.050	nd	4.811 ± 0.110	1.005 ± 0.306	nd	
			1600°C	nd	nd	nd	3.437 ± 0.094	nd	nd	
		<b>Total</b>		<b>0.673 ± 0.204</b>	<b>1.523 ± 0.050</b>	<b>nd</b>	<b>8.248 ± 0.145</b>	<b>1.005 ± 0.306</b>	<b>nd</b>	
DRE2	57.29	Step Heating	1200°C	0.508 ± 0.267	1.064 ± 0.084	nd	2.371 ± 0.046	0.930 ± 0.494	nd	
			1600°C	nd	nd	nd	0.924 ± 0.078	nd	nd	
		<b>Total</b>		<b>0.508 ± 0.267</b>	<b>1.064 ± 0.084</b>	<b>nd</b>	<b>3.295 ± 0.090</b>	<b>0.930 ± 0.494</b>	<b>nd</b>	
FG02	92.92	Step Heating	1200°C	2.047 ± 0.160	nd	nd	83.455 ± 0.162	nd	nd	
			1600°C	nd	0.854 ± 0.015	0.145 ± 0.029	5.593 ± 0.040	nd	nd	
		<b>Total</b>		<b>2.047 ± 0.160</b>	<b>0.854 ± 0.015</b>	<b>0.145 ± 0.029</b>	<b>89.048 ± 0.167</b>	<b>nd</b>	<b>nd</b>	
P20	35.56	Step Heating	1200°C	0.010 ± 0.304	23.752 ± 1.790	3.586 ± 1.038	85.837 ± 0.187	1036.866 ± 309.565	98.487 ± 2940.527	
			1600°C	0.640 ± 0.557	8.478 ± 0.466	3.559 ± 0.740	13.649 ± 0.234	5.889 ± 5.142	1.555 ± 1.393	
		<b>Total</b>		<b>0.650 ± 0.635</b>	<b>32.230 ± 1.849</b>	<b>7.145 ± 1.275</b>	<b>99.487 ± 0.300</b>	<b>22.037 ± 21.566</b>	<b>3.075 ± 3.052</b>	

nd = not determinable.

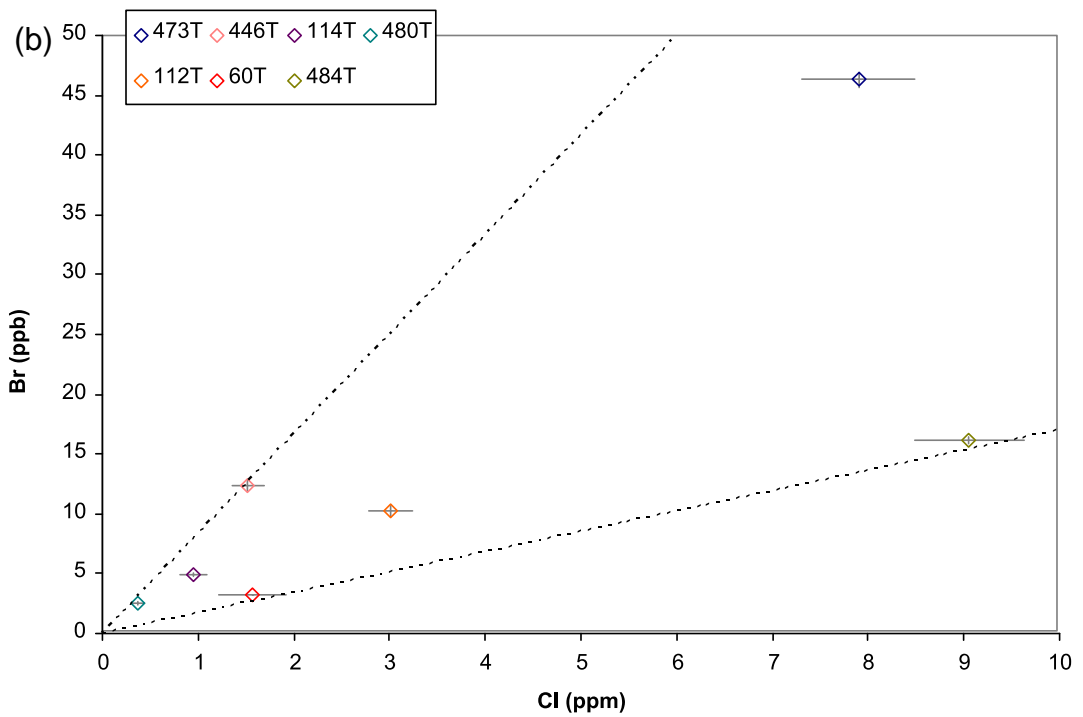
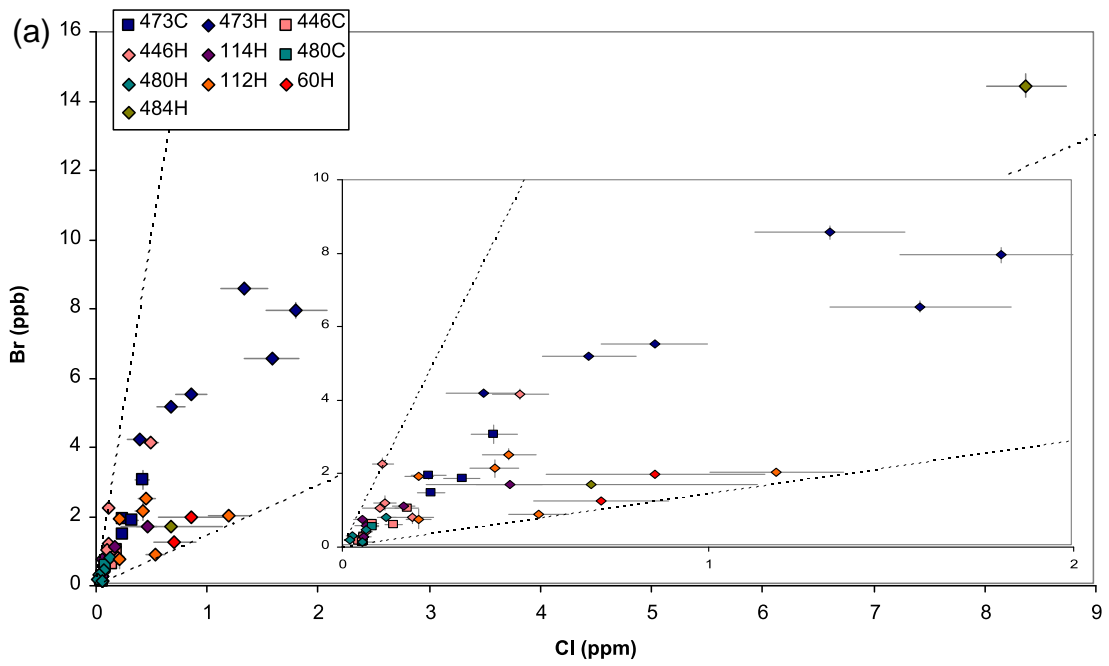


Figure 4.14 Br vs Cl for the Tristan and Inaccessible samples (squares = crushing; diamonds = heating; open symbols = total release). (a) Individual steps: all data have Br/Cl values between  $1.4 \times 10^{-3}$  and  $2.0 \times 10^{-2}$  shown by the dashed lines. (b) Total release: all data have Br/Cl values between  $1.7 \times 10^{-3}$  and  $8.3 \times 10^{-3}$ , shown by the dashed lines.

The I vs Cl plot shows that there is significant variation in I/Cl and greater variation in I concentrations with values ranging from 0.3-25 ppb for the total amount released (Figure 4.15). The majority of the values show I/Cl ratios in the range of  $10^{-3}$ - $10^{-4}$ , shown by the dashed lines (Figure 4.15).

Samples 446 (Inaccessible) and 473 (Inaccessible) show a higher total I concentration; this is likely to be partially due to the samples having a greater inclusion population density. However, sample 446 (Inaccessible) does not have a correspondingly high Cl concentration, perhaps suggesting a heterogeneous halogen composition in the mantle source. Samples 446 (Inaccessible) and 473 (Inaccessible) both have the highest I/Cl ratios as a result of their higher I concentrations.

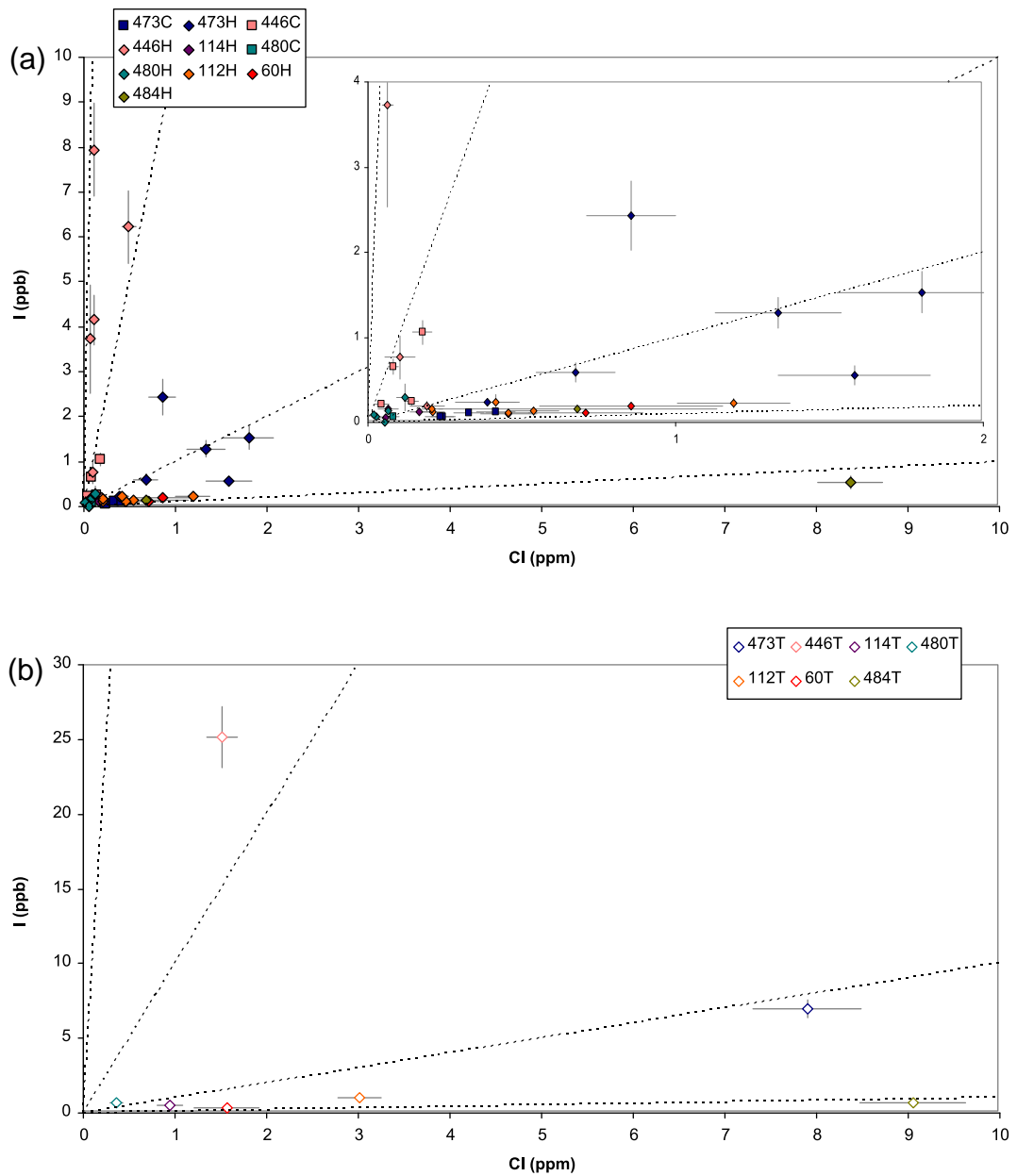
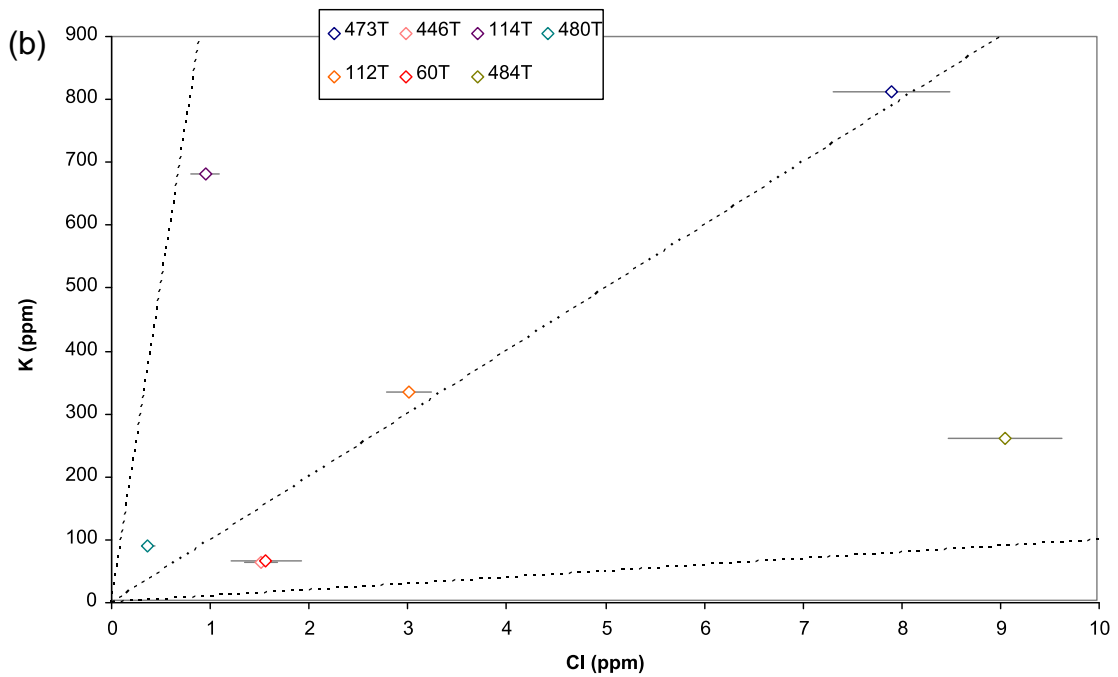
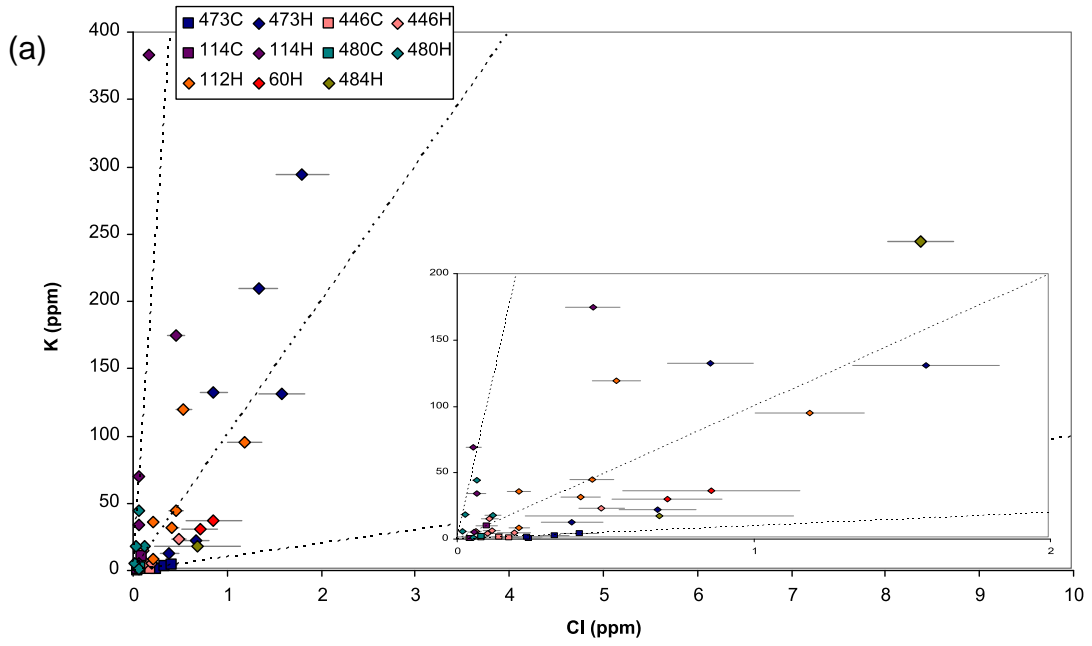


Figure 4.15 I vs CI for the Tristan and Inaccessible samples (squares = crushing; diamonds = heating; open symbols = total release). (a) Individual steps: the dashed lines show I/CI values of  $10^{-1}$ ,  $10^{-2}$ ,  $10^{-3}$  and  $10^{-4}$ . (b) Total releases: dashed lines show I/CI values of  $10^{-1}$ ,  $10^{-2}$ ,  $10^{-3}$  and  $10^{-4}$ .

Data show considerable variation in K and Cl (Figure 4.16). Concentrations for K range 19-811 ppm for the total gas release (Figure 4.16). Four of the samples (112 (Tristan), 114 (Tristan), 473 (Inaccessible), 484 (Tristan)) show a range of values for their individual release steps. Although the crushing steps show less K release, there is some overlap between the heating and crushing releases. K/Cl values for most samples fall between 10 and 1,000.

The release plots indicated that the K and Cl were released at different stages; this range of values suggests that the K and Cl have been fractionated from one another.



**Figure 4.16 K vs Cl for the Tristan and Inaccessible samples (squares = crushing; diamonds = heating; open symbols = total release). (a) Individual steps: The dashed lines show K/Cl values of  $10^{-3}$ . (b) Total K vs Cl. The dashed lines show K/Cl values of  $10^{-3}$ .**

### **4.2.3 Halogen and K Ratios**

A good correlation is observed on the Br/K vs Cl/K plot (Figure 4.17). Higher ratios of both Br/K and Cl/K are observed during crushing, particularly for samples 473 (Inaccessible) and 446 (Inaccessible) suggesting a variation in the source of the different inclusions.

The Br/K vs Cl/K plot for the total gas released shows that both Br/K and Cl/K show factor 1,000 variations (Br/K =  $3.5 \times 10^{-6}$  to  $1.0 \times 10^{-3}$ ; Cl/K  $4.8 \times 10^{-4}$  to  $36.4 \times 10^{-2}$ ). The crushing steps for samples 446 (Inaccessible) and 473 (Inaccessible) show the highest Br/K and Cl/K values; sample 484 (Tristan) has the highest Cl/K and sample 446 (Inaccessible) has the highest Br/K value.

Most of the total release values for Cl/K lie between the mid-ocean ridge basalt (MORB) and ocean island basalt (OIB) values of 0.01 and 0.042 determined from melt inclusions using ion probe measurements (Koleszar *et al.* 2009). This suggests that the variation in Br/K and Cl/K may result from mixing between these two end-members (Figure 4.17) although it is unknown if these components are trapped as separate melt inclusions or were mixed prior to trapping. Two of the samples, 114 (Tristan) and 480 (Inaccessible), show a lower Cl/K ratio than MORB ( $1.8 \times 10^{-3}$  and  $4.6 \times 10^{-3}$  respectively) and also have the lowest Br/K ratios ( $< 0.02 \times 10^{-3}$ ); this may be due to some heterogeneity in the MORB source. The lower temperature release has higher Cl/K, which may be due to release from hydrous inclusions.

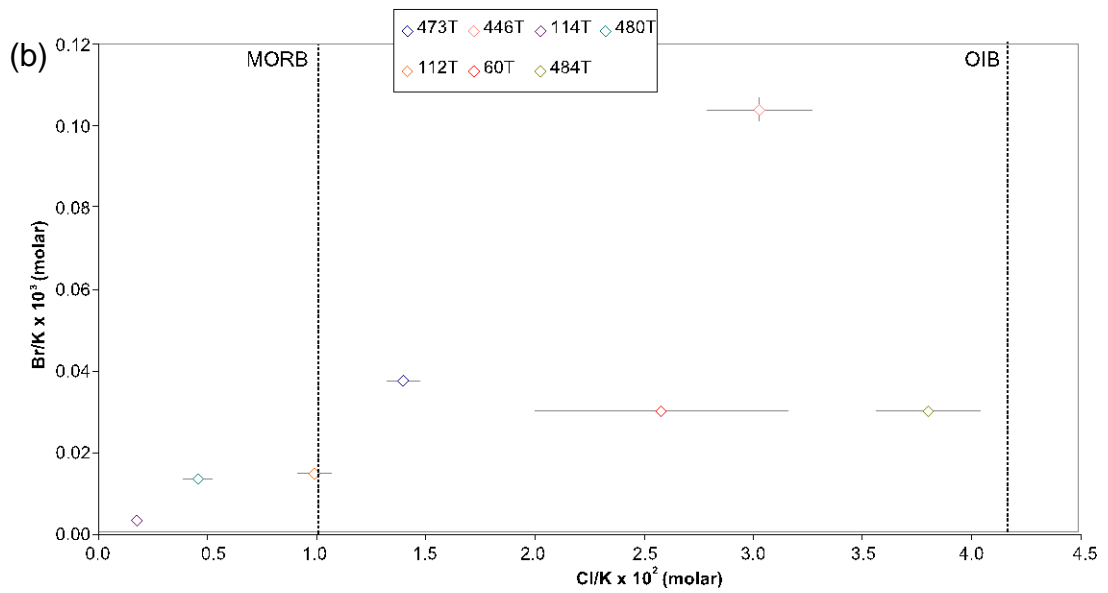
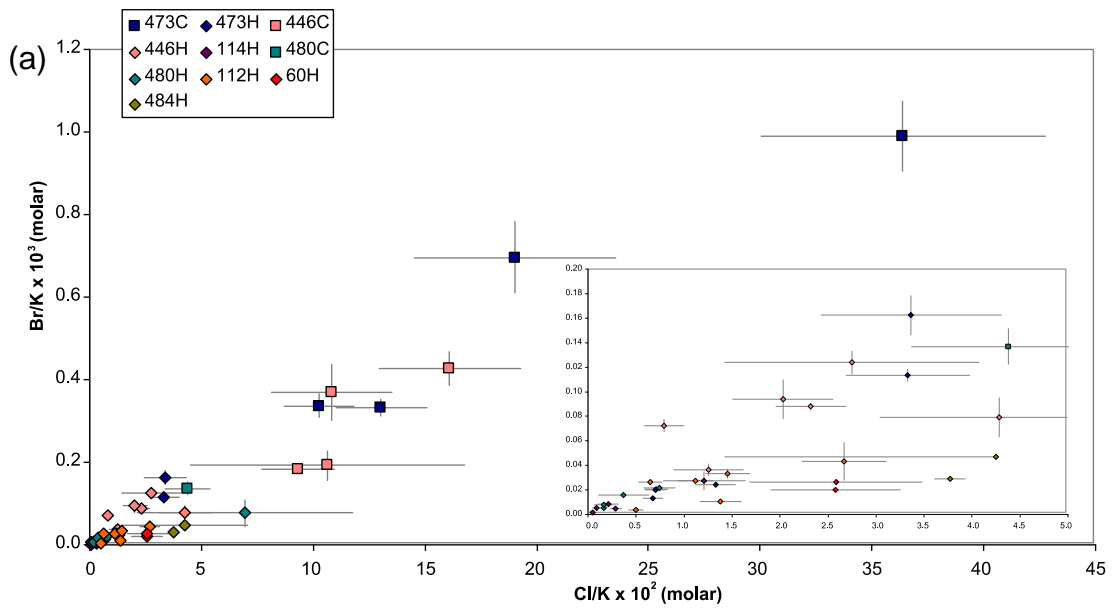


**Figure 4.17 Br/K vs Cl/K for the Tristan and Inaccessible samples (squares = crushing; diamonds = heating; open symbols = total release). (a) Individual steps. (b) Total releases: MORB and OIB are shown by the dashed lines (MORB and OIB data from Koleszar *et al.* 2009).**

Fitting a trend line to the data points on the Br/K vs Cl/K plot gives a possible mixing line between MORB and OIB (Figure 4.18). Using this line and Koleszar *et al.*'s (2009) Cl/K values for MORB and OIB, approximate values for Br/K for the two reservoirs can be estimated. This gives Br/K estimates of  $0.03 \times 10^{-3}$  for MORB and  $0.12 \times 10^{-3}$  for OIB.

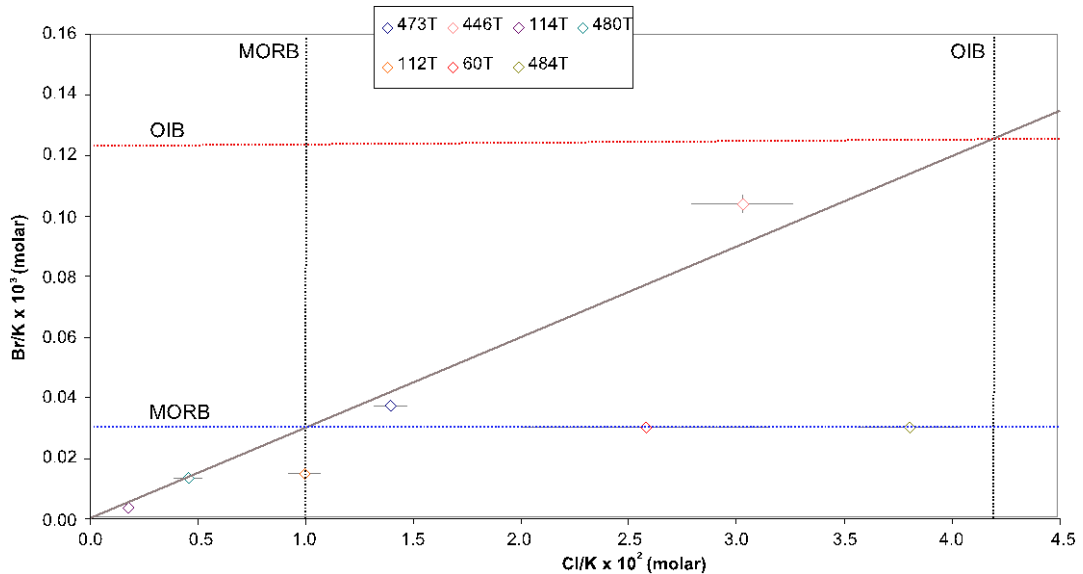


**Figure 4.18** Showing the derivation of MORB and OIB Br/K estimates (open symbols = total release) (MORB and OIB Cl/K data from Koleszar *et al.* 2009).

The plot of I/K vs Cl/K shows a greater variation than the Br/K plot, however there is an overall trend towards increasing I/K and Cl/K ratios with the crushing steps again recording the highest values (Figure 4.19).

The total I/K values extend from  $2.4 \times 10^{-7}$  to  $1.2 \times 10^{-4}$ , the highest value being observed in sample 446 (Inaccessible). Most of the values lie at around I/K of  $10^{-7}$ .

Samples 446 (Inaccessible) and 473 (Inaccessible) both have the highest I/K and Br/K ratios, but although both samples have high I and Br concentrations, only sample 473 (Inaccessible) has high K concentration.

This difference may again be due to the amount of inclusions present of different types, generations or source.

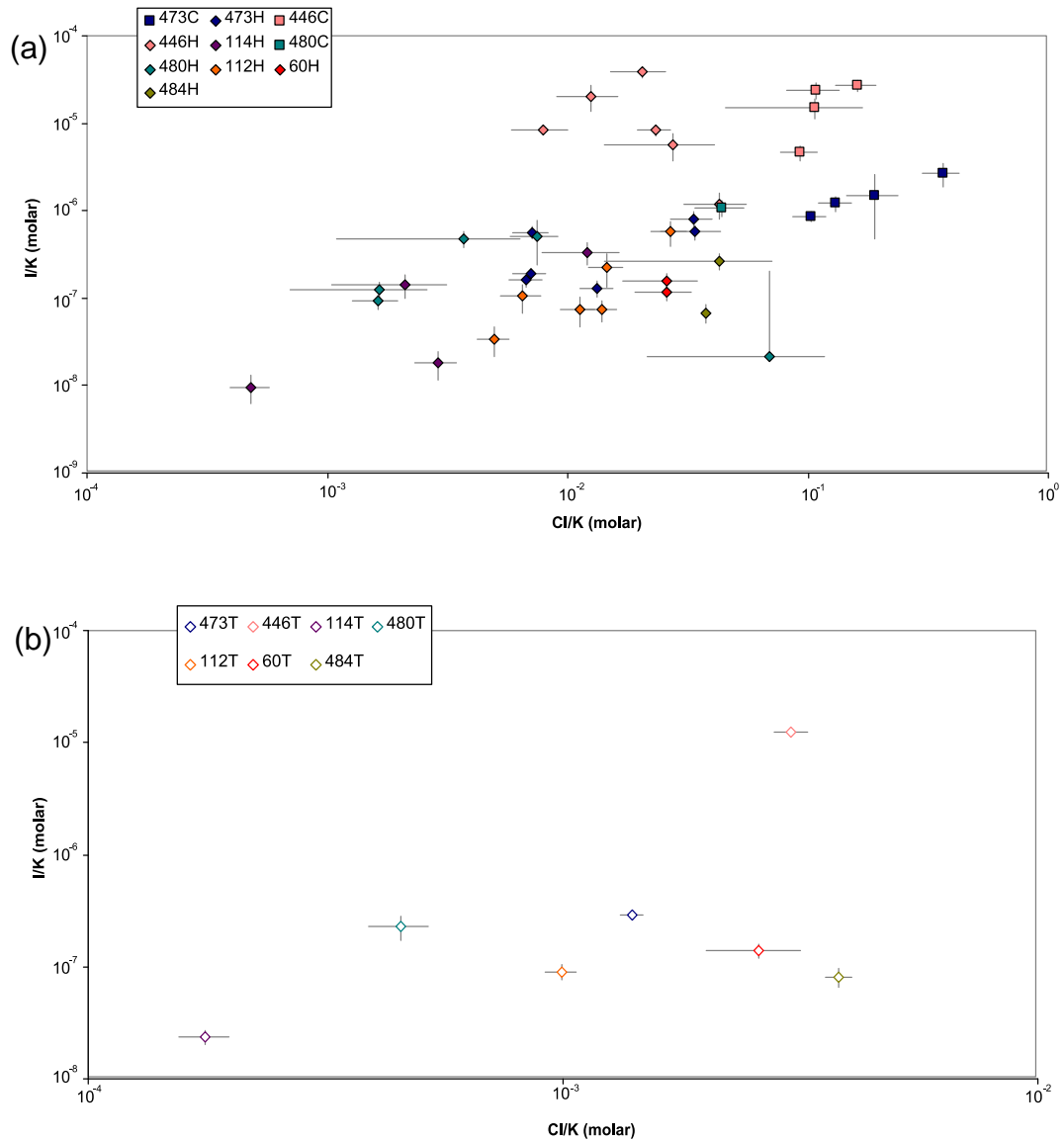


**Figure 4.19 I/K vs Cl/K for the Tristan and Inaccessible samples (squares = crushing; diamonds = heating; open symbols = total release). (a) Individual steps. (b) Total releases.**

#### 4.2.4 Halogen Ratios

For the halogen plot of I/Cl vs Br/Cl, the I/Cl values extend from  $3.0 \times 10^{-6}$  to  $1.9 \times 10^{-2}$  for the individual heating and crushing steps (Figure 4.20). The highest values are reported from the heating steps of sample 446 (Inaccessible); the range for this sample is from  $2.8 \times 10^{-4}$  to  $1.9 \times 10^{-2}$ , with an integrated value of  $4.1 \times 10^{-3}$ . Most of the I/Cl values fall between  $10^{-4}$  and  $10^{-2}$ . For the total releases, the values range from  $2.3 \times 10^{-6}$  to  $4.1 \times 10^{-3}$ , shown by the open symbols (Figure 4.20).

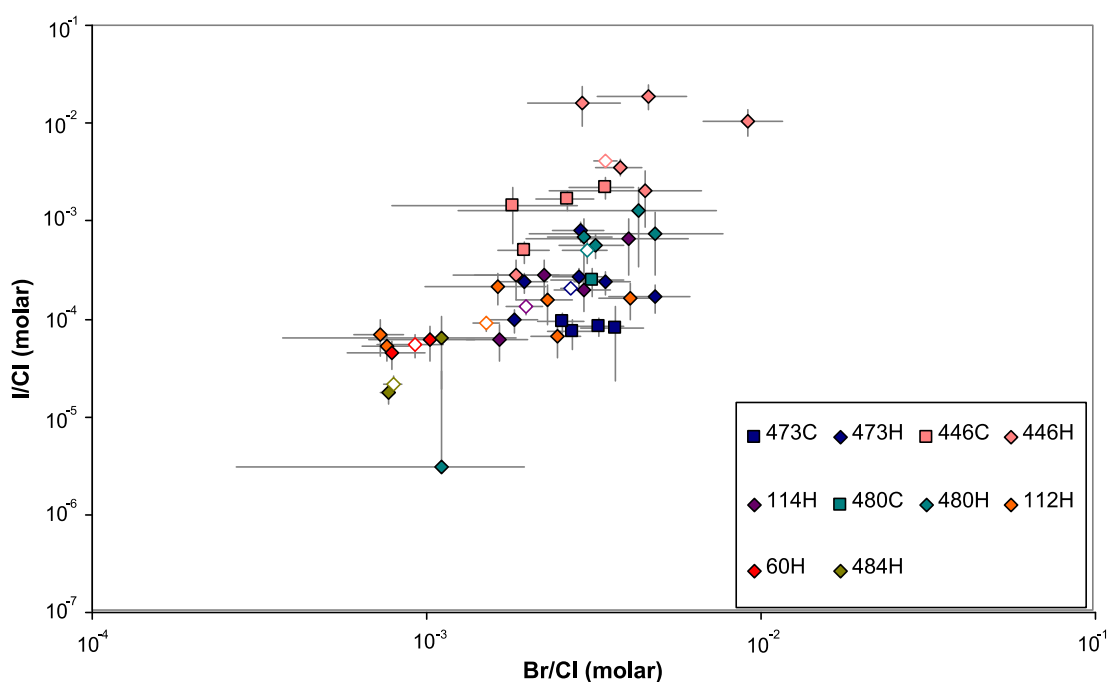


**Figure 4.20 I/Cl vs Br/Cl for the Tristan and Inaccessible samples (squares = crushing; diamonds = heating; open symbols = total release).**

There is less variation observed in the Br/Cl values, which range from  $(7.3-91) \times 10^{-4}$  for the individual steps, and from  $(7.9-34) \times 10^{-4}$  for the total releases. The largest range is again reported in sample 446 (Inaccessible), which extends from  $(1.8-9.1) \times 10^{-3}$ , with the larger values generally relating to the step heating releases.

There is overall variation within samples between low and high halogen ratios in Figure 4.21 (e.g. sample 446 (Inaccessible)). In Figure 4.21 it can be seen that the lower Br/Cl and I/Cl ratios almost extend to the MORB field, (Br/Cl  $(1.03\text{--}1.11) \times 10^{-3}$  and I/Cl  $(15\text{--}25) \times 10^{-6}$ ) (Schilling *et al.* 1980; Jambon *et al.* 1995; Burgess *et al.* 2009). The data has higher I/Cl than obtained from diamond analyses, which represent the sub-continental lithospheric mantle (SCLM) (Johnson *et al.* 2000; Burgess *et al.* 2002; Burgess *et al.* 2009). In particular the Tristan data do not correspond to the higher I/Cl and Br/Cl obtained from Canadian diamonds (Johnson *et al.* 2000). The high I/Cl of Canadian diamonds show fractionation of the halogens from one another, either due to separation of an immiscible fluid or due to crystallisation of the Cl-rich mineral phase, for example apatite (Johnson *et al.* 2000; Burgess *et al.* 2009). These processes do not appear to have played a role in the halogen composition of the Tristan source.

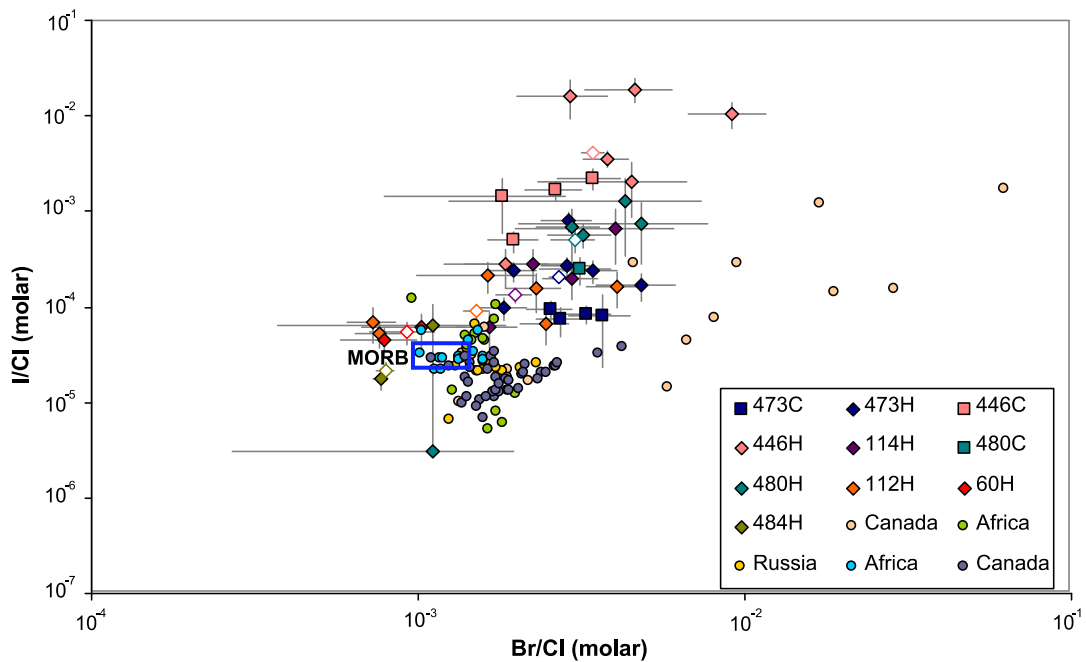


**Figure 4.21 I/Cl vs Br/Cl showing MORB field and diamond data added (squares = crushing; diamonds = heating; open symbols = total release. MORB values from (Schilling *et al.* 1980; Jambon *et al.* 1995; Burgess *et al.* 2009); diamond data from (Johnson *et al.* 2000; Burgess *et al.* 2002; Burgess *et al.* 2009)).**

Figure 4.22 shows the data with the estimated composition for the bulk silicate Earth (BE) added. The model BE value has been derived from halogen values determined on the basis of condensation temperatures by Allègre *et al.* (2001). Values of 10 ppm Cl, 400 ppb Br and 40.5 ppb I were calculated, giving Br/Cl  $17.7 \times 10^{-3}$  and I/Cl  $1.1 \times 10^{-3}$  (Allègre *et al.* 2001). This estimate does not fit the data from this study, as the data are trending towards higher I/Cl values for the calculated model BE Br/Cl value. BE values have also been estimated on the basis of halogen data from mantle samples (diamonds and MORB; (Burgess *et al.* 2002)), at Br/Cl =  $1.77 \times 10^{-3}$  and I/Cl =  $72 \times 10^{-6}$  (Figure 4.22). It is notable that this BE estimate is consistent with the minimum Br/Cl and I/Cl values obtained for the Tristan da Cunha analyses.

The chondritic (CI) value of  $1.64 \times 10^{-3}$  Br/Cl and  $470 \times 10^{-6}$  also has a Br/Cl close to the BE estimate (Figure 4.22), but the I/Cl is an order of magnitude higher (Johnson *et al.* 2000). However, halogen concentrations have only been measured in two CI chondrites, which showed widely differing values, and so there remains uncertainty regarding the CI value (Burgess *et al.* 2002). Due to the low condensation temperatures of the halogens, terrestrial halogens are expected to be more depleted than in CI chondrites. Some of the Tristan da Cunha samples show similar ratios to the estimated CI halogen ratios, but most of the samples show higher Br/Cl and I/Cl, particularly the samples from Inaccessible Island (samples 446, 473 and 480).

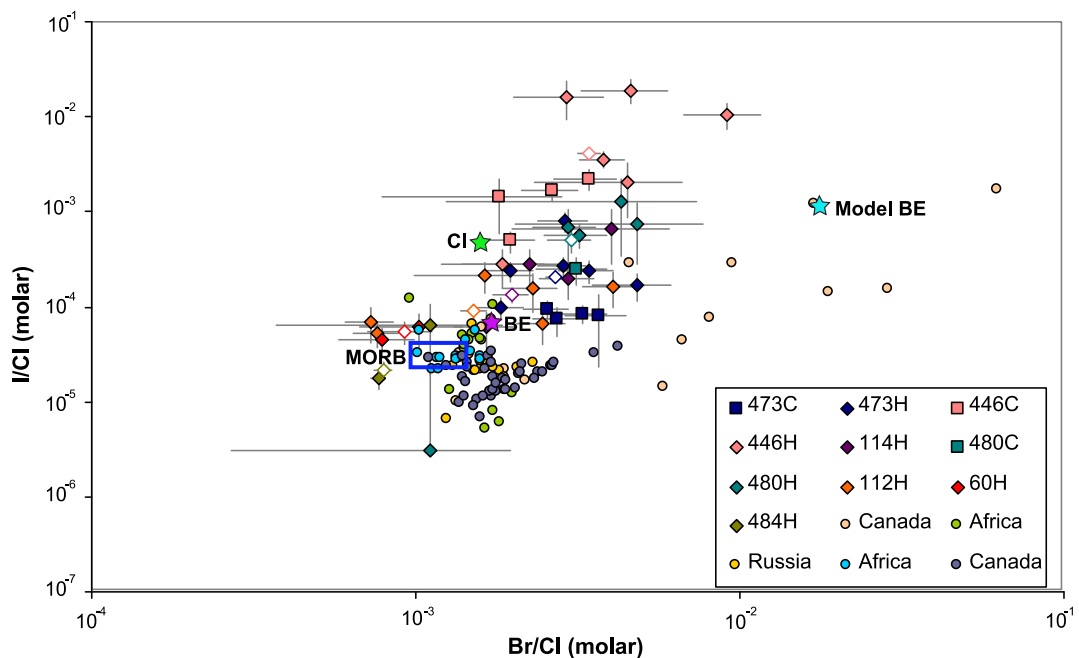


**Figure 4.22** I/Cl vs Br/Cl showing chondritic (CI), bulk Earth (BE) and model BE values (squares = crushing; diamonds = heating; open symbols = total release. MORB values from (Schilling *et al.* 1980; Jambon *et al.* 1995; Burgess *et al.* 2009); diamond data and CI and BE values from (Johnson *et al.* 2000; Burgess *et al.* 2002; Burgess *et al.* 2009); model BE data derived from (Allègre *et al.* 2001)).

The origin of the high Br/Cl and I/Cl component in Tristan da Cunha samples is more problematic. The only known source of material having high I/Cl and

Br/Cl in the Earth are organic-rich sediments and marine pore fluids. Marine pore fluids are highly enriched in I compared to seawater due to decay of organic-rich materials in the sediment pores which dramatically increases the I/Cl values by > 1,000 times the seawater value.

The high halogen ratios in Tristan da Cunha olivines may therefore be explained by the presence of subducted sediments in their mantle source. Support for this comes from the halogen composition of marine pore fluids (Figure 4.23) obtained from Mahn & Gieskes (2001) and Martin *et al.* (1993) which overlaps with data from the Tristan da Cunha samples for both the individual steps and the total releases. Only sample 60 (Tristan) lies significantly outside this field, having a more MORB/BE-like composition.

The majority of the samples have halogen composition between the MORB or BE end-member and the values reported for marine pore fluids. This range of values suggests that we are seeing a recycled halogen signature in OIBs from Tristan da Cunha, particularly within the Inaccessible Island samples, and indicates that subducted marine sediments and pore fluids are mixing with the OIB source. There may also be entrainment of MORB during magma ascent. The subduction origin of the halogen signature in Tristan da Cunha basalts is also supported by their radiogenic Pb isotope signature (Gibson *et al.* 2005).

Sample 446 (Inaccessible) has a higher I/Cl value than reported for marine pore fluids, however, Sumino *et al.* (2010) have suggested that an increase in I/Cl beyond the known range of marine pore fluids may be due to

additional release of I from dewatering of clay minerals and organic matter in the sediment pores.

Assuming a sediment I concentration of 15 ppm (Burgess *et al.* 2009), approximately 400 ppm sediment would need to be subducted to give the highest I/Cl ratio (sample 446 (Inaccessible) bulk) of  $4.1 \times 10^{-3}$  observed in the Tristan da Cunha samples. The I concentrations in the marine pore fluids are variable and can reach 145 ppm (Martin *et al.* 1993), so this sediment concentration could be lower by up to an order of magnitude.

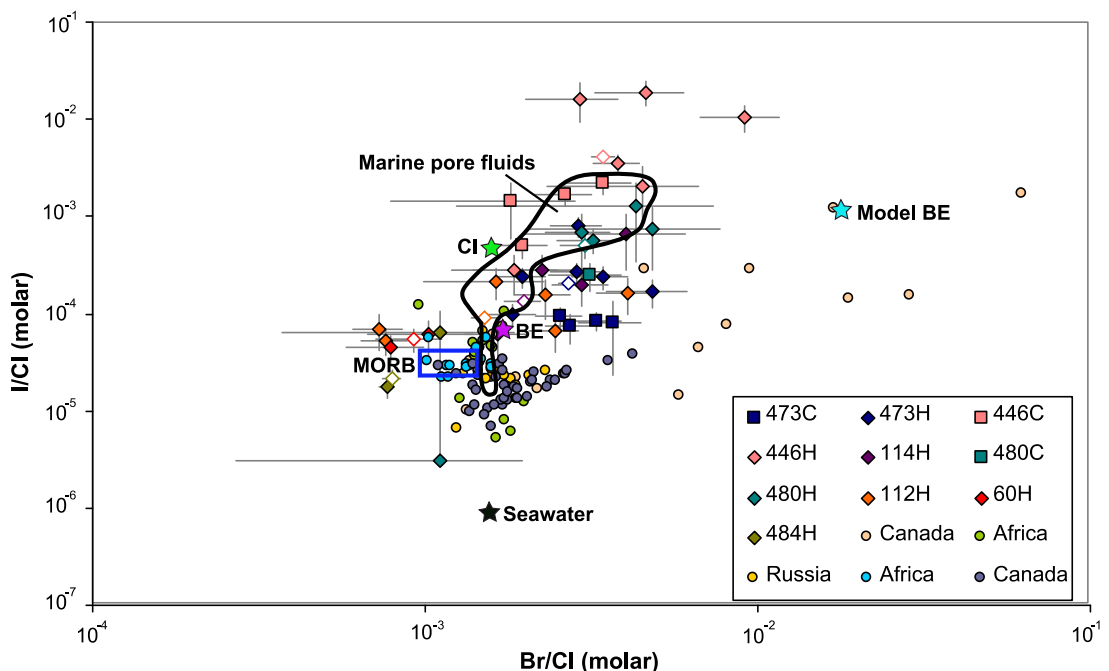


**Figure 4.23** I/Cl vs Br/Cl showing marine pore fluid field and seawater ratio (squares = crushing; diamonds = heating; open symbols = total release. Marine pore fluid data from (Martin *et al.* 1993; Mahn & Gieskes 2001; Sumino *et al.* 2010); MORB values from (Schilling *et al.* 1980; Jambon *et al.* 1995; Burgess *et al.* 2009); diamond, BE, CI and seawater data from (Johnson *et al.* 2000; Burgess *et al.* 2002; Burgess *et al.* 2009); model BE data derived from (Allègre *et al.* 2001)).

### 4.3 Mantle Source Halogen Concentrations

Due to the volatility of the halogens, we can assume that during partial melting of the lower mantle that all of the Cl, Br and I present will partition into the melt. OIB are believed to be form by approximately 10% partial

melting of their mantle source. As such, the OIB halogen concentrations measured can be used as a proxy for the Tristan hotspot mantle source.

Most of the samples analysed optically have an estimated fluid/melt inclusion abundance of approximately 1-5%vol. Thus, from this estimate and the concentration of halogens released from the bulk olivine sample it is possible to estimate of the halogen concentrations of the mantle source.

The maximum concentrations measured for Tristan da Cunha bulk olivine are 9 ppm Cl, 46 ppb Br and 25 ppb I. These concentrations constrain the maximum concentrations for the Tristan OIBs as 180-900 ppm Cl, 0.9-4.6 ppm Br and 0.5-2.5 ppm I; assuming a maximum partial melting figure of 10%, this gives 90 ppm Cl, 0.4 ppm Br and 0.25 ppm I for the enriched mantle source. These figures are in good agreement with previously published figures of 70 ppm Cl and 0.27 ppm Br for Iceland and Hawaii subaerial volcanism (Schilling *et al.* 1978).

Compared to MORB values of 35 ppm Cl, 0.1 ppm Br and 0.001 ppm I, these data show an enrichment of 2.6 for Cl and 4.6 for Br and a factor of 250 for I, suggesting that the mantle source is enriched in the order of Cl < Br < I.

Using these values, the Br/Cl and I/Cl ratios of the mantle source are calculated as  $2.3 \times 10^{-3}$  and  $776 \times 10^{-6}$  respectively.

There are uncertainties associated with using this method to estimate OIB and mantle source concentrations, as we are estimating the degree of partial melting of the source and the proportion of melt inclusions. The accuracy of the estimations could be increased with electron microprobe data on the

individual inclusions for each sample, enabling the Cl and K concentrations (and hence Br and I) to be measured directly.

#### **4.4 Noble Gases**

##### **4.4.1 Argon**

In addition to halogens, Ar isotope ratios are also obtained during crushing and stepped heating (Table 4.2). The  $^{40}\text{Ar}/^{36}\text{Ar}$  ratios measured for the individual steps mostly fall in the range of 296-500 with most similar to the atmospheric argon value with  $^{40}\text{Ar}/^{36}\text{Ar} = 295.5$  (Figure 4.24). There is no correlation between  $^{40}\text{Ar}/^{36}\text{Ar}$  and  $\text{Cl}/^{36}\text{Ar}$ ; as has been observed previously in mantle samples (Johnson *et al.* 2000) with the  $^{40}\text{Ar}/^{36}\text{Ar}$  values being relatively constant over a large range of  $\text{Cl}/^{36}\text{Ar}$  values ( $< 3,000,000$ ). The relatively young age of the samples ( $< 1$  Ma Tristan;  $< 6$  Ma Inaccessible) means that in situ addition of radiogenic  $^{40}\text{Ar}$  from  $^{40}\text{K}$  decay is assumed to be a minor component. For sample 112 (Tristan), a few heating steps gave  $^{40}\text{Ar}/^{36}\text{Ar}$  values of 200-250, lower than the value of air; the reasons for this are unknown but possibilities include the presence of isotopically fractionated Ar within the sample, or an analytical artefact.

For each sample, the total gas released gives  $^{40}\text{Ar}/^{36}\text{Ar}$  ratios which are often within error of air, 295.5, ranging from 272-297. Data obtained by Dr David Murphy (pers. comm.) by *in vacuo* crushing of the same set of unirradiated samples also show a low  $^{40}\text{Ar}/^{36}\text{Ar}$  values, with a maximum of 743 (Table 4.2).

The low  $^{40}\text{Ar}/^{36}\text{Ar}$  values are consistent with a marine pore fluid component containing dissolved atmospheric Ar being recycled in to the Tristan mantle

source region. All of the values reported are much less than the typical OIB  $^{40}\text{Ar}/^{36}\text{Ar}$  values of 3,000-12,000.

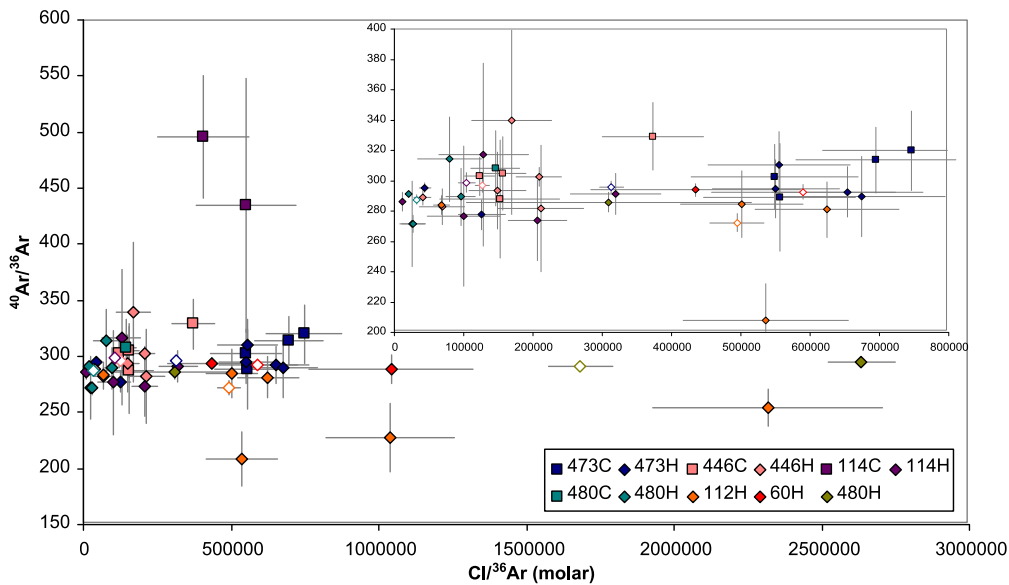


**Figure 4.24** Showing the range of Ar values; most are within error of air (295.5) (squares = crushing; diamonds = heating; open symbols = total release).

#### 4.4.2 Helium

The  $^3\text{He}/^4\text{He}$  values were obtained by Dr Murphy by *in vacuo* crushing of unirradiated aliquots of the Tristan olivine samples. The  $^3\text{He}/^4\text{He}$  values range between 2-6  $R_A$  (Table 4.2) and are all below the OIB mantle values of  $< 38 R_A$ , and the MORB value of 8  $R_A$  (Pepin & Porcelli 2002). Atmospheric He has a low  $^3\text{He}/^4\text{He}$  value of 1  $R_A$ , however the He concentration of air is very low and recycling of dissolved air in marine pore fluids is not considered to be a significant source of He. Reduction in the  $^3\text{He}/^4\text{He}$  in the Tristan source can be accounted for by the presence of a subducted sediment component. As sediment is U-rich and  $^4\text{He}$  is formed from during the decay of  $^{238}\text{U}$  and  $^{235}\text{U}$ , any addition of sediment to the OIB source will decrease the  $^3\text{He}/^4\text{He}$  ratio and this could explain the lower  $R_A$  values observed in the Tristan da Cunha samples (Pepin & Porcelli 2002).

Table 4.2 He and Ar data from previous study (Ol = olivine, Px = pyroxene) (provided by Dr David Murphy, except <sup>a</sup> from this study).

Sample (BM 1962 / 128)	Phase	R/Ra	<sup>40</sup> Ar/ <sup>36</sup> Ar	<sup>40</sup> Ar/ <sup>36</sup> Ar <sup>a</sup>
60	Ol	2.0 ± 8.8	361 ± 274	293 ± 5
60	Px	3.3 ± 4.1	357 ± 19	-
112	Ol	5.1 ± 0.9	743 ± 36	272 ± 6
112	Px	5.4 ± 1.0	387 ± 38	-
114	Ol	3.3 ± 1.7	378 ± 16	299 ± 6
114	Px	4.9 ± 1.3	381 ± 24	-
114	Px	5.0 ± 0.3	-	-
341	Ol	4.9 ± 1.3	312 ± 13	-
341	Px	3.9 ± 3.1	348 ± 17	-
446	Ol	2.1 ± 2.4	315 ± 11	297 ± 4
446	Px	6.2 ± 1.0	377 ± 29	-
473	Ol	5.8 ± 0.6	533 ± 21	296 ± 4
473	Px	5.1 ± 0.8	401 ± 15	-
473	Px	5.6 ± 0.3	-	-
480	Ol	5.9 ± 2.5	313 ± 3	288 ± 3
480	Px	5.4 ± 2.3	337 ± 4	-
482	Ol	5.7 ± 1.3	328 ± 17	-
482	Px	2.5 ± 3.6	334 ± 5	-
484	Ol	5.7 ± 2.0	413 ± 43	291 ± 3
484	Px	3.9 ± 4.2	378 ± 54	-

#### 4.5 Réunion and Fogo

For the four remaining samples, the majority of the data for the total releases falls within the ranges observed in the Tristan da Cunha samples.

In the Réunion samples, Br/Cl extended from  $(9.3-10) \times 10^{-4}$ , within the  $(7.9-34) \times 10^{-4}$  seen in the Tristan da Cunha samples. Br/Cl was only measured within one Fogo sample; this was a magnitude higher than the Tristan range at  $2.2 \times 10^{-2}$ .

In the Fogo samples, the only measurement obtained for I/Cl was  $3.1 \times 10^{-3}$ , which is within the range of  $2.3 \times 10^{-6}$  to  $4.1 \times 10^{-3}$  observed in the Tristan da Cunha samples. No data was obtained for I/Cl from the Réunion samples.

All the Fogo and Réunion samples for Cl/K and Br/K fell within the range of the Tristan results, extending from  $7.2 \times 10^{-3}$  to  $2.4 \times 10^{-1}$  Cl/K and  $4.7 \times 10^{-6}$  to  $1.6 \times 10^{-4}$  Br/K. Data was only obtained for I/K for the Fogo samples; again this were within range of the Tristan data, extending from  $5.0 \times 10^{-7}$  to  $2.2 \times 10^{-5}$ .

$^{40}\text{Ar}/^{36}\text{Ar}$  data were also low for the Fogo and Réunion samples, all being low and close to air in composition, extending from 288-812. He data for one of the Fogo samples gives a low  $R_A$  of 4.9, similar to the Tristan and Inaccessible samples.

The similarities between the Fogo and Réunion samples, and the Tristan da Cunha samples indicate the possibility of sediment or pore fluid recycling and a subducted halogen signature within these samples, as well as the Tristan and Inaccessible samples.

#### **4.6 Implications for Mantle Halogen Geochemistry**

The presence of a subducted halogen signature within the Tristan da Cunha OIBs, together with low  $^{40}\text{Ar}/^{36}\text{Ar}$  and a depressed  $R_A$  value, suggests that I-rich sediment, or marine pore fluid, is being transported via subduction down to the hotspot source – potentially the core-mantle boundary. Recent work suggests that both sediments and fluids containing Cl and Br undergo shallow recycling to the depths of arc volcanism, and possibly beyond the transition zone (Straub & Layne 2003; Bureau *et al.* 2010). Due to the similar chemical behaviour of I, we would expect that deep recycling of all the heavy halogens may occur.

The low  $R_A$  of the Tristan basalts is not typical for hotspot volcanism, so the Tristan hotspot may be geochemically distinct from other hotspots. As such, it is not expected that all hotspots will exhibit a recycled halogen signature, although similar results are shown in the Réunion and Fogo samples.

#### **4.7 Implications for the Source of the Tristan Mantle Plume**

The difference in the halogen signature between the Tristan and the Inaccessible OIBs suggests that the composition of the mantle source has changed over the past 6 Ma. This confirms previous results which suggest that the chemical and isotopic composition of the enriched mantle source has evolved both temporally and spatially (Le Roex *et al.* 1990; Gibson *et al.* 2005). However, the subducted sediment signature that is present in the basalts from this study agrees with earlier findings on Pb isotopes by Gibson *et al.* (2005) which suggest a subduction origin for the Tristan da Cunha basalts.

The Inaccessible basalts had both a higher I/Cl ratio and were more vesicular than the Tristan samples, suggesting that the more gaseous earlier eruptions were I-rich. It would be interesting to analyse some of the earlier Tristan central cone eruptions, which were also more gaseous, to see if a similar halogen signature is present.

## 5 Conclusions

- 1) The Tristan da Cunha samples show a strong overlap of I/Cl and Br/Cl values with marine pore fluids, suggesting that subducted sediments are mixing with the mantle source for the Tristan hotspot. The samples with lower I/Cl and Br/Cl lie close to the BE and MORB fields, suggesting a mixing trend between BE or MORB, and I-rich sediments.
- 2) The Tristan hotspot source has changed chemically over time; the Inaccessible basalts report higher halogen ratios than seen in the Tristan samples. The highest Inaccessible I/Cl is  $4.1 \times 10^{-3}$ , the highest Tristan I/Cl is  $1.3 \times 10^{-4}$ ; the highest Br/Cl are  $3.4 \times 10^{-3}$  and  $2.0 \times 10^{-3}$  for Inaccessible and Tristan respectively.
- 3) The maximum concentrations calculated for the Tristan hotspot source are 90 ppm Cl, 0.46 ppm Br and 0.25 ppm I, in good agreement with previously published data for other ocean islands. These values give Br/Cl  $2.3 \times 10^{-3}$  and I/Cl  $776 \times 10^{-6}$  for the enriched mantle source.
- 4) Approximately 400 ppm of sediment with 15 ppm I would need to be subducted in order to obtain the values observed in the Tristan da Cunha basalts.
- 5) The Cl/K values observed extend from  $4.8 \times 10^{-4}$  to  $36.4 \times 10^{-2}$  and show a trend of mixing between MORB and OIB. Some values reported are lower than MORB; this may indicate heterogeneity in the MORB component. Br/K values range from  $3.5 \times 10^{-6}$  to  $1.0 \times 10^{-3}$ ;

values for MORB and OIB end-members have been derived at  $0.03 \times 10^{-3}$  and  $0.12 \times 10^{-3}$  respectively. I/K extends from  $2.4 \times 10^{-7}$  to  $1.2 \times 10^{-4}$ .

- 6) The low  $R_A$  of the Tristan da Cunha samples suggests that U-rich sediment is being recycled into the mantle source. However the  $R_A$  of OIBs ranges to  $< 38$ , indicating that the mantle source of the Tristan hotspot is not typical of all ocean islands. The  $^{40}\text{Ar}/^{36}\text{Ar}$  is similar to air, suggesting that noble gases are also being recycled.

### **5.1 Ideas for Further Work**

In order to improve the estimates of the halogen concentrations for OIB, microprobe analysis could be carried out in order to establish the Cl and K concentrations within the inclusions, rather than just in the bulk sample. Point counting could also be used to establish the inclusion density, allowing the concentrations to be calculated optically. Both these methods would allow a better constraint to be put on the OIB concentrations of K, Cl, Br and I and thus the halogen concentrations of the mantle source.

Analyses could be completed on OIBs from different island groups, to see if Tristan da Cunha is representative of ocean islands, by seeing if a similar subducted halogen signature is present. A comparative study of halogens in high  $R_A$  and low  $R_A$  OIBs would help to confirm if the low  $R_A$  observed at Tristan da Cunha is purely as a result of sediment recycling.

It would also be interesting to date the Tristan da Cunha group samples in order to establish how the halogen signature of the plume has changed

temporally, as the Tristan basalts differ to the Inaccessible basalts. Further samples from Nightingale Island and Gough Island could also be analysed to see how the halogen signature has changed over time.

For ocean islands which have a related flood basalt province, it would be of interest to establish how the halogen signatures have changed during the evolution of the mantle plume. Analyses of the three Tristan group islands, together with Gough Island, may help elucidate the chemical and isotopic evolution of the Tristan hotspot.

## **Acknowledgements**

Firstly, I would like to thank my supervisor Dr Ray Burgess for his endless patience and support over the past year. I would also like to thank the Natural History Museum, London for providing access to the samples, and Dr David Murphy for supplying additional thin sections and noble gas data.

Many thanks to James Jepson for his moral support, helping me to learn various graphics packages and for generally keeping me sane!

And finally, thanks to my mum, Liz Abbott for introducing me to the world of geology and encouraging me to return to university, for her support over the past four years, and most recently, for keeping my house clean and me fed whilst I was writing up!

## References

- Aiuppa, A., Baker, D. R. & Webster, J. D. 2008. Halogens in volcanic systems. *Chemical Geology*, **263**(1-4), 1-18.
- Allègre, C., Manhès, G. & Lewin, É. 2001. Chemical composition of the Earth and the volatility control on planetary genetics. *Earth and Planetary Science Letters*, **185**(1-2), 49-69.
- Baker, P. E., Gass, I. G., Harris, P. G. & Maitre, R. W. L. 1964. The Volcanological Report of the Royal Society Expedition to Tristan da Cunha, 1962. *Philosophical Transactions of the Royal Society of London. Series A, Mathematical and Physical Sciences*, **256**(1075), 439-575.
- Ballentine, C. J., Burgess, R. & Marty, B. 2002. Tracing Fluid Origin, Transport and Interaction in the Crust. *Reviews in Mineralogy and Geochemistry*, **47**(1), 539-614.
- Bureau, H., Foy, E., Raepsaet, C., Somogyi, A., Munsch, P., Simon, G. & Kubsy, S. 2010. Bromine cycle in subduction zones through in situ Br monitoring in diamond anvil cells. *Geochimica et Cosmochimica Acta*, **In Press, Accepted Manuscript**.
- Burgess, R., Layzelle, E., Turner, G. & Harris, J. W. 2002. Constraints on the age and halogen composition of mantle fluids in Siberian coated diamonds. *Earth and Planetary Science Letters*, **197**(3-4), 193-203.
- Burgess, R., Cartigny, P., Harrison, D., Hobson, E. & Harris, J. 2009. Volatile composition of microinclusions in diamonds from the Panda kimberlite, Canada: Implications for chemical and isotopic heterogeneity in the mantle. *Geochimica et Cosmochimica Acta*, **73**(6), 1779-1794.

- Campbell, I. H. 2007. Testing the plume theory. *Chemical Geology*, **241**(3-4), 153-176.
- Carlson, R. W. 1995. Isotopic inferences on the chemical structure of the mantle. *Journal of Geodynamics*, **20**(4), 365-386.
- Chevallier, L. & Verwoerd, W. J. 1987. A dynamic interpretation of Tristan da Cunha volcano, South Atlantic Ocean. *Journal of Volcanology and Geothermal Research*, **34**(1-2), 35-49.
- Cliff, R. A., Baker, P. E. & Mateer, N. J. 1991. Geochemistry of inaccessible island volcanics. *Chemical Geology*, **92**(4), 251-260.
- Davies, G. F. 1990. Mantle plumes, mantle stirring and hotspot chemistry. *Earth and Planetary Science Letters*, **99**(1-2), 94-109.
- Déruelle, B., Dreibus, G. & Jambon, A. 1992. Iodine abundances in oceanic basalts: implications for Earth dynamics. *Earth and Planetary Science Letters*, **108**(4), 217-227.
- Ernesto, M., Marques, L. S., Piccirillo, E. M., Molina, E. C., Ussami, N., Comin-Chiaramonti, P. & Bellieni, G. 2002. Paraná Magmatic Province-Tristan da Cunha plume system: fixed versus mobile plume, petrogenetic considerations and alternative heat sources. *Journal of Volcanology and Geothermal Research*, **118**(1-2), 15-36.
- Farnetani, C. G., Legras, B. & Tackley, P. J. 2002. Mixing and deformations in mantle plumes. *Earth and Planetary Science Letters*, **196**(1-2), 1-15.
- Gass, I. G. 1967. Geochronology of the Tristan da Cunha Group of Islands. *Geological Magazine*, **104**(2), 160-170.
- Gibson, S. A., Thompson, R. N., Day, J. A., Humphris, S. E. & Dickin, A. P. 2005. Melt-generation processes associated with the Tristan mantle

- plume: Constraints on the origin of EM-1. *Earth and Planetary Science Letters*, **237**(3-4), 744-767.
- Graham, D. W. 2002. Noble Gas Isotope Geochemistry of Mid-Ocean Ridge and Ocean Island Basalts: Characterization of Mantle Source Reservoirs. *Reviews in Mineralogy and Geochemistry*, **47**(1), 247-317.
- Harris, C., Smith, H. S. & le Roex, A. P. 2000. Oxygen isotope composition of phenocrysts from Tristan da Cunha and Gough Island lavas: variation with fractional crystallization and evidence for assimilation. *Contributions to Mineralogy and Petrology*, **138**(2), 164-175.
- Jambon, A., Déruelle, B., Dreibus, G. & Pineau, F. 1995. Chlorine and bromine abundance in MORB: the contrasting behaviour of the Mid-Atlantic Ridge and East Pacific Rise and implications for chlorine geodynamic cycle. *Chemical Geology*, **126**(2), 101-117.
- Johnson, L. H., Burgess, R., Turner, G., Milledge, H. J. & Harris, J. W. 2000. Noble gas and halogen geochemistry of mantle fluids: comparison of African and Canadian diamonds. *Geochimica et Cosmochimica Acta*, **64**(4), 717-732.
- Kendrick, M. A. 2000. *Noble gases and halogens in fluid inclusions: definitive evidence on the age and origin of ancient mineralising fluids*. PhD Thesis, University of Manchester, 250 pp.
- Koleszar, A. M., Saal, A. E., Hauri, E. H., Nagle, A. N., Liang, Y. & Kurz, M. D. 2009. The volatile contents of the Galapagos plume; evidence for H<sub>2</sub>O and F open system behavior in melt inclusions. *Earth and Planetary Science Letters*, **287**(3-4), 442-452.

- Le Roex, A. P., Cliff, R. A. & Adair, B. J. I. 1990. Tristan da Cunha, South Atlantic: Geochemistry and Petrogenesis of a Basanite-Phonolite Lava Series. *J. Petrology*, **31**(4), 779-812.
- Mahn, C. L. & Gieskes, J. M. 2001. Halide systematics in comparison with nutrient distributions in sites 1033B and 1034B, Saanich Inlet: ODP Leg 169S. *Marine Geology*, **174**(1-4), 323-339.
- Martin, J. B., Gieskes, J. M., Torres, M. & Kastner, M. 1993. Bromine and iodine in Peru margin sediments and pore fluids: Implications for fluid origins. *Geochimica et Cosmochimica Acta*, **57**(18), 4377-4389.
- McDougall, I. & Ollier, C. D. 1982. Potassium-argon ages from Tristan da Cunha, South Atlantic. *Geological Magazine*, **119**(1), 87-93.
- Pepin, R. O. & Porcelli, D. 2002. Origin of Noble Gases in the Terrestrial Planets. *Reviews in Mineralogy and Geochemistry*, **47**(1), 191-246.
- Porcelli, D., Ballentine, C. J. & Wieler, R. 2002. An Overview of Noble Gas Geochemistry and Cosmochemistry. *Reviews in Mineralogy and Geochemistry*, **47**(1), 1-19.
- Pyle, D. M. & Mather, T. A. 2009. Halogens in igneous processes and their fluxes to the atmosphere and oceans from volcanic activity: A review. *Chemical Geology*, **263**(1-4), 110-121.
- Richards, M. A., Duncan, R. A. & Courtillot, V. E. 1989. Flood Basalts and Hot-Spot Tracks: Plume Heads and Tails. *Science*, **246**(4926), 103-107.
- Safonov, O. G., Perchuk, L. L. & Litvin, Y. A. 2007. Melting relations in the chloride-carbonate-silicate systems at high-pressure and the model for

- formation of alkalic diamond-forming liquids in the upper mantle. *Earth and Planetary Science Letters*, **253**(1-2), 112-128.
- Schilling, J. G., Unni, C. K. & Bender, M. L. 1978. Origin of chlorine and bromine in the oceans. *Nature*, **273**(5664), 631-636.
- Schilling, J. G., Bergeron, M. B., Evans, R. & Smith, J. V. 1980. Halogens in the Mantle Beneath the North Atlantic [and Discussion]. *Philosophical Transactions of the Royal Society of London. Series A, Mathematical and Physical Sciences*, **297**(1431), 147-178.
- Straub, S. M. & Layne, G. D. 2003. The systematics of chlorine, fluorine, and water in Izu arc front volcanic rocks: Implications for volatile recycling in subduction zones. *Geochimica et Cosmochimica Acta*, **67**(21), 4179-4203.
- Sumino, H., Burgess, R., Mizukami, T., Wallis, S. R., Holland, G. & Ballentine, C. J. 2010. Seawater-derived noble gases and halogens preserved in exhumed mantle wedge peridotite. *Earth and Planetary Science Letters*, **294**(1-2), 163-172.
- The Tristan da Cunha Website 2009. <http://www.tristandc.com/index.php>. Accessed 15/12/09.
- Wilson, M. 1993. Geochemical signatures of oceanic and continental basalts: a key to mantle dynamics? *Journal of the Geological Society*, **150**(5), 977-990.
- Wolfe, C. J., Solomon, S. C., Laske, G., Collins, J. A., Detrick, R. S., Orcutt, J. A., Bercovici, D. & Hauri, E. H. 2009. Mantle Shear-Wave Velocity Structure Beneath the Hawaiian Hot Spot. *Science*, **326**(5958), 1388-1390.

## Appendices

### Appendix A

Sample Descriptions:

#### ***BM 1962 / 60 (Tristan)***

Rock Type: Leucite-bearing Ankaramitic Basalt.

Texture: Inequigranular porphyritic, vesicular.

Composition: 60% phenocrysts (fragmentary), 40% groundmass.

Phenocrysts: Subhedral to anhedral, 1-6 mm (fragmentary).

- Clinopyroxene (50%). Some enclosing olivine, plagioclase and leucite crystals. Melt inclusions are present within some crystals.
- Olivine (30%). Some enclosing leucite crystals. Rare melt inclusions.
- Leucite (20%). Showing multiple twinning.

Groundmass: Plagioclase laths, opaques, fragmentary crystals, glass.

Crystallisation History: Olivine > Leucite > Clinopyroxene.

#### ***BM 1962 / 112 (Tristan)***

Rock Type: Leucite-bearing Olivine Basalt.

Texture: Inequigranular porphyritic. Preferred orientation.

Composition: 33% phenocrysts, 67% groundmass.

Phenocrysts:

- Leucite (50%). 1-2 mm, euhedral to subhedral.
- Clinopyroxene (40%). Euhedral, 1-4 mm in size. Some crystals enclose olivine crystals plagioclase laths.
- Olivine (10%). Subhedral to anhedral, average size of 1.5 mm. Trails of melt inclusions present. Some crystals are resorbed or fractured.

Groundmass: Fine grained, mainly plagioclase laths.

Crystallisation history: Olivine / plagioclase > Clinopyroxene.

***BM 1962 / 114 (Tristan)***

Rock Type: Ankaramitic Basalt.

Texture: Inequigranular porphyritic.

Composition: 15% phenocrysts, 85% fine grained groundmass.

Phenocrysts: Many fractured or resorbed.

- Clinopyroxene (60%). Euhedral, ~3 mm in size. Some showing undulose extinction.
- Opaques (20%).
- Plagioclase (15%). Euhedral laths, ~1.5 mm in length. Some crystals show zoning.
- Olivine (5%). Euhedral, ~1 mm in size. Melt inclusions are present in some crystals.

Groundmass: Shows weak preferred orientation. Mainly comprises of plagioclase laths.

Crystallisation history: Unable to ascertain.

***BM 1962 / 116 (Tristan)***

Rock Type: Leucite-bearing Olivine Basalt.

Texture: Inequigranular porphyritic. Strong preferred orientation.

Composition: 5% phenocrysts, 95% fine grained groundmass.

Phenocrysts: 0.5-2 mm in size.

- Olivine (40%).
- Leucite (40%).
- Plagioclase (15%).
- Clinopyroxene (5%).

Groundmass: Aligned plagioclase laths.

Crystallisation history: Unable to ascertain.

***BM 1962 / 341 (Tristan)***

Rock Type: Trachybasalt.

Texture: Inequigranular porphyritic, preferred orientation.

Composition: 5% phenocrysts; 95% fine grained groundmass.

Phenocrysts:

- Clinopyroxene (75%). Euhedral, 1 mm crystals, showing rare fluid inclusions.
- Leucite (20%). Euhedral, 1 mm crystals, with multiple twinning in various directions.
- Olivine (5%). Subhedral, 1 mm crystals, with rare fluid inclusions.

Groundmass: Mainly plagioclase laths and opaques/glass.

Crystallisation history: Unable to ascertain.

***BM 1962 / 446 (Inaccessible)***

Rock Type: Vesicular Olivine Basalt.

Texture: Inequigranular porphyritic, vesicular. Most vesicles are coalesced and 0.2-3 mm in length.

Composition: 25% phenocrysts, 50% groundmass, 25% vesicles.

Phenocrysts:

- Olivine (45%). Subhedral to anhedral, 3 mm in size. Some crystals show resorption. Melt inclusions are present along fractures and within the crystal.
- Plagioclase (35%). Euhedral to subhedral laths, 1-2 mm in length.
- Clinopyroxene (20%). Euhedral to subhedral, 4-8 mm. Melt inclusions are present. Crystals enclose both olivine and plagioclase.

Groundmass: Glassy (50%), plagioclase laths (50%).

Crystallisation history: Olivine > plagioclase > clinopyroxene.

***BM 1962 / 473 (Inaccessible)***

Rock Type: Vesicular Olivine Basalt.

Texture: Inequigranular porphyritic, vesicular. Vesicles comprise ~20%vol and are 1 mm in diameter; some are coalesced.

Composition: 20% phenocrysts, 60% groundmass, 20% vesicles.

Phenocrysts: Euhedral to subhedral.

- Olivine (40%). Crystals are euhedral to subhedral and range in size from 1-9 mm. Zoning is present in some crystals. Some crystals show resorption and secondary alteration to serpentine. A high density of melt inclusions (~2%) is present, with at least two inclusion assemblages; along fractures and within the crystal. Some crystals are fractured.
- Clinopyroxene (40%). Crystals show both twinning and zoning, are euhedral to subhedral, and 1-5 mm in size. Exsolution lamellae and melt inclusions are observed.
- Plagioclase (20%). Euhedral laths, 2 mm in length.

Groundmass: Glassy.

Crystallisation history: Unable to ascertain.

***BM 1962 / 480 (Inaccessible)***

Rock Type: Picritic Basalt.

Texture: Inequigranular porphyritic, vesicular. Vesicles are rounded, 1 mm in size, with a few coalescing with one another. Flow banding is observed.

Composition: 15% phenocrysts, 70% fine grained groundmass, 15% vesicles.

Phenocrysts:

- Olivine (80%). Euhedral to subhedral, 2-4 mm in size. Some crystals have melt inclusions.
- Clinopyroxene (10%). Euhedral to subhedral, 2-4 mm crystals.
- Plagioclase (10%). Euhedral laths, 2 mm in length, with some alteration present around crystal edges.

Groundmass: Plagioclase laths highlight flow banding.

***BM 1962 / 482 (Tristan)***

Rock Type: Leucite-bearing Olivine Basalt.

Texture: Inequigranular porphyritic.

Composition: 15% phenocrysts, 85% groundmass.

Phenocrysts: Euhedral to subhedral. Many are resorbed or fractured.

- Olivine (70%). 1-3 mm in size.
- Leucite (20%). 3-5 mm in size.
- Clinopyroxene (10%). ~2 mm in size.

Groundmass: Plagioclase laths.

Crystallisation history: Unable to ascertain.

***BM 1962 / 484 (Tristan)***

Rock Type: Leucite-bearing Vesicular Trachybasalt.

Texture: Inequigranular porphyritic. Preferred orientation and vesicular; vesicles are mainly coalesced and ~2 mm in length.

Composition: 35% phenocrysts, 45% groundmass, 20% vesicles.

Phenocrysts:

- Clinopyroxene (60%). Crystals are euhedral and 1-3 mm in length. Some crystals are twinned; rare melt inclusions are observed. Some crystals enclose crystals of olivine and leucite.
- Olivine (30%). Subhedral, 1-2 mm in size. Some crystals are resorbed. Rare melt inclusions are observed.
- Leucite (10%). Subhedral, 1 mm in size.

Groundmass: Plagioclase laths and glass.

Crystallisation history: Olivine / leucite > clinopyroxene.

## Appendix B

Table of thin sections found on accompanying CD:

<b>Filename</b>	<b>Sample Number</b>	<b>Brief Description</b>
BM 1962 128 60_ovl_001_ppl.jpg	60	Texture
BM 1962 128 60_ovl_001_xpl.jpg	60	Texture
BM 1962 128 60_ovl_002_ppl.jpg	60	Groundmass
BM 1962 128 60_ovl_002_xpl.jpg	60	Groundmass
BM 1962 128 60_ovl_003_ppl.jpg	60	Inclusions
BM 1962 128 60_ovl_003_xpl.jpg	60	Inclusions
BM 1962 128 60_ovl_004_ppl.jpg	60	Ol in cpx phenocryst
BM 1962 128 60_ovl_004_xpl.jpg	60	Ol in cpx phenocryst
BM 1962 128 60_ovl_005_ppl.jpg	60	Leuc in cpx phenocryst
BM 1962 128 60_ovl_005_xpl.jpg	60	Leuc in cpx phenocryst
BM 1962 128 112_ovl_001_ppl.jpg	112	Texture
BM 1962 128 112_ovl_001_xpl.jpg	112	Texture
BM 1962 128 112_ovl_002_ppl.jpg	112	Ol with inclusions
BM 1962 128 112_ovl_002_xpl.jpg	112	Ol with inclusions
BM 1962 128 112_ovl_003_ppl.jpg	112	Inclusions
BM 1962 128 112_ovl_003_xpl.jpg	112	Inclusions
BM 1962 128 112_ovl_004_ppl.jpg	112	Inclusions
BM 1962 128 112_ovl_004_xpl.jpg	112	Inclusions
BM 1962 128 112_ovl_005_ppl.jpg	112	Inclusions
BM 1962 128 112_ovl_005_xpl.jpg	112	Inclusions
BM 1962 128 112_ovl_006_ppl.jpg	112	Leuc in cpx
BM 1962 128 112_ovl_006_xpl.jpg	112	Leuc in cpx

BM 1962 128 112_ovl_007_ppl.jpg	112	Plag alignment around cpx
BM 1962 128 112_ovl_007_xpl.jpg	112	Plag alignment around cpx
BM 1962 128 114_ovl_001_ppl.jpg	114	Cpx phenocryst
BM 1962 128 114_ovl_001_xpl.jpg	114	Cpx phenocryst
BM 1962 128 114_ovl_002_ppl.jpg	114	Texture
BM 1962 128 114_ovl_002_xpl.jpg	114	Texture
BM 1962 128 114_ovl_003_ppl.jpg	114	Inclusions
BM 1962 128 114_ovl_003_xpl.jpg	114	Inclusions
BM 1962 128 114_ovl_004_ppl.jpg	114	Texture
BM 1962 128 114_ovl_004_xpl.jpg	114	Texture
BM 1962 128 114_ovl_005_ppl.jpg	114	Inclusions, flow banding
BM 1962 128 114_ovl_005_xpl.jpg	114	Inclusions, flow banding
BM 1962 128 114_ovl_006_ppl.jpg	114	Texture
BM 1962 128 114_ovl_006_xpl.jpg	114	Texture
BM 1962 128 114_ovl_007_ppl.jpg	114	Plag zoning
BM 1962 128 114_ovl_007_xpl.jpg	114	Plag zoning
BM 1962 128 116_ovl_001_ppl.jpg	116	Texture
BM 1962 128 116_ovl_001_xpl.jpg	116	Texture
BM 1962 128 116_ovl_002_ppl.jpg	116	Mineral alignment
BM 1962 128 116_ovl_002_xpl.jpg	116	Mineral alignment
BM 1962 128 116_ovl_003_ppl.jpg	116	Alignment around cpx
BM 1962 128 116_ovl_003_xpl.jpg	116	Alignment around cpx
BM 1962 128 341_ovl_001_ppl.jpg	341	Lava clot
BM 1962 128 341_ovl_001_xpl.jpg	341	Lava clot
BM 1962 128 341_ovl_002_ppl.jpg	341	Inclusions
BM 1962 128 341_ovl_002_xpl.jpg	341	Inclusions

BM 1962 128 341_ovl_003_ppl.jpg	341	Texture
BM 1962 128 341_ovl_003_xpl.jpg	341	Texture
BM 1962 128 341_ovl_004_ppl.jpg	341	Resorbed cpx
BM 1962 128 341_ovl_004_xpl.jpg	341	Resorbed cpx
BM 1962 128 341_ovl_005_ppl.jpg	341	Leuc
BM 1962 128 341_ovl_005_xpl.jpg	341	Leuc
BM 1962 128 341_ovl_006_ppl.jpg	341	Leuc
BM 1962 128 341_ovl_006_xpl.jpg	341	Leuc
BM 1962 128 446_ovl_001_ppl.jpg	446	Texture
BM 1962 128 446_ovl_001_xpl.jpg	446	Texture
BM 1962 128 446_ovl_002_ppl.jpg	446	Cpx with mineral inclusions
BM 1962 128 446_ovl_002_xpl.jpg	446	Cpx with mineral inclusions
BM 1962 128 446_ovl_003_xpl.jpg	446	Ol resorbtion
BM 1962 128 473_ovl_001_ppl.jpg	473	Ol zoning, alteration
BM 1962 128 473_ovl_001_xpl.jpg	473	Ol zoning, alteration
BM 1962 128 473_ovl_002_ppl.jpg	473	Texture
BM 1962 128 473_ovl_002_xpl.jpg	473	Texture
BM 1962 128 473_ovl_003_ppl.jpg	473	Ol – fractured crystal
BM 1962 128 473_ovl_003_xpl.jpg	473	Ol – fractured crystal
BM 1962 128 473_ovl_004_ppl.jpg	473	Ol with inclusions
BM 1962 128 473_ovl_004_xpl.jpg	473	Ol with inclusions
BM 1962 128 473_ovl_005_ppl.jpg	473	Cpx with exsolution
BM 1962 128 473_ovl_005_xpl.jpg	473	Cpx with exsolution
BM 1962 128 480_ovl_001_ppl.jpg	480	Ol, flow banding
BM 1962 128 480_ovl_001_xpl.jpg	480	Ol, flow banding
BM 1962 128 480_ovl_002_ppl.jpg	480	Texture

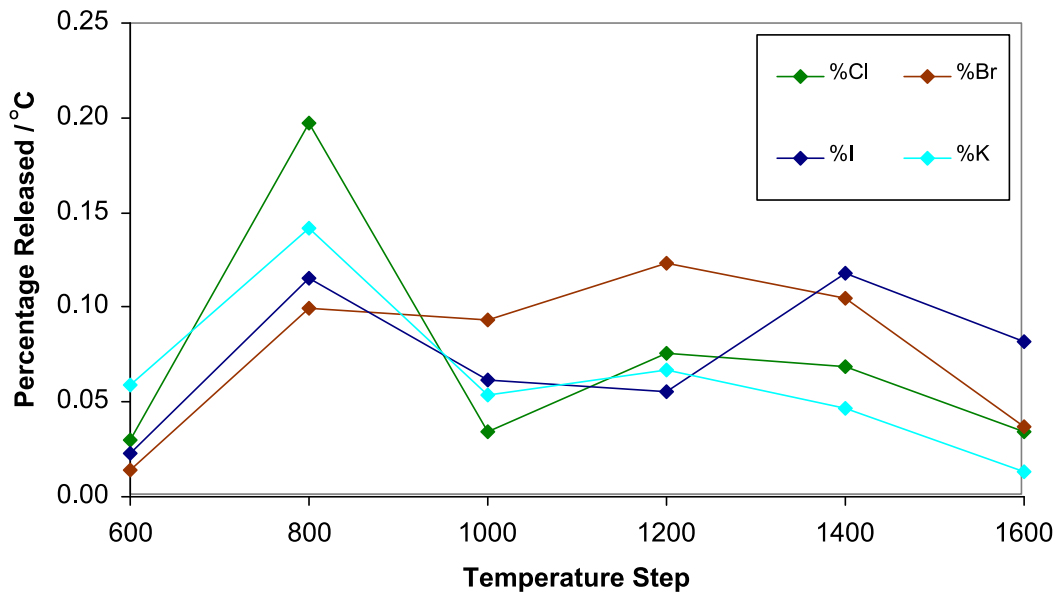
BM 1962 128 480_ovl_002_xpl.jpg	480	Texture
BM 1962 128 482_ovl_001_ppl.jpg	482	Ol with inclusions
BM 1962 128 482_ovl_001_xpl.jpg	482	Ol with inclusions
BM 1962 128 482_ovl_002_ppl.jpg	482	Ol with inclusions
BM 1962 128 482_ovl_002_xpl.jpg	482	Ol with inclusions
BM 1962 128 482_ovl_003_ppl.jpg	482	Ol with inclusions
BM 1962 128 482_ovl_003_xpl.jpg	482	Ol with inclusions
BM 1962 128 482_ovl_004_ppl.jpg	482	Zoned ol crystal
BM 1962 128 482_ovl_004_xpl.jpg	482	Zoned ol crystal
BM 1962 128 482_ovl_005_ppl.jpg	482	Resorbed ol
BM 1962 128 482_ovl_005_xpl.jpg	482	Resorbed ol
BM 1962 128 482_ovl_006_ppl.jpg	482	Resorbed cpx
BM 1962 128 482_ovl_006_xpl.jpg	482	Resorbed cpx
BM 1962 128 482_ovl_007_ppl.jpg	482	Zoned ol phenocryst
BM 1962 128 482_ovl_007_xpl.jpg	482	Zoned ol phenocryst
BM 1962 128 482_ovl_008_ppl.jpg	482	Resorbed leuc
BM 1962 128 482_ovl_008_xpl.jpg	482	Resorbed leuc
BM 1962 128 484_ovl_001_ppl.jpg	484	Vesicles
BM 1962 128 484_ovl_001_xpl.jpg	484	Vesicles
BM 1962 128 484_ovl_002_ppl.jpg	484	Inclusions
BM 1962 128 484_ovl_002_xpl.jpg	484	Inclusions
BM 1962 128 484_ovl_003_ppl.jpg	484	Inclusions
BM 1962 128 484_ovl_003_xpl.jpg	484	Inclusions
BM 1962 128 484_ovl_004_ppl.jpg	484	Ol with inclusions
BM 1962 128 484_ovl_004_xpl.jpg	484	Ol with inclusions
BM 1962 128 484_ovl_005_ppl.jpg	484	Resorbed cpx

BM 1962 128 484_ovl_005_xpl.jpg	484	Resorbed cpx
BM 1962 128 484_ovl_006_ppl.jpg	484	Resorbed leuc
BM 1962 128 484_ovl_006_xpl.jpg	484	Resorbed leuc
BM 1962 128 484_ovl_007_ppl.jpg	484	Resorbed ol
BM 1962 128 484_ovl_007_xpl.jpg	484	Resorbed ol
BM 1962 128 484_ovl_008_ppl.jpg	484	Texture
BM 1962 128 484_ovl_008_xpl.jpg	484	Texture

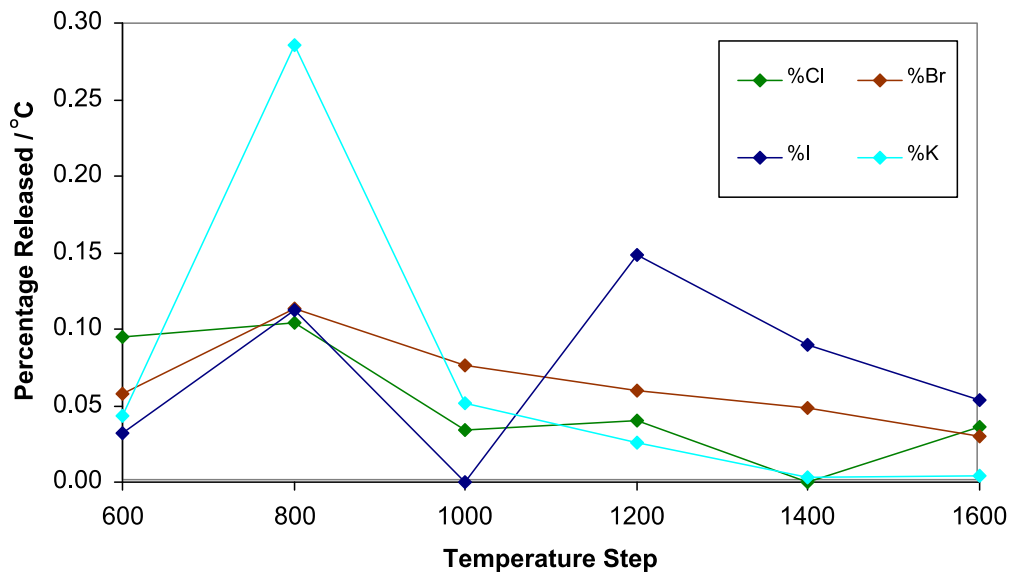
## Appendix C

Halogen and K release plots:

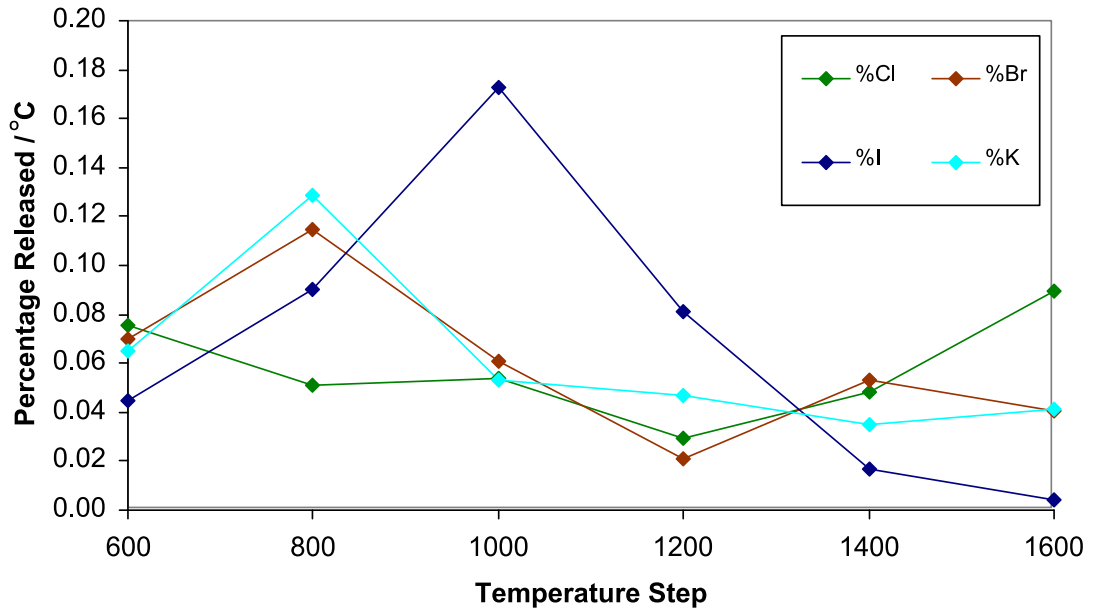
BM 1962 128 / 112 (Tristan)



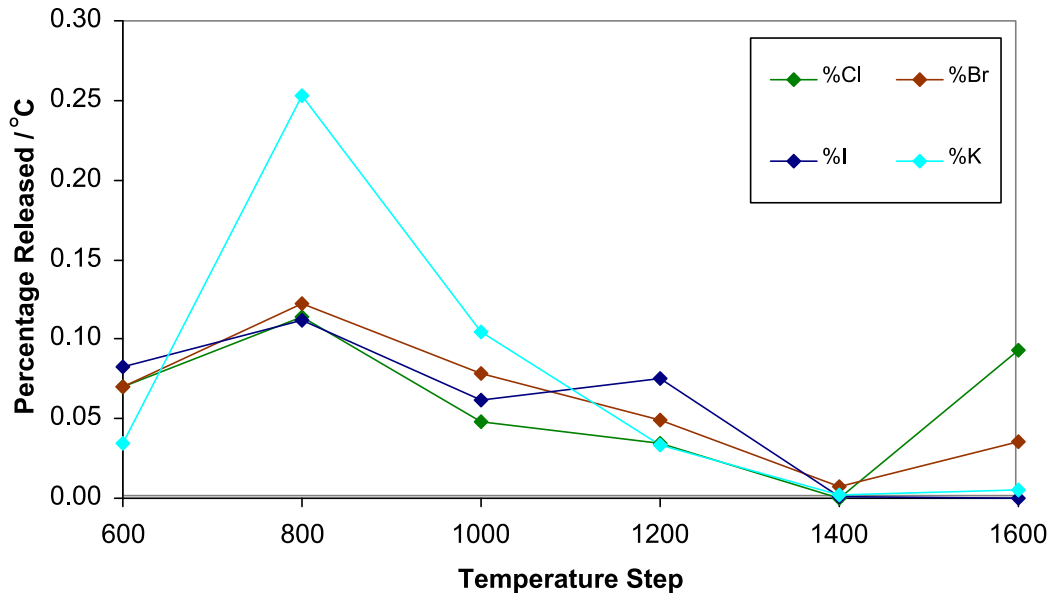
BM 1962 128 / 114 (Tristan)



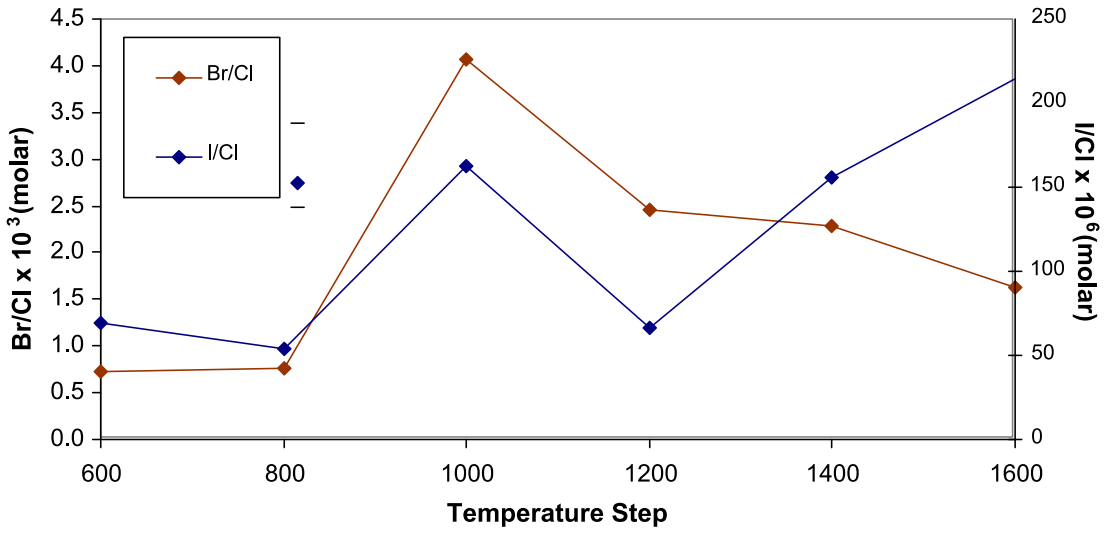
BM 1962 128 / 446 (Inaccessible)



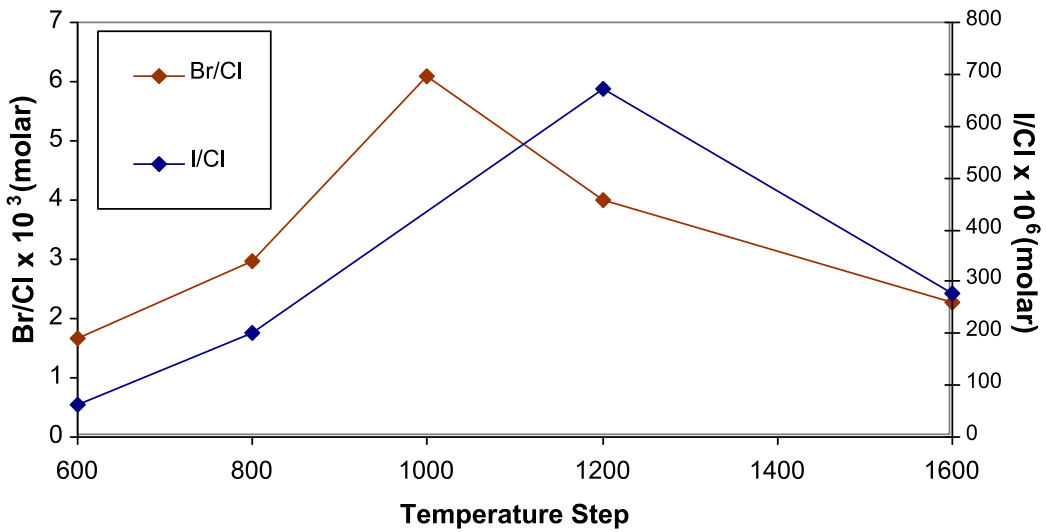
BM 1962 128 / 480 (Inaccessible)



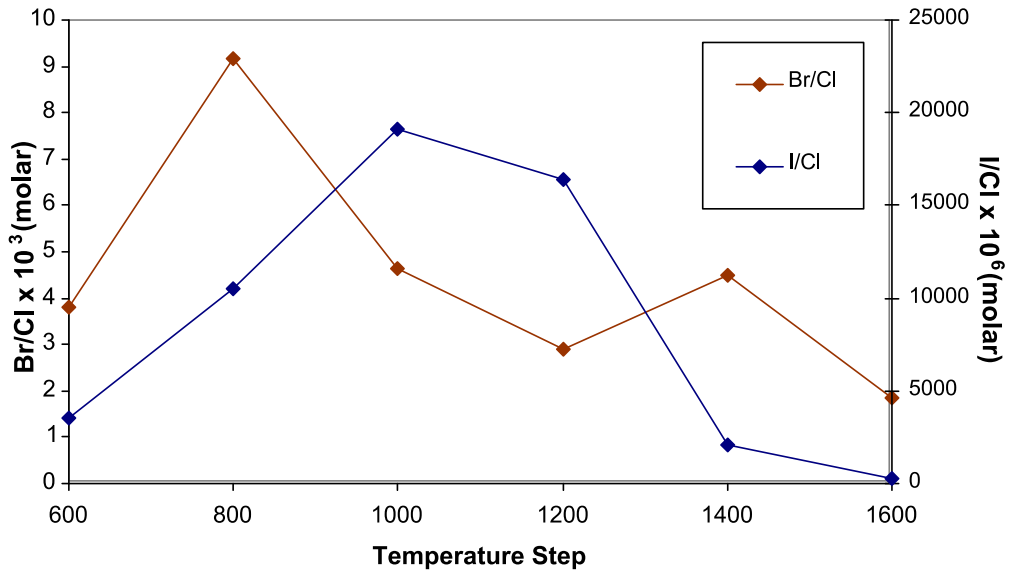
BM 1962 128 / 112 (Tristan)



BM 1962 128 / 114 (Tristan)



BM 1962 128 / 446 (Inaccessible)



BM 1962 128 / 480 (Inaccessible)

